Quotes

Man hat den Eindruck, dass die moderne Physik auf Annahmen beruht, die irgendwie dem Lächeln einer Katze gleichen, die gar nicht da ist.
- Albert Einstein (Nobel Prize 1921)

I do not like it, and I am sorry I ever had anything to do with it.
- Erwin Schrödinger (Nobel Prize 1933)
speaking of quantum mechanics

Zwei Dinge scheinen unendlich, das Universum und die menschliche Dummheit. Beim Universum bin ich mir nicht ganz sicher.
- Albert Einstein (Nobel Prize 1921)

Physics is very muddled again at the moment; it is much too hard for me anyway, and I wish I were a movie comedian or something like that and had never heard anything about physics.
- Wolfgang Pauli (Nobel Prize 1935)
in a letter to R. Kronig 1925

Seit die Mathematiker über die Relativitätstheorie hergefallen sind, verstehe ich sie selbst nicht mehr.
- Albert Einstein (Nobel Prize 1921)

University of Alberta

Towards an erbium-doped waveguide amplifier sensitized by silicon nanoclusters

by

Florian C. Lenz

A thesis submitted to the Faculty of Graduate Studies and Research
in partial fulfillment of the requirements for the degree of

Master of Science
in
Communications and Signal Processing

Department of Electrical and Computer Engineering

©Florian C. Lenz
Fall 2009
Edmonton, Alberta

University of Alberta

Faculty of Graduate Studies and Research

Examining Committee:

Dr. Raymond DeCorby
Department of Electrical and Computer Engineering

Dr. Al Meldrum
Department of Physics

Dr. James McMullin
Department of Electrical and Computer Engineering

Dr. Jonathan Veinot
Department of Chemistry

This thesis is dedicated to my wife Esther to thank her for her love and support during the time I have spent in Canada with her and working towards this degree. If it wasn't for her, I would most likely not even be here and do what I am doing.

Abstract

Amorphous and crystalline silicon nanocomposites have been shown to act as effective "sensitizers" for erbium ions. In the present work, a series of erbium-doped (0.2 at.%) SiO_x:Er films ($x = 1 - 1.8$) were synthesized by physical vapor deposition and subsequently annealed at temperatures ranging from $400°C$ to $1100°C$ to induce phase separation and cluster growth. Silicon nanocluster (Si-NC) and Er^{3+} photoluminescence intensity spectra and dynamics were investigated as a function of SiO_x composition, annealing temperature, pump wavelength and power, and specimen temperature in order to determine characteristic cross-sections and to map the efficiency of the energy transfer process between Si-NCs and Er^{3+} ions. Additionally, two types of optical waveguides based on SiO_x:Er materials were fabricated using conventional CMOS compatible microfabrication processes. Waveguide propagation losses as well as signal absorption and enhancement were investigated under pumping conditions to evaluate the use of SiO_x:Er materials as amplifying media.

In gratitude

I have been lucky to work and live with a bunch of fantastic people throughout the last years. Some helped me out with my studies, some in the lab, others with moral support, and it is here where I get to say: THANK YOU !

Most importantly thanks to my wonderful wife Esther for always being there for me and enduring the periods of procrastination during my time as a MSc. student. I would like to continue by thanking both my supervisors, Dr. Ray DeCorby, and Dr. Al Meldrum. As partners in crime, they have done (and still do) a tremendous job in guiding students, teaching classes, and letting us play with all that fancy equipment in the labs. Thanks Al, for letting me mark the classes you were teaching, the extra money made paying that international differential fee much easier. And what would student life be without some geeky lab-mates to work, discuss, and share geek jokes with? A big thanks to you guys, you made the time here fun. In my "engineering group", many thanks to Nakeeran for putting up with all the stuff I make him join me, to Trevor for his comic book rentals, to Tom for his valuable tips, and to Eric for time on tennis and squash courts. In my "physics group", many thanks to Nicole and Aaron, my first office neighbors and instructors (Canadian Campus 101). Further thanks to Sulan for constantly reminding me to keep going, to Kai for suffering with me through the condensed matter class, and to Pablo for computer related support. Thanks also to the three undergrad musketeers: 'sexy geek' Ross, Mary, and Mac.

Further acknowledgement goes to the two thin film gurus and technicians, Don Mullin and Greg Popowich. I don't know if anything would be running down there in the lab without them. Very special thanks to Hue Nguyen for all the patience and efforts she had to invest in teaching me in the NanoFab. Thanks to Dave Clegg for his support with the fiber optic equipment at TRLabs and to George Braybrook for his excellent work on the SEM.

Contents

List of Tables

List of Figures

List of Abbreviations and Acronyms

A	Acceptor
a-	Amorphous
AOM	Acousto-optic modulator
BCB	Benzocyclobutene
BOE	Buffered-oxide-etch
BPF	Band-pass filter
c-	Crystalline
CCA	Confined carrier absorption
CCD	Charge-coupled device
CM	Crystal monitor
CMOS	Complementary metal-oxide-semiconductor
D	Donor
dB	Decibel
DF	Dark field
DOS	Density of states
EDFA	Erbium-doped fiber amplifier
EDWA	Erbium-doped waveguide amplifier
EDX	Energy-dispersive X-ray
EF	Energy-filtered
EFTEM	Energy-filtered transmission electron microscopy
EMPA	Electron microprobe analysis
ESA	Excited state absorption
FCA	Free carrier absorption
GLAD	Glancing angle deposition
HAADF	High angle annular dark field
HMDS	Hexamethyldisilizane
HREM	High-resolution electron microscopy
HRTEM	High-resolution transmission electron microscopy

IC	Integrated circuit
ICRIE	Inductively-coupled plasma reactive-ion-etch
ITRS	International Technology Roadmap for Semiconductors
LED	Light-emitting diode
LPF	Long-pass filter
NC	Nanocluster
NIR	Near-infrared
OSA	Optical spectrum analyzer
PC	Personal computer
PECVD	Plasma-enhanced chemical vapor deposition
PL	Photoluminescence
PMT	Photomultiplier tube
PVD	Physical vapor deposition
QC	Quantum confinement
RBS	Rutherford backscattering spectroscopy
RE	Rare earth
RIE	Reactive-ion-etch
RMS	Root-mean-square value
S	Substrate
SEM	Scanning electron microscopy
SH	Shield
SRO	Silicon-rich oxide
STEM	Scanning transmission electron microscopy
TE	Transverse-electric
TEM	Transmission electron microscopy
TEOS	Tetrahylorthosilicate
TM	Transverse-magnetic
UV	Ultraviolet
WDM	Wavelength-division multiplexer
WKB	Wentzel-Kramers-Brouillin approximation
YAG	Ytterbium aluminium garnet
2D	Two-dimensional
3D	Three-dimensional

List of Symbols

a_B	Exciton Bohr radius
at.%	atomic percentage
d_b	Barrier thickness
d_p	Particle diameter
E	Energy
E_g	Bandgap energy
E_c, E_v	Energy of conduction and valence band mobility edges
Er_atomic	atomic percentage of erbium atoms
$g_A(\nu)$	Acceptor absorption spectrum
$g_D(\nu)$	Donor emission spectrum
g_Er	Erbium related gain
h	Planck constant: 4.136×10^{-15} eVs
$\hbar$	Reduced Planck constant: 6.582×10^{-16} eVs
$h\nu$	Photon energy
I	Intensity
J	Total angular momentum
$\mathbf{k}$	Electron wavevector
k_B	Boltzmann's constant: 8.617×10^{-5} eV/K
L	Orbital angular momentum
l_ab, l_wg	Length of waveguide piece (from a to b)
l_k	orbital operator
L_wg	Waveguide loss in dB/cm

$\bar{M}_{\mathrm{SiO_x}}$	Average molar mass of atoms in $\mathrm{SiO_x}$
m_{b}	Carrier effective mass in the barrier
m_{p}	Carrier effective mass in the particle
n	Refractive index
N_A	Avogadro's number: 6.02×10^{23} mol^{-1}
N_{Er}	Number of erbium ions
N_{exc}	Number of excitable erbium ions
$N(E)$	Density of (energy) states
P	Power (optical)
r	Nanocrystal radius
R	Donor-acceptor separation distance
R^2	Coefficient of determination
R_{abs}	Absorption rate
R_{exc}	Excitation rate
R_0	Distance at which $w_{\mathrm{tr}} = w_{\mathrm{pl}}$
R_c	Electron-hole pair capture radius
R_{exc}	Excitation rate
S	Spin angular momentum
s_k	spin operator
t	Time
T	Temperature (of the sample)
T_{anneal}	Annealing temperature
V	Barrier height
w	Transition rate
w_{pl}	Photoluminescence rate
w_{tr}	Transfer rate
w_{tunnel}	Single-carrier tunneling rate
x	Oxygen-to-silicon atomic ratio
$\alpha\,(\lambda)$	Wavelength dependent absorption
α_0	Erbium absorption at $\lambda = 1.534$ µm and zero pump power
β	Stretch factor (constant exponent of a stretched exponential)
Γ	Core confinement factor
$\Delta E, \epsilon$	Energy difference
ϕ_{pump}	Incident pump photon flux
λ	Wavelength of light
$\rho_{\mathrm{SiO_x}}$	$\mathrm{SiO_x}$ film density
σ_{abs}	Absorption cross section
σ_{eff}	Effective excitation cross section
τ_{decay}	1/e decay time constant (or lifetime)
τ_{rise}	1/e rise time constant (or lifetime)

Introduction: Light emission from silicon

1.1 The need for a silicon-based light source

In 1965, Intel co-founder Gordon Moore published his famous article about "cramming more components onto integrated circuits"[1], creating what is known today as *Moore's Law*. By analyzing statistical data about the evolution of the microelectronics industry, Moore discovered that the number of transistors that could fit onto a square inch of silicon doubled every year. Although Moore had to revise the doubling period ten years later (to two years), his "law" still holds true up to this day. This rapid evolution in the complexity of integrated circuits (ICs) is enabled by scaling. Starting from dimensions of tens of micrometers, the minimum size that can be patterned on a silicon chip has been reduced to less than 100 nm in recent years, in turn enabling the arrangement of an increasing number of electronic components on the same area. Scaling benchmarks are set and monitored through the *International Technology Roadmap for Semiconductors* (ITRS), published every other year by a consortium representing the semiconductor industry.[2] It specifies requirements, possible solutions, and time frames for the semiconductor industry over the next fifteen years to come. In recent years, the ITRS has pointed out a problem associated with continued scaling that would eventually slow down Moore's Law; the so-called "interconnection bottleneck". As the number and density of electronic components in a single integrated circuit increases, more closely spaced interconnecting wires are necessary to link all those components together. Scaling also reduces the cross sectional area of each wire, proportionally increasing its electrical resistance. This leads to limiting factors such as capacitive charging delays and power dissipation. In the roadmap, these issues compose the so-called "red brick wall".

Among different approaches that are being investigated to overcome the above obstacles, optical solutions are considered a primary option for replacing electronic

interconnects[3,4]. The information would be carried not by electrons, but by an optical signal (i.e. photons). An analogous transformation from electronics to photonics is successfully taking place with the development of optical fiber networks. Integration of optical functionality on an electronic circuit - so-called *microphotonics* - could become an important technology in the near future. The potential advantages of using photonic interconnects (i.e. waveguides) are manyfold. Photons, unlike electrons, are immune to cross-talk and electromagnetic interference, can have very low transmission losses, and perhaps most significantly, have practically unlimited information carrying capacity. One additional advantage of optical interconnects is the possibility of wavelength multiplexing of signals simultaneously on the same waveguide, as is common practice in fiber optics. The goal in microphotonics is to create high performance optical devices, including light emitters (lasers), waveguides, modulators, and detectors, from a set of complementary metal-oxide-semiconductor (CMOS) compatible materials.

Naturally, silicon is a desirable material for the implementation and integration of microphotonics. Silicon is the predominant semiconductor material in electronics and microchip technology and has been called the "engine" of the information revolution[5].

The importance of silicon is due to its outstanding electronic properties, natural abundance, good thermal conductivity, and good mechanical strength. Furthermore, its oxide (SiO_2) is a very good insulator, that can passivate surfaces and act as an effective diffusion barrier. All of these properties made silicon the leading material in microelectronic applications. But silicon can do well in photonics as well; it has a high refractive index of about 3.5 and a small intrinsic absorption at infrared wavelengths. The fabrication processes and techniques available for silicon are a mature technology that allow production of structures in micrometer and nanometer size, and can readily be utilized to build photonic devices on silicon circuits. As a result, the optical properties of silicon and the development of Si-based photonic devices have been important topics in research for decades, and today most building blocks for integrated photonics, such as low-loss waveguides, modulators, and switches, have been designed and monolithically integrated on silicon. Up to now, one significant limitation in achieving fully integrated photonics and electronics on a silicon chip has been the lack of an efficient Si-based light emitter or a Si-laser, which are needed to generate light and to balance the losses caused by passive devices such as splitters and switches.

1.2   Silicon light emission

1.2.1   Bulk crystalline silicon

Despite its many advantages as a semiconductor material, crystalline silicon is an inefficient light emitter with a quantum efficiency for photon emission of $\sim 10^{-7}$

to 10^{-6} at room-temperature in standard electronic grade silicon[6–8], four orders of magnitude smaller than for direct bandgap semiconductors. The quantum efficiency is defined as the number of generated photons as a fraction of the number of excited electron-hole pairs. This fact constitutes a major drawback in the attempt to replace the electronic devices on a silicon-based microchip with photonic components. The existence of a bandgap, i.e. forbidden energy regions, in a crystal is
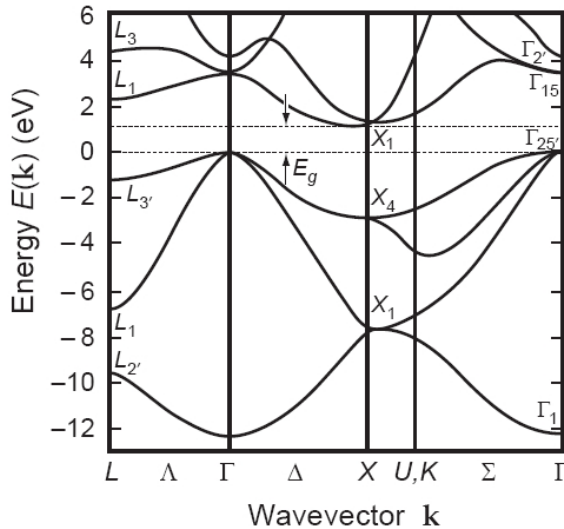
Fig. 1.1: Theoretical band structure of crystalline silicon after Ref.[9]. The indirect-bandgap character of silicon is evident by the mismatch in wave vectors for the positions at which valence band maximum and conduction band minimum occur.

closely related to the periodicity of the crystal lattice. This periodicity is accounted for in the Hamiltonian by the crystal potential. Bloch's theorem states that the solutions to the Schrödinger equation for electrons influenced by a crystal potential can be described as the product of a plane wave and a function with the same periodicity as the crystal lattice. Allowed values of the electron wavevectors $\mathbf{k}$ depend upon the long-range order and symmetry of the crystal lattice[10], and often band structure diagrams of E as a function of $\mathbf{k}$ are used to illustrate the allowed electron energies in a crystal. The energy band structure in semiconductor materials is derived from the relationship between the momentum and energy of a charge carrier, not only depending on the crystal structure but also on the bonding between atoms, the respective bond length, and the chemical species[11]. These band structures are often quite complex and their calculation elaborate; a result of such a calculation is shown in Fig. 1.1 for crystalline silicon. It is easy to see that bulk crystalline silicon is an indirect bandgap semiconductor, since the conduction band minimum (near the X point at the Brillouin zone boundary) occurs at a different wavevector $\mathbf{k}$ compared to the valence band maxima (Γ point at the Brillouin zone center). The vertical separation between the valence band maximum and the conduction band minimum (i.e. the difference in energy of the electron states) is termed the "electronic" bandgap, E_g. Since optical transitions conserve both energy and crystal momentum, only phonon assisted absorption and emission processes can occur

in silicon and other indirect bandgap semiconductors. This makes the probability for spontaneous recombination very low and thereby the radiative decay lifetime is long ($\gtrsim$ 1 ms) compared to competing non-radiative transitions with much faster rates (ns to μs). This ultimately results in a low quantum efficiency, severely restricting the possibilities for the development of effective light emitters based on recombination across the fundamental bandgap.

Different strategies, summarized by Lockwood and Pavesi[11] as *materials engineering*, have been researched in recent years to overcome the limitations of the indirect bandgap in silicon:

- **Band structure engineering** aims to modify the band structure of bulk silicon and fabricate a direct bandgap material. One strategy described in Refs.[12,13] utilizes the deposition of superlattices, with layer thicknesses on the order of the unit cell dimensions, by molecular beam epitaxy. The periodicity of these superlattices results in the "folding back" of the electronic band structure into a reduced Brillouin zone, thereby creating a direct bandgap. Another way to change the band structure is by alloying of germanium or carbon with silicon.

- **Quantum confinement effects** in nanostructured Si have received a large amount of attention lately, including porous silicon, nanoclusters, quantum wells, quantum wires, and quantum dots. In these small structures - with diameters less than the size of the free exciton Bohr radius in bulk Si (4.3 nm) - the electron-hole wavefunction overlap is increased by quantum confinement, resulting in enhanced radiative rates. The requirement for momentum conservation is relaxed in small structures due to the uncertainty principle, increasing the probability for direct transitions.

- **Impurity doping** is another possibility to achieve efficient light emission from silicon. By introducing localization centers for electron-hole recombination, such as rare-earth ions[14], carbon complexes[15], or sulfur/oxygen complexes[16], efficient light emission can be achieved. Combining the effects of quantum confinement in nanostructured silicon with the insertion of efficient light emitting impurities (i.e. rare-earth metal ions) has shown great potential and will be one of the main topics of this thesis.

1.2.2 Bulk amorphous silicon

Since amorphous Si (a-Si) does not possess a periodic lattice and long-range order as does crystalline silicon, its electrons cannot be described by Bloch waves. Therefore, reasoning of the existence of a band gap in a-Si via the Bloch construction in conventional crystal theory fails and no $E(\mathbf{k})$ band structure representation exists.[9] A "proof-of-existence" theorem for the bandgap in amorphous solids was presented by Weaire and Thorpe[17,18], only short-range order due to bonding being
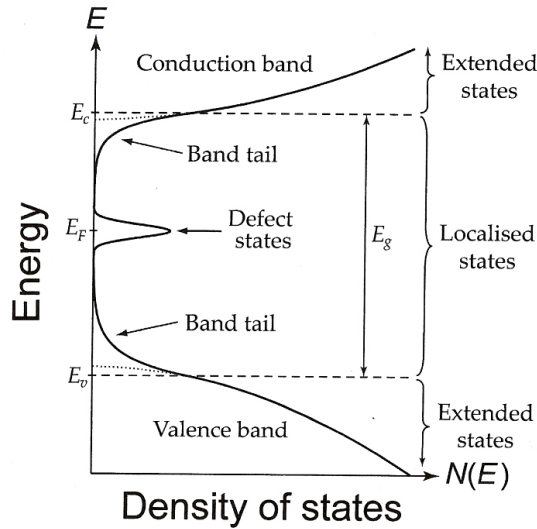
Fig. 1.2: Schematic density of states for a typical amorphous semiconductor. E_c and E_v are the mobility edges for the conduction and valence bands, whereby $E_g = E_c - E_v$ defines the mobility gap. Coordination defects manifest themselves as deep-gap defect states. Dotted lines represent abrupt band edges of a crystalline semiconductor. (After Ref.[9])

considered in their model. It was shown that, although the representation in an $E(\mathbf{k})$ diagram is not applicable, a bandgap can exist in a-Si; e.g. there is no overlap between the energy band created by bonding orbitals (valence band) and the band created by antibonding orbitals (conduction band).[9]

A concept shared by both crystalline and amorphous solids is that of the density of states (DOS) $N(E)$, shown schematically for a typical amorphous semiconductor in Fig. 1.2. The effect of the topological disorder in an amorphous lattice is the broadening of the sharp parabolic band edges of the crystal case into an exponential distribution of states trailing off into the mobility gap, the so-called *band tails*. The mobility gap is defined by the mobility edges E_v and E_c, the energies marking the boundary between the localized states in the band tails and the extended states in the valence and conduction bands, respectively (see Ref.[9] for a more detailed treatment). Irregularities in the ideal *continuous random network* of the amorphous semiconductor introduce a narrow band of localized defects states within the gap, thereby pinning the Fermi level near mid-gap.

It is evident from Fig. 1.1 that the minimum energy for vertical transitions in crystalline-Si is on the order of 3 eV. The restrictions on $\mathbf{k}$ due to the indirect nature of the bandgap prevent efficient emission of photons with energies below 3 eV, although the electronic bandgap is only $\sim$1.12 eV. In amorphous-Si, however, the strong scattering caused by the structural disorder creates a large uncertainty in the wavevector $\mathbf{k}$. As such, an overlap of states in real space is sufficient to promote efficient transitions[20]. The relaxation of momentum-conservation rules in amorphous-Si also makes the distinction between direct and indirect bandgap irrelevant. Interband electronic transitions are allowed in a-Si for all energies above the mobility gap of about 1 eV, greatly increasing the probabilities for optical transitions in the 1 to 3 eV range, leading to a much higher absorption coefficient ($> 10^5$
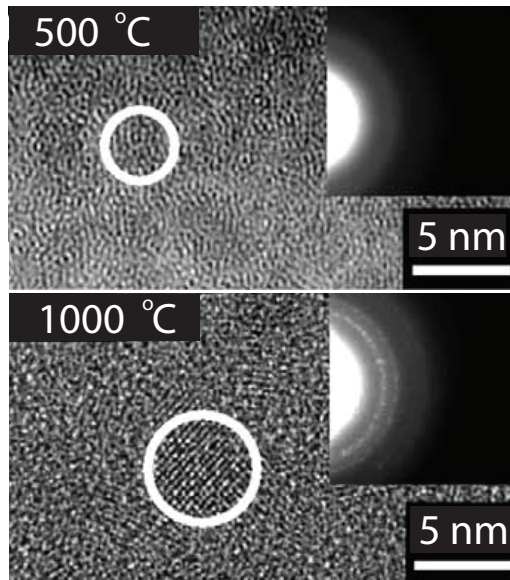
Fig. 1.3: High-resolution electron microscope images and diffraction data for SiO films annealed at 500 and 1000 ˚C showing amorphous Si nanocluster (500 ˚C) and Si nanocrystal (1000 ˚C). After Ref.[19].

cm^{-1}) in the visible wavelength region as compared to c-Si ($\sim 10^3$ cm^{-1} at $\lambda = 700$ nm).

1.2.3 Silicon nanocomposites

Since traditional group III-V alloy photonic materials are relatively incompatible with CMOS microelectronic fabrication processes - primarily due to mismatched crystal lattice constants with respect to Si - nanostructured silicon has been actively explored as an alternative light emitter for silicon photonics. In 2000, articles by Canham[21] and Pavesi *et al.*[22] published in *Nature* highlighted how promising the quantum confinement approach could be and sparked renewed and increased interest in silicon based nanostructures and their properties. But the story of bright light emission from silicon nanocomposites already began in 1984 with the first report of drastically altered photoluminescence (PL) efficiency in so-called 'porous silicon', produced by partial electrochemical dissolution of silicon wafers in hydrofluoric acid based electrolytes[9]. Such porous Si films feature dot- or column-like silicon grains (embedded in SiO$_2$), and can yield intense PL in the visible wavelength range.[23] Similar observations have since been made in nanostructured silicon materials (see Fig. 1.3) fabricated via thermal precipitation of silicon nanoclusters from films of SiO$_x$ deposited by ion implantation[24,25], sputtering[26–28], plasma-enhanced chemical vapor deposition (PECVD)[29,30], and thermal co-evaporation of silicon rich oxides (SRO)[31,32], and others. Most of these deposition techniques allow for the incorporation of rare-earth ions as well.

The observed optical behavior was first recognized as a quantum confinement effect by Canham in 1990.[33] Both crystalline and amorphous Si nanoparticles generally show broad photoluminescence bands in the visible to near-infrared spectral region, blueshifted with respect to the electronic bandgap of silicon. These broad luminescence spectra seem to be caused by contributions from nanoparticles with different sizes, although the fundamental radiative recombination processes in a-Si nanoparticles are thought to be different from those of silicon nanocrystals.[34]

1.2.3.1 Silicon nanocrystals

Efficient luminescence observed in silicon nanocrystals materials is generally attributed to the transitions between confined electron and hole states inside the nanocrystal, the so-called *quantum confinement effect*.[35] Once a semiconductor structure is reduced to nanometric sizes (i.e. a quantum dot) comparable to the exciton Bohr radius*, its electronic states become localized within the nanocrystal and the momentum distribution spreads due to the Heisenberg uncertainty relations.[37] Moreover, due to the boundary conditions, only certain wavefunctions can exist; the energy of the confined particles becomes quantized.[6] In the simplest model of infinitely high potential barriers at the quantum dot boundary it is possible to estimate the energies of electrons and holes localized inside the nanocrystal (via an effective mass approximation) as proportional to $1/r^2$, where r is the nanocrystal radius. The optical gap is given by[37]

$$E_g\left(\mathrm{r}\right) = E_g + \frac{A}{\mathrm{r}^2},\tag{1.1}$$

where E_g is the bandgap of bulk silicon, A is some positive constant, and A/r^2 represents the total energy of the non-interacting electron-hole pairs inside the dot. It is evident that: (i) the nanocrystal bandgap energy is increased compared to the bulk value of $E_g = 1.12$ eV due to the additional positive term A/r^2, and (ii) the photon energy increases as the nanocrystal size decreases. Most experimental data suggests a size dependence proportional to $1/\mathrm{r}^b$ with $1 < b < 1.5$ rather than

---

*The hydrogen-like state of a bound electron-hole pair, or *exciton*, is characterized for a given crystalline material by its *exciton Bohr radius*,

$$a_B = \frac{\epsilon\hbar^2}{\mu e} = \epsilon\frac{m_0}{\mu} \times 0.53\text{ Å}$$

and its *exciton Rydberg energy*,

$$Ry^* = \frac{e^2}{2\epsilon a_B} = \frac{\mu e^4}{2\epsilon^2\hbar^2} = \frac{\mu}{m_0}\frac{1}{\epsilon^2} \times 13.6\text{ eV}$$

where $\mu = (m_e^{*-1} + m_h^{*-1})^{-1}$ is the reduced mass of the electron-hole pair, ϵ is the dielectric constant of the crystal, m_0 is the rest mass of an electron, and m_e^* and m_h^* are the effective masses of an electron and hole, respectively, in the crystal. Refer to Ref.[36] for a derivation and discussion of these quantities.

$1/r^2$ as in the simplest quantum mechanical model.[37] Such an increase is generally termed a *blueshift*, since the photon energy shifts toward the shorter-wavelength region of the visible spectrum.

In addition to the quantum confinement effect, several recombination mechanisms at radiative centers and non-radiative traps, homogeneous and inhomogeneous broadening, and energy transfer may affect the overall emission spectrum as well.[38] In fact, a variety of theories exist in order to explain the occurring redshift between absorbing and emitting states. For example, proposed Si=O double bonds at the NC-to-SiO$_2$ interface are suspected to form a radiative sub-gap state[39]. A spectral redshift has also been attributed to states caused by Si-O-Si bridging bonds[40], while Daldosso *et al.*[41] have suggested that a redshift might be caused by Si-enriched shell regions that possibly form around the exterior of the nanocrystals. Also, the strained Si-SiO$_2$ interface can result in distortions in the core of the silicon nanocrystals, which in turn may lead to a redshift of the emission energy as shown in theory elsewhere.[42]. The coupling of surface bond vibrational modes to the quantized nanocrystal levels can create a redshift as well[43], and finally nanocrystal-to-nanocrystal interaction can produce additional localized states within the bandgap[44,45] for closely spaced nanocrystals (distances of a few atomic spacings). Possible involvement of some or all of these mechanisms in the luminescence process makes interpretation of Si-nanocrystal spectra difficult, considering that all these mechanisms are strongly influenced by the size distribution and the spacing of the nanocrystals.[46]

1.2.3.2   Amorphous silicon nanoclusters

Similar dependence on size and nanocluster spacing of the emission energies have been observed in nanoscale amorphous silicon (a-Si), which has sometimes been attributed to quantum confinement (QC).[47,48] On the other hand, bandtail-to-bandtail transitions represent the dominant contribution to photoluminescence in amorphous semiconductors and the lack of crystallinity in small amorphous silicon nanoclusters casts doubt on the importance of quantum confinement effects in determining the emission energy.[34,49] One is faced with "an apparent contradiction: evidence for localized transitions versus evidence for a size dependence", implying delocalized transitions.[50] This contradiction can be solved with arguments considering *spatial* - rather than quantum - confinement effects.

The basic principles of the spatial-confinement model as introduced by Estes *et al.*[50] are shown schematically in Fig. 1.4. An electron-hole pair is initially excited into the extended band states of a-Si by absorbing a photon. It then rapidly relaxes to the lowest-energy band-tail states accessible within a capture radius R_c via tunneling. Upon reaching the lowest-energy state available within R_c, the carriers recombine either radiatively (thereby emitting a photon) or non-radiatively in case the carrier diffuses to a quenching center. The diffusion of electrons and holes are assumed to be uncorrelated in this description.[50] Vertical dashed lines in
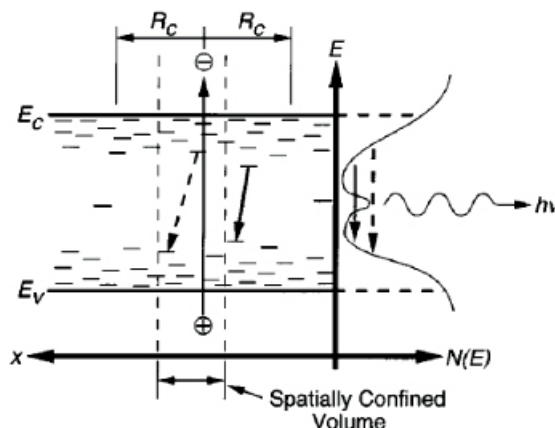
Fig. 1.4: The effect of spatial confinement on emission from a-Si. Photogenerated electron-hole pairs recombine to the deepest available state within a capture radius R_c via tunneling between localized band-tail states. By spatially limiting the recombination volume, the average emission energy and efficiency both increase. (After Refs. [9,50])

Fig. 1.4 demonstrate the effects of small cluster sizes on this process: the accessible capture volume of the bulk material is reduced by spatial confinement in the small a-Si cluster, preventing the carriers from reaching deeper band-tail states, thereby increasing the effective bandgap. Considering this model, the size dependence of amorphous silicon nanoclusters can be understood as a statistical phenomenon. Reduced cluster sizes decrease the probability for a carrier to find a lower-energy state and the emission energy becomes blueshifted.

1.3 Light emission via Er^{3+} ion doping

Rare-earth doped silicon has received much attention as a potential material for fabrication of light sources and optical amplifiers. Optical properties of rare-earth ions in solids have been investigated in great detail and are generally well understood[52,53]. The rare earths, otherwise referred to as lanthanides, comprise the series of the elements in the sixth row of the periodic table of elements from lanthanum to ytterbium. When incorporated in a solid host, rare-earth ions preferably exist in a trivalent oxidation state (3+) and are characterized by a partially filled $4f$ shell that is shielded from external fields by $5s^2$ and $5p^6$ electrons. As a result of this shielding of the 4f electrons, rare-earth electronic levels are influenced much more by spin-orbit interactions than by the external crystal field; the positions of the energy levels are therefore largely insensitive to the environment or host material. Since intra-$4f$ transitions are parity forbidden and are only made partially allowed by crystal-field interactions, luminescence lifetimes are rather long (often in the millisecond range), and linewidths narrow. A detailed account of rare-earth ion energy levels was first published by Dieke *et al.* in 1968[51] and is summarized in a so-called Dieke diagram for the isolated 3+ ions of each of the lanthanides as shown in Fig. 1.5.

In recent years most of the interest in luminescent rare-earth ions has concen-
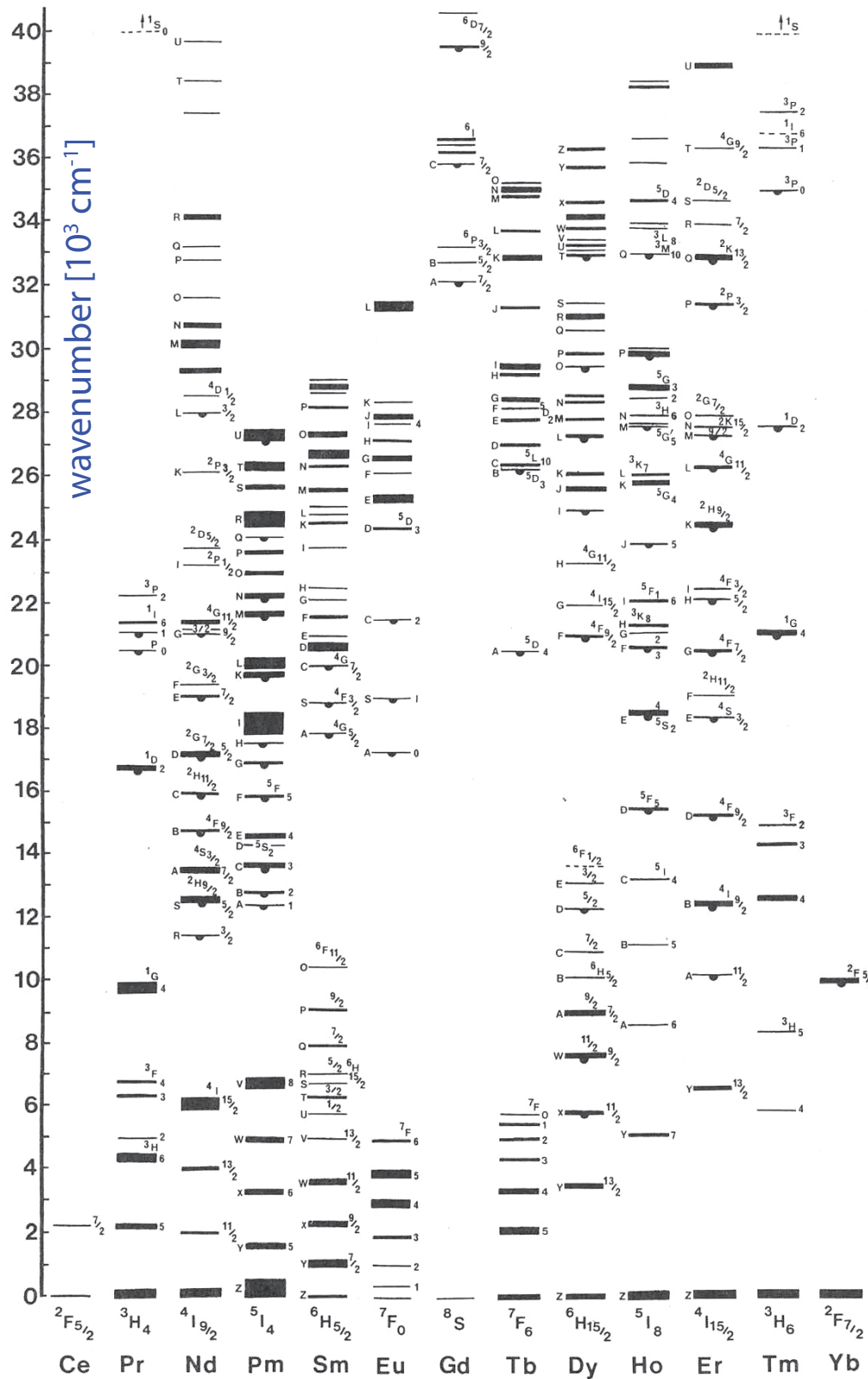
Fig. 1.5: "Dieke" diagram of energy level structure for trivalent rare-earth ions in a crystalline host. The thickness of each line indicates manifolds of levels due to crystal-field splitting; hanging semicircles denote radiative transitions from that level to the ground state. (After Ref.[51])
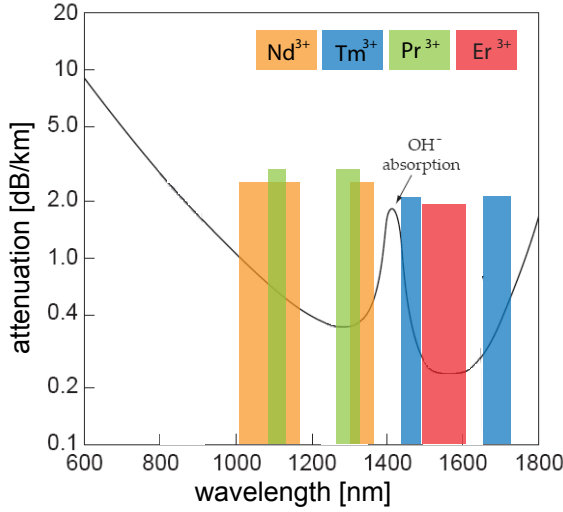
Fig. 1.6: Rare-earth ion emission bands compares to wavelength dependent absorption in SiO_2 .

trated on one species: Trivalent erbium (Er^{3+}). The electronic structure of Er^{3+} is [Xe] $4f^{11}$, with [Xe] representing the closed shell configuration of xenon. Of special interest is the Er^{3+} emission band around 1.54 µm , which is a near-perfect fit to the attenuation minimum of optical fibers as shown in Fig. 1.6.

1.3.1 Er^{3+} electronic configuration

The energy levels and sub-levels of Er^{3+} ions (and any other rare-earth material) are determined by the electronic configuration of the $4f$-electrons and the effects of the surrounding environment on these electrons. A *term symbol* notation of the form $^{2S+1}L_J$ is used to describe and term levels according to the Russell-Saunders coupling scheme for atomic states of multiple electron atoms. Here, L and S are the orbital and spin contributions to the total angular momentum, J. For a free ion with N electrons, the operators L and S are given by

$$L = \sum_{k=1}^{N} l_k \tag{1.2}$$

and

$$S = \sum_{k=1}^{N} s_k \tag{1.3}$$

where l_k and s_k are the orbital and spin operators of the kth electron and the value of L is converted into a letter according to the same code as is used for the s, p, d, ... designations of atomic orbitals. Therefore $L = 0, 1, 2, 3, 4, 5, 6, 7, 8, 9, 10... =$ S, P, D, F, G, H, I, K, L, M, N ... and so on. Given the total spin S, the multiplicity is calculated as $2S + 1$. For example in case of a level with parallel spin: $S = \frac{1}{2} + \frac{1}{2} = 1$

Spin-orbit split:

$^4I_{9/2}$

Isolated level:

$^4I_{11/2}$

Stark split:
crystal field,
local coordination

~200-400 cm^{-1}

$^4I_{13/2}$

Inhomogeneous broadening:
site-to-site difference of crystal field

~ 27-60 cm^{-1}

^4I

Homogeneous broadening:
thermal fluctuation

~ 8-49 cm^{-1}

$^4I_{15/2}$

20~80 cm^{-1}
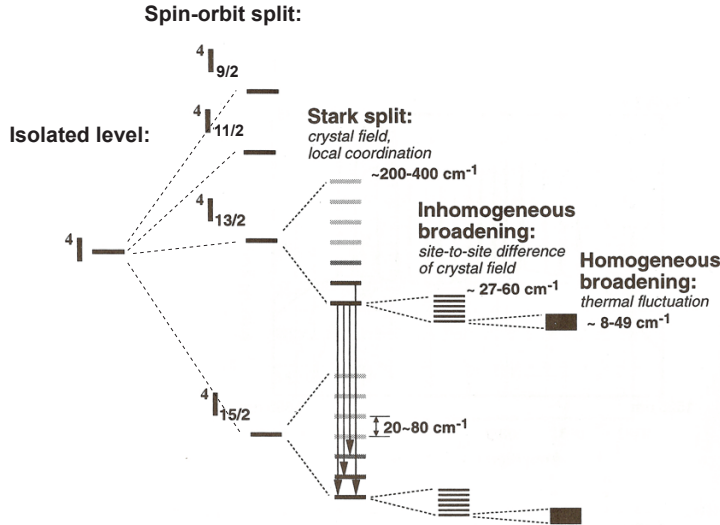
Fig. 1.7: Schematic of different energy level splitting mechanisms for the Er^{3+} ion ^4I state. Spin-orbit splitting, and the Stark split due to the crystal field create a number of sub-levels. Inhomogeneous broadening due to site-to-site difference (see Fig.**??**) and homogeneous broadening caused by thermal fluctuations create overlaps of closely spaced levels in a manifold, resulting in quasi continuous bands. (After Ref.[54])

and $2S + 1 = 3$, this would be a triplet. Finally, the total angular momentum quantum number J is given by

$$J = L + S, L + S - 1, ..., |L - S| \tag{1.4}$$

Electrostatic interaction of the $4f$-electrons define isolated atomic energy levels such as ^4I, ^4F, ^4S, and ^2H. Spin-orbit coupling between the electron's spin and the nucleus's electric field causes these atomic levels to split into different sub-levels, which are sharp for a free ion. Placed in a crystal field (i.e. a solid) however, each sub-level is split further into a manifold of more closely spaced sub-levels as illustrated in Fig. 1.7. This effect is called *Stark splitting* in case of an external electric field and *Zeeman splitting* in case of an external magnetic field, and will hereafter be termed *crystal-field splitting*. In glass materials, the electrostatic interaction between ions and lattice is dominant, and crystal-field splitting is therefore caused by the Stark effect. The number and spacing of split sub-levels depend on the total angular momentum, J, and the magnitude of the local electric field, which in turn depends on the position of the Er^{3+} ions within the host matrix. For the Er^{3+} ground level $^4I_{15/2}$ crystal-field splitting creates a maximum of $(2J+1)/2 = 8$ levels, whereas for the first excited state $^4I_{13/2}$ a maximum of 7 levels are formed.

At thermal equilibrium, the levels in each manifold are populated according to a Boltzmann distribution (indicated by different shades of gray in Fig.1.7); the ratio of populations (N_a, N_b) of any two levels (a, b) created by crystal-field splitting depends on the energy difference $(E_b - E_a)$ between the levels and the absolute
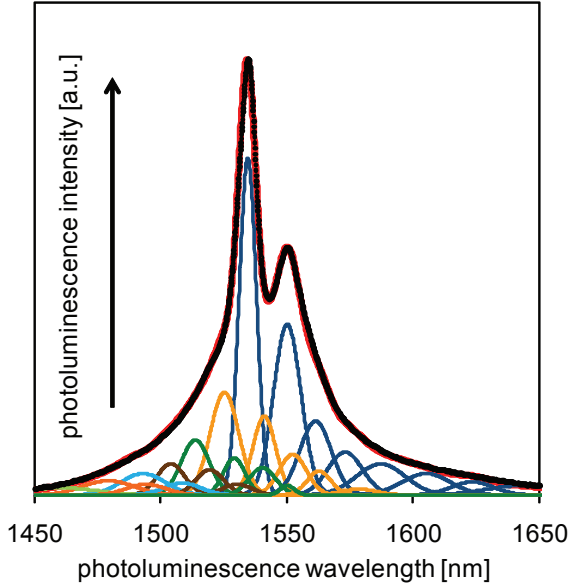
Fig. 1.8: Erbium emission spectrum from a SiO:Er waveguide pumped at 980 nm. The spectrum is fit with gaussian functions representing different transitions between sub-levels created by crystal-field splitting. Blue gaussian curves represent transitions from the lowest sublevel in the $^4I_{13/2}$ manifold to each of the levels in the $^4I_{15/2}$ manifold, yellow curves represent transitions from the next higher level in the $^4I_{13/2}$ manifold to the ground levels, and so on (see details in appendix C).

temperature T in degree Kelvin, and is given by

$$\frac{N_a}{N_b} = \exp\left(\frac{E_b - E_a}{k_B T}\right) \tag{1.5}$$

where k_B is Boltzmann's constant (8.617 x 10^{-5} eV/K).

Optical transitions between the first excited state and the ground state of Er^{3+} can in theory take place between any two levels, one from each manifold, resulting in a total of 56 possible transitions with different energies or wavelength, respectively. Inhomogeneous broadening due to site-to-site differences in the crystal field and homogenous broadening due to thermal fluctuations further broaden each sub-level, creating nearly continues bands as observed in the emission spectrum in Fig. 1.8. Here, the luminescence spectrum of the $^4I_{13/2}$ to $^4I_{15/2}$ Er^{3+} transition obtained from experiment (black) is fitted by the sum (red) of different gaussian curves, each representing one possible transition from the upper to the lower manifold. Blue curves, for example, represent transitions from the lowest crystal-field split level in the upper $^4I_{13/2}$ manifold to each of the crystal-field split levels in the ground state manifold, starting with the strongest transition to the 'absolute' ground (E=0) with a wavelength around 1.534 μm . Transitions to levels of higher energies are less intense, following the exponential decrease in population density given by the Boltzmann distribution. The same can be observed for transitions from higher levels in the upper manifold to the ground state levels, shown in yellow, green, brown, cyan, and orange in Fig. 1.8.

1.3.2 Er^{3+} in bulk crystalline silicon

At low temperatures, luminescence originating from the radiative transition from the $^4I_{13/2}$ energy level to the $^4I_{15/2}$ ground level is readily observed from Er^{3+} ions embedded in silicon. Excitation of the Er^{3+} ions is sensitized by the silicon host through a carrier-mediated process after an electron-hole pair is generated by an impinging photon with an energy greater than the bandgap, and an exciton becomes trapped at a erbium related trap site. Erbium ions can then be excited via energy transfer from recombining electron-hole pairs[53](the physical mechanisms of the energy transfer will be outlined later). However, room temperature photoluminescence from erbium-doped silicon presents a considerable technical challenge, due to the presence of strong temperature quenching effects. These include backtransfer, in which an excited Er^{3+} ion transfers energy back to the silicon, and the impurity Auger effect, in which the erbium transfers energy to a free carrier in the conduction or valence band of the silicon.[53] Another problem is the relatively low solubility ($\sim 2 \times 10^{16}$ cm^{-3}) of Er^{3+} ions in crystalline silicon. A combination of ionic radii mismatch and the sp^3 bonding of the silicon host means that it is difficult to incorporate high concentrations of erbium in crystalline silicon by equilibrium techniques such as thermal diffusion. Amorphous Si (*a*-Si) and SiO$_2$ can accommodate much higher Er^{3+} concentrations due to their random network and defect structure.

1.3.3 Er^{3+} co-doped Si-nanoclusters in SiO$_2$

The discovery of efficient energy transfer from silicon nanocrystals to rare-earth ions has sparked increased interest in hybrid material systems containing both Si nanocomposites and rare earths - particularly Er^{3+} - embedded in a SiO$_2$ host in order to achieve light emission in the technologically important wavelength region around 1.54 µm[55,56]. A schematic of this sensitization process is shown in Fig. 1.9. Materials containing both Si-NC and Er^{3+} ions take advantage of the relatively large absorption cross section of silicon ($\sim 10^{-16}$cm^2) as compared to the very small excitation cross section for resonant excitation of Er^{3+} ions ($\sim 10^{-21}$cm^2); a difference of about 5 orders of magnitude. Furthermore, Si-NC absorb over a broad wavelength range in the visible and UV, bypassing the requirement of expensive high power pump lasers.

Beyond certain critical concentrations, rare-earth ions tend to form precipitates (so-called 'clusters') in most solid hosts. Such clusters quench the luminescence from Er^{3+} ions due to increased rates of non-radiative ion–ion interactions. Besides supporting a much higher solubility of erbium ions as compared to Si, SiO$_2$ as a host material also supplies the oxygen atoms for the Er^{3+} ions to be coordinated in a sixfold C_{4v} symmetry with oxygen, which is the local structure of an optically active center. Additionally, incorporation of oxygen significantly increases the energy barrier for backtransfer and impurity Auger effects due to an increased
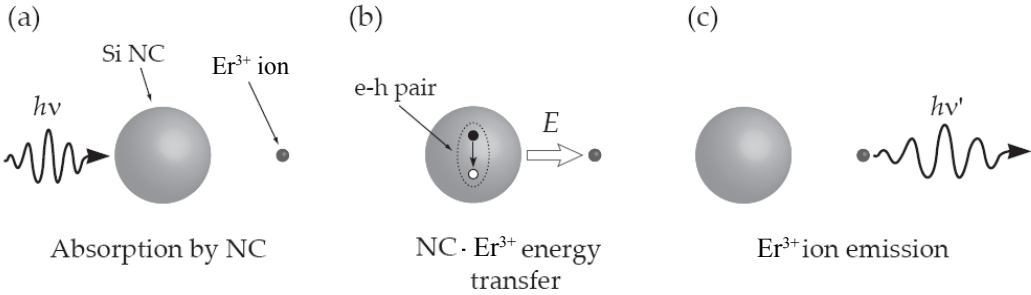
Fig. 1.9: Schematic of the simplified sensitization process between Si-NC and Er^{3+} ion. In (a), and incident photon is absorbed by the nanocluster, exciting an electron-hole pair. This electron-hole pair recombines non-radiatively and thereby transfers its energy to the Er^{3+} ion as shown in (b). Finally, the Er^{3+} ion emits light with a wavelength corresponding to its characteristic energies in (c). (After Ref. [9])

bandgap with respect to bulk silicon, enabling efficient luminescence even at room temperature[57,58]. General features of the luminescence from Er^{3+} and other rare-earth ions in Si-NC sensitized materials are:

- For a given pump intensity, the rare-earth emission is much more intense than luminescence observed in a pure SiO_2 host or in bulk crystalline silicon

- The emission spectrum suggests that light is emitted from ions embedded in the SiO_2 host, not in the silicon nanocluster

- The rare-earth-related luminescence may have only a weak dependence on temperature

- Increasing the rare-earth concentration leads to an increase in rare-earth related emission intensity (up to a point where concentration quenching becomes dominant) , whereas the luminescence from the Si-NC is quenched

Nevertheless, many details, such as the exact nature of the energy transfer from Si nanocrystals to Er^{3+} ions, as well as its characteristic rate[59–62], the characteristic transfer distance[63–65], and the maximum number of Er^{3+} ions sensitizable per nanocrystal[66,67] - just to mention a few of the most important - are still uncertain.

Most recent studies of Er-doped silicon nanocomposites have relied on thermal processing on the order of 1000°C or more to induce phase separation in silicon-rich oxides (SRO), temperatures incompatible with standard complementary metal oxide semiconductor (CMOS) fabrication processes. Despite this significant barrier for monolithic integration, considerably less attention has been brought to materials in which the Er^{3+} ions are sensitized via amorphous silicon nanoclusters, requiring much lower processing temperatures on the order of 400°C to 600°C . Amorphous Si-NC exhibit comparable luminescent properties to their crystalline

counterparts, and have been shown to sensitize Er^{3+} via an efficient energy transfer. In fact, it has been reported recently, that amorphous silicon clusters with a size of around 2 nm in diameter in erbium co-doped SRO sensitize Er^{3+} ions even more effectively than Si-nanocrystals[68,69], resulting in a higher luminescence yield and possibly increasing the chance to obtain optical gain in these materials.

1.4 Energy transfer and sensitization

The efficient energy transfer mechanism between silicon nanoclusters and Er^{3+} ions is the reason for the strong research interest in these co-doped materials. But besides the fact that the exact nature of this sensitization process is not resolved in detail, various other interactions - such as NC-NC interactions and Er^{3+} -Er^{3+} interactions - must be considered, which in general behave as loss mechanisms and are therefore undesirable for optical amplification.

1.4.1 Transfer mechanisms

The three fundamental energy transfer mechanisms present in the NC-Er^{3+} system are: radiative energy transfer, multi-polar Coulomb (Förster) energy transfer, and the energy transfer via overlapping wavefuntions (or Dexter energy transfer), each of which exhibits a characteristic energy transfer rate depending on NC size and/or spacing.

1.4.1.1 Resonant radiative transfer

In this process, radiative recombination of the donor (D) creates a real photon of energy $h\nu$. The emitted photon can then be absorbed by an acceptor (A) with a level of equal energy, exciting it to the matching state. The efficiency of such a process is determined by the absorption cross-section of the acceptor, the transfer rate of this process scales with the separation distance, R, between D and A as[9,70]

$$w_{\mathrm{tr}} = w_{\mathrm{pl}} \frac{\sigma_A}{4\pi\mathrm{R}^2} \int g_D(\nu) \, g_A(\nu) \, d\nu,\tag{1.6}$$

where σ_A is the absorption cross-section of A, w_{pl} is the donor photoluminescence rate, and $g_D(\nu)$ and $g_A(\nu)$ are the donor emission spectrum and acceptor absorption spectrum, respectively. The rate for this direct photon transfer shows a $1/\mathrm{R}^2$ dependence.

1.4.1.2 Multi-polar Coulomb transfer

The second fundamental interaction mechanism is a non-radiative multi-polar energy transfer first described by Förster[71] for the case of dipole-dipole transfer. Interactions of this sort are often referred to as *Förster transfer*. In this mechanism,

electron-hole pairs migrate from the donor (D) to acceptor (A) by a dipole-dipole or higher-order multipole coupling. The transfer rate in the dipole-dipole case depends on the separation distance, R, between D and A as

$$w_{tr} = w_{pl} \left(\frac{R_0}{R} \right)^6 ,$$ (1.7)

where w_{pl} again is the donor photoluminescence rate, and R_0 is the distance at which $w_{tr} = w_{pl}$. Considering dipole-quadrupole interactions one would simply replace the 6 in the exponent with an 8, and so on.[72] R_0 itself depends on the spectral overlap integral between donor (D) and acceptor (A). In the Miyakawa-Dexter theory[73], the resonant Förster transfer rate is modified by accounting for electron-phonon coupling parameters in the density of states functions of D and A, allowing for phonon-assisted non-resonant transfer with a rate[73]

$$w_{tr} = w_{pl} \left(\frac{R_0}{R} \right)^6 \times \exp\left(-\beta \Delta E\right) ,$$ (1.8)

where β depends on the electron-phonon coupling strength, and ΔE represents the energy mismatch between donor and acceptor state.

1.4.1.3 Overlapping wavefunction transfer

If donor (D) and acceptor (A) are very closely spaced, the probability for energy transfer due to electron exchange effects can become close to unity as a result of the overlap of the electron wavefunctions of donor and acceptor[72] - the so-called *Dexter transfer*. The transfer rate for the the Dexter mechanism is given by[74]

$$w_{tr} = w_0 \exp\left(-b R\right) ,$$ (1.9)

where w_0 is a prefactor, and b is a constant equal to $2/L$, with L being the sum of the mean van der Waal's radii for the D and A states (e.g. ~ 0.4 nm for Si and Er).

1.4.2 Nanocluster - nanocluster interactions

Closely spaced nanoclusters (NCs) can exchange charge carriers via at least two fundamental mechanisms[37], single-carrier tunneling and the Förster-type multipole coupling. Typically, phonon-assisted energy transfer is considered in the latter case, namely the Miyakawa-Dexter[73] theory described previously. Both of these energy migration mechanisms depend more strongly on the distance between the interacting NCs, as opposed to the strong dependence on NC size seen in radiative and non-radiative decay rates.

The transfer rate for single-carrier tunneling can be approximated by a Wentzel-Kramers-Brouillin (WKB) approximation for NCs with nearly the same size (i.e.

matched energy levels - resonant condition), and can be written as[75]

$$
\begin{aligned}
w_{\text{tunnel}} = {} & \left(\frac{1}{2d_{\text{p}}}\right) \left(\frac{2E}{m_{\text{p}}}\right)^{1/2} \frac{16E\,(V-E)\,(m_{\text{p}}/m_{\text{b}})}{\left[V + (m_{\text{p}}/m_{\text{b}} - 1)\,E\right]^2} \\
& \times \exp\left[-2d_{\text{b}}\left(\frac{2m_{\text{b}}\,(V-E)}{\hbar}\right)^{1/2}\right],
\end{aligned}
\tag{1.10}
$$

where m_{p} and m_{b} are the carrier effective masses in the barrier and the particle, d_{p} and d_{b} are the particle diameter and barrier thickness, V is the barrier height, and E is the carrier energy. For close distances the tunneling rates are high, but rapidly decrease below other transfer rates (e.g. Förster-type) for NC separations greater than ~ 3 nm.[38] In most cases the energy levels of adjacent NCs are mismatched, tunneling must then be assisted by phonon emission or absorption, causing the tunneling rates to decrease approximately exponentially over a range of ΔE.

1.4.3 Ion - ion interactions

Rare-earth ions in a solid host exhibit a strong characteristic tendency to ion-ion interactions.[52] Several energy transfer processes between a donor ion (D) and an acceptor ion (A) are shown in Fig. 1.10. The sensitization processes illustrated in (a) and (f) indicate radiative energy transfer (solid arrows); i.e. the donor ion emits a photon with energy $h\nu$ which is then absorbed by the acceptor ion possessing a matching energy level. Energy transfers in (b) to (e) on the other hand (dashed arrows) are non-radiative transitions, such as Förster or Dexter transfer as described above.

Fig. 1.10(b) shows a non-radiative but resonant sensitization process between two ions with matching energy levels. This energy transfer may be welcome and beneficial as is the case of Er^{3+} ions sensitized by Yb^{3+} ions, or unfavored when Er^{3+} ions transfer energy between themselves, resulting in a diffusion of energy throughout the ensemble. This process is often referred to as *pair-induced quenching* or *excitation migration*[53,76]. Phonon assisted non-resonant transfer (e.g. of the Miyakawa-Dexter type) is depicted in Fig. 1.10(c); here energy transfer occurs between mismatched energy levels of different ions, the discrepancy in energy, ϵ, is compensated by the creation or annihilation of phonons.

Interactions between identical rare earth ions (D = A, e.g. both donor and acceptor are Er^{3+}) as shown in (d) are often referred to as *cross-relaxation* processes.[9] Here, an excited ion transfers part of its energy to another ion in the ground state, so that both end up in some intermediate level.

At high concentrations of rare-earth ions, interaction between these ions can become a significant gain limiting effect. One such process is commonly known as *co-operative upconversion*[52,76] and is shown schematically in Fig. 1.10(e). In this process, an excited Er^{3+} ion de-excites by transferring its energy to another neigh-
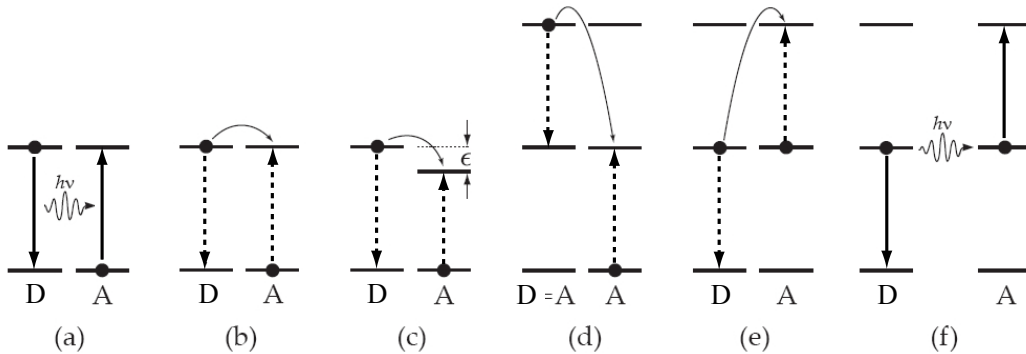
Fig. 1.10: Schematic representations of various Er^{3+} -Er^{3+} interactions. Solid arrows denote radiative transitions involving absorption or emission of a photon, whereas dashed arrows represent non-radiative transitions due to an electrostatic, magnetostatic, or exchange interaction between D and A. Type (a) illustrates the resonant radiative energy transfer, a photon is emitted by D and thereafter absorbed by A. In (b), the process is non-radiative (e.g. Förster type transfer), whereas (c) shows the non-resonant version of (b): the energy difference ϵ is accounted for by the creation or annihilation of phonons. Two identical ions may interact by relaxing both to excited states as illustrated in (d), or if both already are excited, D may relax to the ground state and excite A to a higher excited state as shown in (e). In (f), D recombines radiatively, emitting a photon that is absorbed by A, exciting it into a higher level. (After Refs.[9,52,70])

boring excited Er^{3+} (in the $^4I_{13/2}$ level), promoting it into the $^4I_{9/2}$ level. This effect lowers the amount of excited erbium and in turn increases the pump power needed to achieve population inversion. Co-operative upconversion is only present in systems possessing a resonant level at twice the energy of the first excited state, as is unfortunately the case for the $^4I_{13/2}$ and $^4I_{9/2}$ levels of Er^{3+} ions, limiting the gain in Er-doped systems for concentrations above $10^{19} - 10^{20}$ Er/cm^3.

Graph (f) shows yet another gain limiting effect known as *excited state absorption* (ESA).[76] In this process, an already excited Er^{3+} acceptor ion absorbs a real photon, exciting it into a higher state. The photon may be originating from the signal to be amplified or the pump and therefore affects both maximum possible gain and excitation efficiency. Several authors[77,78] refer to the effect described in (e) as *excited state absorption* as well, but the use of the term 'absorption' in this context is misleading, since no real photon is actually absorbed, but the Er^{3+} ion is rather brought to a higher excited state by means of a Förster- or Dexter-type energy transfer.

1.4.4 Nanocluster to Er^{3+} energy transfer

By employing Si-NCs as sensitizers for the optically active erbium in the material, the absorption cross-section of the Er^{3+} ions - normally on the order of 10^{-20} cm^2 - effectively becomes similar to that of the nanoclusters (around 10^{-16} cm^2), four orders of magnitude higher.[79] However, the nature of the energy transfer has long been unclear and vigorously debated.

In general, all three energy transfer mechanisms (radiative energy transfer, multipolar coulomb transfer, and transfer via overlapping wavefunctions) must be con-
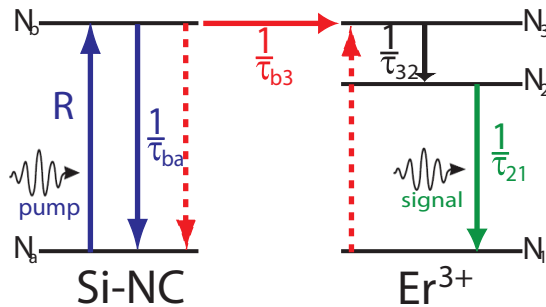
Fig. 1.11: Schematic diagram of the Si-NC-Er^{3+} population dynamics model. A two-level Si-NC system is sensitizing a three-level Er^{3+} system via energy transfer.

sidered between a silicon nanocluster donor and a trivalent erbium ion acceptor.[80] In practice, resonant radiative transfer is rather unlikely, due to the high absorption coefficient of silicon at the wavelengths generally used for optical excitation and the simultaneously rather small absorption cross-section of erbium.

Several authors[63–65,81] report an exponential decrease in transfer efficiency with increasing distance, yielding characteristic interaction lengths of about 0.5 nm for a-Si-NC[63] and approximately 2.1 nm for Si nanocrystals[64]. By extending the point-to-point model to interactions between a thick plane of donors and a thick plane of acceptors, and comparing the derived model with experiment, our group has recently shown[80] that the characteristic transfer distance between c-Si-NC and Er^{3+} ions can be rather large, as long as 6 to 7 nm. Although both Förster and Dexter transfer mechanisms can be fit to the data, this long sensitization distance corresponds to un-physically long-range interactions for energy transfer via overlapping wavefunctions. Other authors[82,83] have found further indicators of quasi-resonant Förster-type energy transfer in spectroscopic experiments.

1.4.5   Energy transfer modeling in the NC-Er^{3+} system

For the development of viable erbium-doped waveguide amplifiers (EDWAs) and lasers a thorough understanding of the population dynamics in the Si-NC-Er^{3+} system is essential; in particular, the maximum output power is limited by the energy transfer rate between the Si-NC and the Er^{3+} ions. Numerous models of varying complexity have been proposed to describe the population dynamics of a NC-Er^{3+} system[77,84], including efforts to determine the relative importance of several gain-limiting processes. The most elaborate model of such a system to date, including ion-ion interactions such as co-operative upconversion, was published by Pacifici *et al.*[84] in 2003.

Due to the large number of free parameters, fitting to experimental data is difficult and results in calculated transfer rates and cross-sections differing by several orders of magnitude in some cases.[77,84,85] Models generally consist of a simplified system (e.g. by ignoring Er^{3+} - Er^{3+} interactions), including a two-level Si-NC system coupled with a three-level Er^{3+} system as shown schematically in Fig. 1.11.

The determination of characteristic transfer rates and cross-sections through experimental work is imperative, in order to gain further understanding of the Si-NC and Er^{3+} system and to improve model accuracy. Also of great interest is the reduction of gain limiting processes by optimized means of sample preparation.

1.5   Thesis objectives

In this thesis, I will address several of the issues that currently appear to limit or prevent Er^{3+}-doped silicon nanocrystals as reliable gain media. I will also investigate the optical properties and photoluminescence behavior of amorphous Si-NC composites doped with Er^{3+} - a material that has seen little previous work compared to the vast body of literature on Si nanocrystals. Specific objectives include:

- Optimizing the sample preparation process via PVD to enable simultaneous deposition of a wide range of SiO_x:Er compositions with best possible control.

- Investigation of the influence of SiO_x:Er composition on the energy transfer efficiency between Si-NCs and Er^{3+} ions. By covering a wide range of excess Si concentrations and annealing temperature, I aim to find optimum conditions for the sensitization process.

- A better understanding of the fundamental nature and characteristics of the energy transfer between the Si-NCs and Er^{3+} ions through photoluminescence spectra and dynamics measurements.

- Fabrication of optical waveguides based on SiO_x:Er and other CMOS compatible materials. The goal is to investigate alternative techniques for fabrication of waveguides based on SiO_x:Er materials, including design and testing of these optical waveguides.

- Investigation of absorption and emission behavior of SiO_x:Er waveguides in different excitation schemes. Estimation of critical cross-sections and transfer rates is possible from such measurements.

CHAPTER 2

SiO$_x$:Er photoluminescence and Er^{3+} sensitization

2.1 Introduction

Many details concerning the energy migration processes in Er-doped silicon NC systems are still not entirely understood. Fabrication parameters, including excess silicon concentration, erbium concentration, annealing temperature, and the synthesis technique itself may influence the sample microstructure and thereby its potential as a gain medium. Several authors have reported enhanced sensitization efficiencies for amorphous Si-NC sensitizers versus Si nano-crystals.[68,69] In this work, a straightforward approach was developed to map photoluminescence efficiency for a wide range of SiO$_x$:Er compositions. In addition to describing the deposition details, I also describe experiments to assess their optical properties, followed by a discussion of the results.

2.2 SiO$_x$:Er film fabrication

Materials comprising silicon nanoclusters and Er^{3+} ions embedded in a host of SiO$_2$ or SRO (silicon-rich-oxide) can be fabricated in a variety of ways. Often, ion implantation is used to introduce the desired percentage of excess silicon into a SiO$_2$ substrate, followed by subsequent implantation of Er^{3+} ions.[86,87] Other common techniques are plasma enhanced chemical-vapor deposition (PECVD)[88], thermal co-evaporation[31,89], co-sputtering[26,90], and laser ablation[58] of SiO$_2$ and SiO. Compositions typically range from SiO to SiO$_2$ doped with 0.04 to 2.5 at.% of erbium, depending on the fabrication technique and desired stoichiometry. Silicon nanoclusters (Si-NC) are subsequently produced by annealing (i.e. thermal processing) the deposited SiO$_x$ films at sufficiently high temperatures to cause a phase separation process.[91,92]
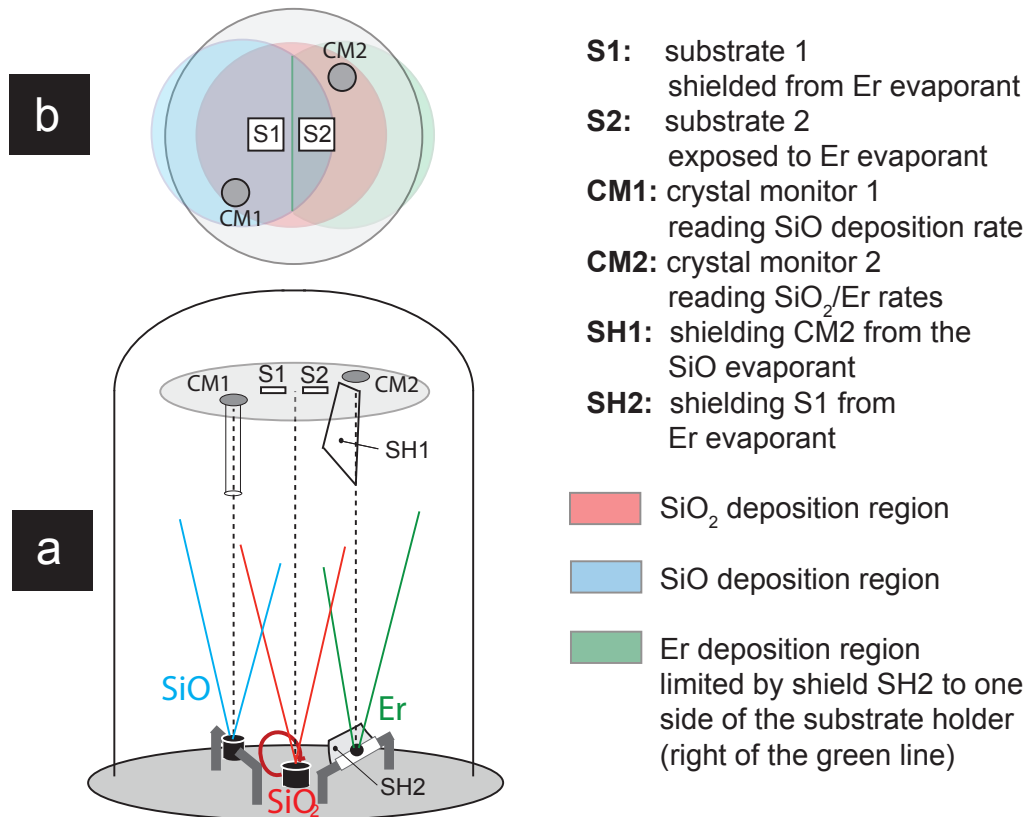
Fig. 2.1: Schematic view of the physical vapor deposition (PVD) system. (a) Schematic of the bell jar including the three material sources (SiO, SiO$_2$, Er) used to deposit SiO$_x$:Er thin films. Also shown is the substrate level with two substrates and two crystal monitors with shielding in place. (b) features a top view of the substrate level, illustrating the shadowing of S1 from the Er source by the shield SH1, which results in an undoped sample S1 and an Er-doped sample S2.

2.2.1 Physical vapor deposition

Physical vapor deposition (PVD) by thermal evaporation or sputtering is a versatile approach to form Er-doped silicon nanocomposites. Generally, the source material is heated to its melting or sublimation point by conductive heating or an impinging electron beam, and the resulting flux of vaporized material condenses on a substrate positioned within the line-of-sight of the source.

2.2.1.1 Deposition system

The SiO$_x$:Er thin films in this work were deposited in a high-vacuum physical vapor deposition (PVD) system as shown schematically in Fig. 2.1 (a). In order to deposit SiO$_x$:Er thin films with a variety of compositions, the system is equipped with an electron-beam evaporator unit and two separate holders for thermal vaporization. This setup enables simultaneous evaporation of up to three source ma-

terials. Here, Silicon monoxide (SiO - 99.9% pure, Kurt J. Lesker Company), silicon dioxide (SiO_2 - 99.999% pure, Kurt J. Lesker Company), and erbium metal (Er - 99.9% pure, Cerac Inc.) were the source materials. SiO was thermally evaporated via resistive heating from a "baffled box" source, SiO_2 was obtained by electron beam evaporation, and the Er was vaporized in a tantalum boat through resistive heating.

The deposition rates and thicknesses of deposited films were determined *in situ* by two independent crystal monitor sensors (CM1 & CM2) placed at opposite ends of the centered substrates (S1 & S2), as illustrated in Fig. 2.1. In order to control the SiO_x:Er film composition during deposition, evaporation rates have to be monitored via the crystal monitors separately; i.e. only the flux from one source reaches each crystal monitor. When operating at high-vacuum (base pressure: $7 - 8 \times 10^{-7}$ Torr) a long mean-free-path is possible*, so that the evaporants reach the substrates and the crystal monitors having traveled in a straight line. Shields were put into place to block the line-of-sight between the sources and the monitors as depicted in Fig. 2.1 (a); a tube was used to ensure CM1 only receives flux from the SiO source, whereas a flat shield (SH1) was positioned to block the flux from the SiO source, but allow vaporized material from the SiO_2 and Er sources to reach CM2. An additional shield (SH2) was affixed to the Er source in such a way as to prevent deposition of erbium on substrate S1 as illustrated (green area) in Fig. 2.1 (b). This setup allows for deposition of both Er-doped and undoped samples (which are otherwise equivalent) with relatively good control over film stoichiometry and thickness, as determined by Rutherford backscattering spectroscopy (RBS).

2.2.1.2 Procedures

Since only two crystal monitors are available in the system to monitor three sources, the following procedure was put in place to maintain a constant Er deposition rate for each film.

After the system was evacuated to base pressure ($\sim 7 - 8 \times 10^{-7}$ Torr), the Er source was heated up first and its deposition rate (typically 0.025 Å/s) was adjusted using the readings from CM2. Next, the deposition rates for SiO and SiO_2 were set using CM1 and CM2, respectively; the combined rate of SiO and SiO_2 were set to 10 Å/s (e.g. 5 Å/s SiO + 5 Å/s SiO_2 for $SiO_{1.5}$). Note that CM2 will display the sum of SiO_2 and Er evaporation, but the Er rate is negligibly small and did not effect the measured SiO_2 rate. Only when all sources are running stably with the desired rates was the shutter protecting the substrate opened and deposition initiated.

---

*For a pressure of 7.5×10^{-6} Torr, the mean free path of gas molecules is on the order of 6.6 m, greatly exceeding typical source–substrate distances and causing most evaporated species to reach the substrate via a straight-line, collision-free trajectory.[93]

x (O : Si ratio)	excess Si (at.%)	thickness (nm)	Er^{3+}
1	25.0	190	yes
1	25.0	185	no
1.2	18.2	205	yes
1.2	18.2	200	no
1.4	12.5	200	yes
1.4	12.5	210	no
1.6	7.7	220	yes
1.6	7.7	215	no
1.8	3.6	210	yes
1.8	3.6	210	no

Table 2.1: Composition list of sample films on a SiO_2 substrate.

2.2.1.3 Summary of fabricated sample films

For the photoluminescence measurements in this chapter, a series of SiO_x:Er samples with a nominal layer thickness of 200 nm was deposited on silica (SiO_2) substrates as listed in table 2.1. Actual thickness values were determined by a stylus instrument. SiO_x compositions (i.e. the ratio of oxygen to silicon atoms) were chosen to range from $x = 1$ to $x = 1.8$ (see table 2.1) by adjustment of the respective evaporation rates of the SiO and SiO_2 sources via independent crystal rate monitors. Conversion between the compositional value x = [O]/[Si] and the atomic fraction of excess silicon $[Si]_{excess}$ in a SiO_2 host is readily obtained via the relation[94]

$$[Si]_{excess} = \frac{1 - x/2}{1 + x}, \quad \text{or inversely} \quad x = \frac{1 - [Si]_{excess}}{0.5 + [Si]_{excess}}. \tag{2.1}$$

Two specimens of each SiO_x composition, one with erbium and one without, were deposited at the same time by blocking the latter sample from the vapor flux coming from the erbium metal source as described before. Except for the difference in erbium concentration, both samples possess nearly equal thickness and stoichiometry, enabling comparison between Er-doped and undoped medium. The Er concentration in the Er-doped set of samples was maintained at about 0.2 at.%, or $\sim 1 \times 10^{20}$ cm^{-3}, since previous work in our group[95] concerning Er-doping of silicon-monoxide (SiO) has shown maximum Er^{3+} PL for this concentration, which is also in good agreement with values obtained for erbium-doped SiO_2 .[96]

Additional films with varying compositions and film thickness (listed in table 2.2) were deposited on silicon and SiO_2 ($\sim$ 2 µm)-coated silicon substrates to be used in the subsequent waveguide fabrication processes described later. These specimens were used to measure the refractive indices of the different compositions and to determine temperature-dependent change in the photoluminescence intensity and dynamics. Since the placement of samples in the cryostat chamber makes collection of PL more difficult, films of greater thickness were preferred as they provide stronger emission. The silicon substrate also possesses excellent thermal conductivity, improving the cooling and warming processes of the film samples

within the cryostat.

x (O : Si ratio)	excess Si (at.%)	thickness (μm)	Er^{3+} (at.%)
1	25.0	0.5	0
1	25.0	0.8 - 1.0	~ 0.2
1	25.0	1.0	~ 1
1.5	10.0	0.5	0
1.5	10.0	0.5	~ 1
1.5	10.0	1	~ 0.2
1.7*	5.56	1.65	0.12

Table 2.2: List of specimens on silicon substrate deposited to measure refractive indices and as core material for SiO_x:Er waveguides.

2.2.2 Annealing and phase segregation

Following the deposition, all samples were annealed in a mixture of 95% N_2 and 5% H_2 - so-called *forming gas*[†] - to induce phase separation of Si and SiO_2, promote nanocluster growth, and to cause the Er^{3+} ions to become optically active. Specimens from table 2.1 were annealed at temperatures ranging from 400 to 1100°C in intervals of 100°C for periods of 1 hour at each temperature. The structural evolution of SiO_x upon annealing undergoes three basic stages[19]:

i) As-deposited SiO_x films (i.e. after the deposition but before the first annealing step) are completely amorphous and consist of a homogeneous glassy mixture of Si and O containing a high number of defect centers.

ii) Annealing at a sufficiently high temperature ($T_{anneal} > 400°C$) induces a phase separation process, separating the two energetically favorable phases of SiO_2 and Si:

$$SiO_x \xrightarrow{\text{anneal}} \frac{2-x}{2}Si + \frac{x}{2} SiO_2, \qquad 0 < x < 2 \qquad (2.2)$$
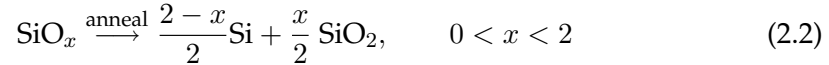
Silicon-rich clusters embedded in a SiO_2 -rich matrix form and grow with increasing T_{anneal} but remain amorphous up to an annealing temperature of about $800 - 900°C$.

iii) For annealing temperatures exceeding about 900°C (in the case of SiO), the silicon-rich clusters crystallize.[19] Annealing at higher temperatures increases the crystal size and decreases the excess Si content remaining in the SiO_2 matrix.

---

[*]Rutherford backscattering spectroscopy (RBS) has determined an oxygen-to-silicon ratio of $x = 1.98$ for this film.

[†]Most commonly, a N_2 gas atmosphere is used for the annealing process, but improved PL characteristics via annealing in a hydrogen enriched atmosphere have been evidenced[97,98], generally attributed to passivation of dangling bonds at the Si/SiO_x interface. Size and density of the formed silicon nanoclusters depend on the initial film stoichiometry (i.e. excess Si concentration), the annealing temperature, and the annealing duration[99].
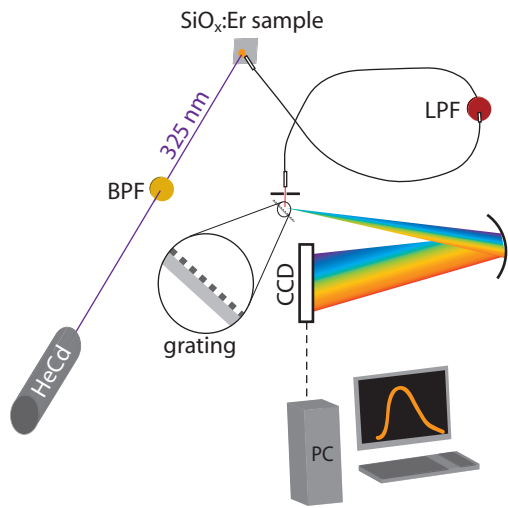
Fig. 2.2: Experimental setup used to measure photoluminescence spectra and intensities. The laser wavelength is 325 nm. Photoluminescence from either the Si-NC or the Er^{3+} ions is collected via an optical fiber and delivered to a spectrometer, where spectra are recorded by a CCD array.

2.3   Experimental: Photoluminescence measurements

This section overviews the experimental setups used to determine photoluminescence spectra and intensities, dynamics, and temperature dependent behavior. Different lasers were used for excitation of the Si-NCs in the material, depending on desired pump power and wavelength. Also, a variety of detectors and optical spectrometers were utilized.

2.3.1   Measuring photoluminescence spectra

Photoluminescence (PL) spectra were recorded for each of the samples listed in table 2.1, both in the as-deposited state and following every annealing step, using the setup illustrated in Fig. 2.2. The samples were optically pumped ($\sim$ 20 mW continuous wave excitation power in a beam of $\sim$ 4 mm^2) by the 325 nm line of a helium cadmium (HeCd) laser, a wavelength not resonant with any excited state of Er^{3+} , to excite the silicon nanoclusters in the material. Band-pass filters ensured that all other emission lines (e.g. 442 nm) of the HeCd laser were filtered out and would not contribute to either pump light or collected light. Emitted light from the samples was collected via an optical fiber in alignment with the impinging pump beam spot on the sample. An appropriate long-pass filter (cutoff wavelength $\sim$400 nm) was used to block residual laser light; wavelengths longer than the cutoff are delivered to an optical spectrometer.

An Ocean Optics spectrometer with a fixed grating coupled to a silicon CCD array was used to record spectra in the visible wavelength range. The spectral response of the system was corrected by normalizing to a standard black-body
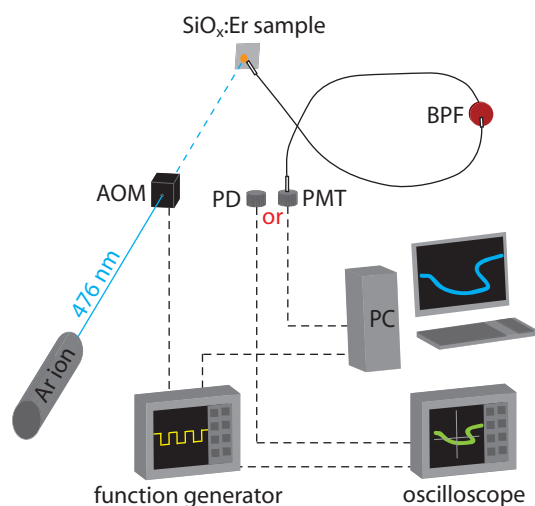
Fig. 2.3: Experimental setup to measure photoluminescence dynamics. The laser light of 476 nm is modulated by an AOM before impinging on the sample. Photoluminescence decay and rise curves from either the Si-NC or the Er^{3+} ions were collected via an optical fiber and recorded by an InGaAs photodiode (NIR) or a PMT (visible).

radiator (3100 K).

In order to record the emission from Er^{3+} ions in the near-infrared (NIR), a liquid nitrogen cooled indium gallium arsenide (InGaAs) CCD array was used. Spectral resolution of the NIR light was achieved within a computer controlled Acton Microspec 2500i spectrometer equipped with multiple gratings. A grating with 300 lines/mm was used to cover the relatively broad emission range of the samples with adequate resolution. Typical collection times were 1 second in the visible and 30 seconds in the near-infrared, respectively, and were kept constant for all measurements to enable comparison of results.

To determine photoluminescence saturation behavior at higher excitation powers, the HeCd laser was replaced by a more powerful argon ion laser emitting at a wavelength of 476 nm. Also, a 550 nm long-pass filter was in this case used to remove all light below this wavelength, especially the laser light reflected from the sample. Photoluminescence was recorded as described above, and the resulting intensities were normalized to an identical integration time.

2.3.2 Luminescence dynamics analysis

Measurement of rise and decay time for photoluminescence originating from both the Si-NCs and the co-doped Er^{3+} ions were performed. A typical setup is shown in Fig. 2.3. To measure the dynamics of light emission, one needs to modulate the pump source (i.e. in this case the laser beam). Modulation was achieved using an acousto-optic modulator (AOM) controlled by a function generator, chopping the 476 nm pump beam from the argon ion laser into a square wave of desired frequency, depending on the duration of the observed luminescence decay. Photo-
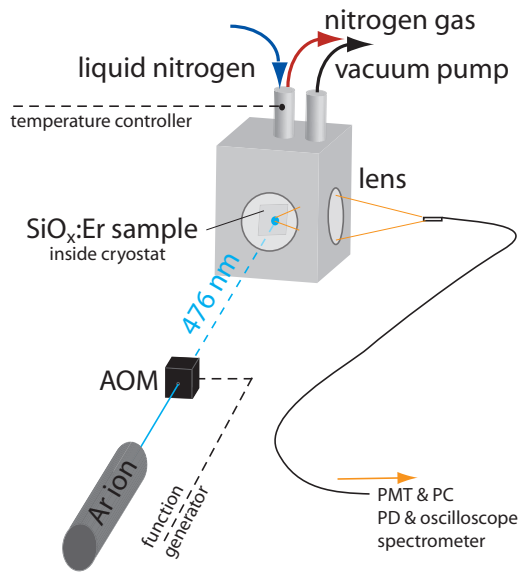
Fig. 2.4: Experimental setup to measure photoluminescence temperature dependence. The sample is placed in a evacuated cryostat chamber and cooled to a minimum of 77 K with liquid nitrogen. An AOM modulates the pump laser beam (476 nm) before it enters the cryostat via a glass window and impinges on the sample inside. Photoluminescence is focused onto the end of a collection fiber outside the cryostat by a plano-convex lens replacing one window facet of the cryostat. The collected emission is detected and analyzed by spectrometers and photodetectors as discussed previously.

luminescence was again collected via an optical fiber and delivered to the detector. Undesired wavelengths (e.g. from the laser) were filtered out by a band-pass filter. Decay and rise times of emission from Si-NCs, either amorphous or crystalline, were recorded by a photomultiplier tube (PMT) triggered by the function generator. No PMT for the near-infrared emission of erbium was available. Instead, a thermoelectrically-cooled InGaAs photodiode was used and the amplified signal was analyzed via a digital storage oscilloscope triggered by the function generator as illustrated in Fig. 2.3. The system response time of this setup was limited by the response time of the AOM and determined to be $\sim$ 20 µs.

2.3.3 Photoluminescence temperature dependence

Investigations of the photoluminescence behavior at different temperatures were carried out by placing the samples on a liquid nitrogen cooled sample holder inside a cryostat chamber as shown in Fig. 2.4. Evacuation of the cryostat to a base pressure of about 2×10^{-6} Torr prevents condensation of water vapor inside the chamber, and minimizes heat transfer by convection. A disadvantage of positioning the specimens inside such a cryostat chamber is that it is no longer possible to place the collection fiber in close proximity to the sample. Instead, one facet of the cryostat chamber was replaced by a plano-convex lens, which focused the photoluminescence from the sample onto a point roughly 20 cm away, where the end of the collection fiber was positioned. Compared to the previous setup with the collection fiber close to the sample ($\sim$ 3-5 mm) a significant fraction of photoluminescence intensity ($\sim$ 75 %) was lost in this setup. Thicker film layers were deposited

to compensate for these losses. Photoluminescence intensity and dynamics were measured from temperatures of 77 K to 300 K.

2.4 Results & Discussion

2.4.1 Stoichiometry and microstructure

Rutherford backscattering spectroscopy (RBS) analysis was carried out for film samples with stoichiometries (as determined by the crystal monitors during deposition) of $SiO_{1.4}$:Er and $SiO_{1.7}$:Er. Results for the latter specimen revealed a stoichiometry of $SiO_{1.98}$:$Er_{0.00353}$ and a film thickness of 1.65 μm . While the determined thickness and Er concentration (0.00353 erbium atoms per 2.98 atoms of silicon and oxygen $\longrightarrow$ 0.12 at.%[‡]) agree reasonably with the values derived from deposition rates during evaporation, a substantial amount of excess oxygen, compared to the estimate from the crystal monitors, is present in the sample according to RBS. Analysis via RBS of the $SiO_{1.4}$:Er sample on the other hand discovered a stoichiometry of $SiO_{1.4}$:$Er_{0.0053}$ and a film thickness of 200 nm. These results match the intended oxygen-to-silicon ratio, erbium concentration (0.0053 erbium atoms per 2.4 atoms of silicon and oxygen $\longrightarrow$ 0.22 at.%), and layer thickness, suggesting that thin films ($\sim$ 200 nm) of SiO_x:Er can be deposited with high accuracy concerning layer composition and thickness with this PVD technique. Considering the costs per sample associated with RBS analysis, additional specimens were not tested.

A lognormal distribution of Si-NC sizes is expected[100,101] and has been observed over a range of annealing temperatures from 400°C to 1100°C .[9] High-resolution transmission electron microscopy (HRTEM) analysis[32] of SiO films (see Fig. 1.3) shows growth of amorphous Si-NCs with a mean diameter of 2-3 nm after annealing at temperatures below 900°C . As the annealing temperature increases, the Si-NC ripen until, after annealing at 1100°C , the now crystallized nanoclusters average $\sim$ 7 nm in diameter.

Transmission electron microscopy (TEM) analysis was also carried out on a heavily Er-doped ($>$ 2 at.%) $SiO_{1.5}$ film annealed at 1100°C in order to investigate both the crystalline Si-NCs and Er-clusters, respectively. A TEM image showing a

---

[‡]It is often of interest to determine the concentration of Er in atoms/cm^3. By assuming that the presence of erbium does not change the atomic number density of the bulk material (valid for low Er concentrations), the number of Er atoms/cm^3 may be found as[9]

$$\frac{N_{Er}}{cm^3} = \frac{N_A \rho_{SiO_x} Er_{atomic}}{\bar{M}_{SiO_x}} \tag{2.3}$$

where N_A is Avogadro's number (6.02×10^{23} mol^{-1}), ρ_{SiO_x} represents the density of the SiO_x film, and $\bar{M}_{SiO_x}$ is the average molar mass of the atoms in the SiO_x . For example, in case of a silicon-monoxide film ($\rho_{SiO} = 2.13$ g/cm^3 and $\bar{M}_{SiO} = 22.04$ g/mol) with an erbium doping concentration of 0.22 at.%, one can calculate the number of Er atoms per cubic centimeter as 1.3×10^{20} atoms/cm^3.
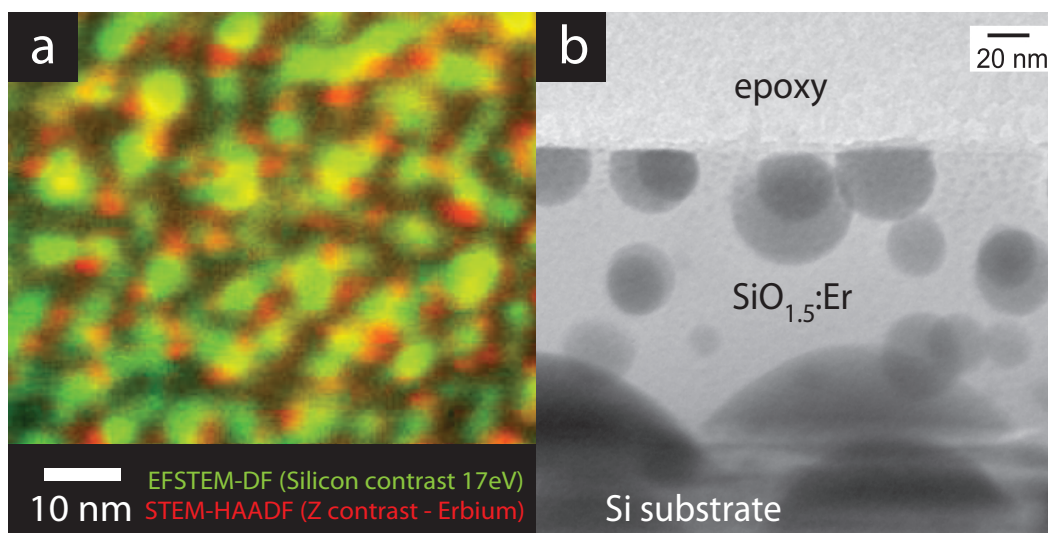
Fig. 2.5: TEM images of $SiO_{1.5}$:Er films. (a) 2D STEM color mixed image showing sizes and locations of Er-clusters (red) and Si-NCs. (green) in a $SiO_{1.5}$:Er (1 at.%) film after annealing at 1000°C . (b) TEM bright field cross-sectional image of a $SiO_{1.5}$:Er (> 2 at.%) film after annealing at 1100°C .

cross-sectional view of the film is shown in Fig. 2.5(b). Dark spheres with diameters ranging between 20 to 30 nm were readily observed. These spheres represent erbium rich regions according to qualitative energy-dispersive X-ray (EDX) spectroscopy. Clusters of even larger dimensions seem to grow inward from the surface of the silicon wafer. Polman *et al.*[96] have observed similar erbium clustering in Er-doped SiO_2 annealed above a temperature of 1000°C , accompanied by sudden quenching of Er^{3+} photoluminescence intensity to nearly zero.

Further investigations of the microstructural properties of an Er-doped ($\sim$ 1 at.%) $SiO_{1.5}$ film annealing at a temperature of 1000°C have been carried out in cooperation with Li *et al.*[102]. In this work, TEM was used to image Si-NCs and Er^{3+} nanoclusters and their respective sizes and locations in 2D and 3D. Briefly, two atomic number contrast images can be obtained by using two detectors in the scanning transmission electron microscopy (STEM) mode. High angle annular dark field (HAADF) STEM images provide atomic number contrast (Z-contrast) and were used to image erbium rich regions; whereas, energy-filtered (EF) imaging centered on the 17 eV plasmon energy loss line of silicon shows the Si-NCs in the SiO_x matrix. Figure 2.5(a) shows a superimposed image combining both imaging modes. Although the sizes and relative positioning in this 2D projection can be easily misinterpreted due to overlap effects, it is apparent that Er^{3+} ions exhibit a tendency to preferentially locate within the SiO_2 matrix rather than inside the Si-NCs.

2.4.2 SiO$_x$:Er refractive index

Refractive indices for a variety of SiO$_x$:Er compositions investigated in this work were determined by means of ellipsometry as described in appendix A. Additionally, the effect of increasing annealing temperature was estimated by measurements of the optical constants before and after annealing the specimens at 500°C and 1000°C . Figs. 2.6 (a) and (b) present a summary of the results.
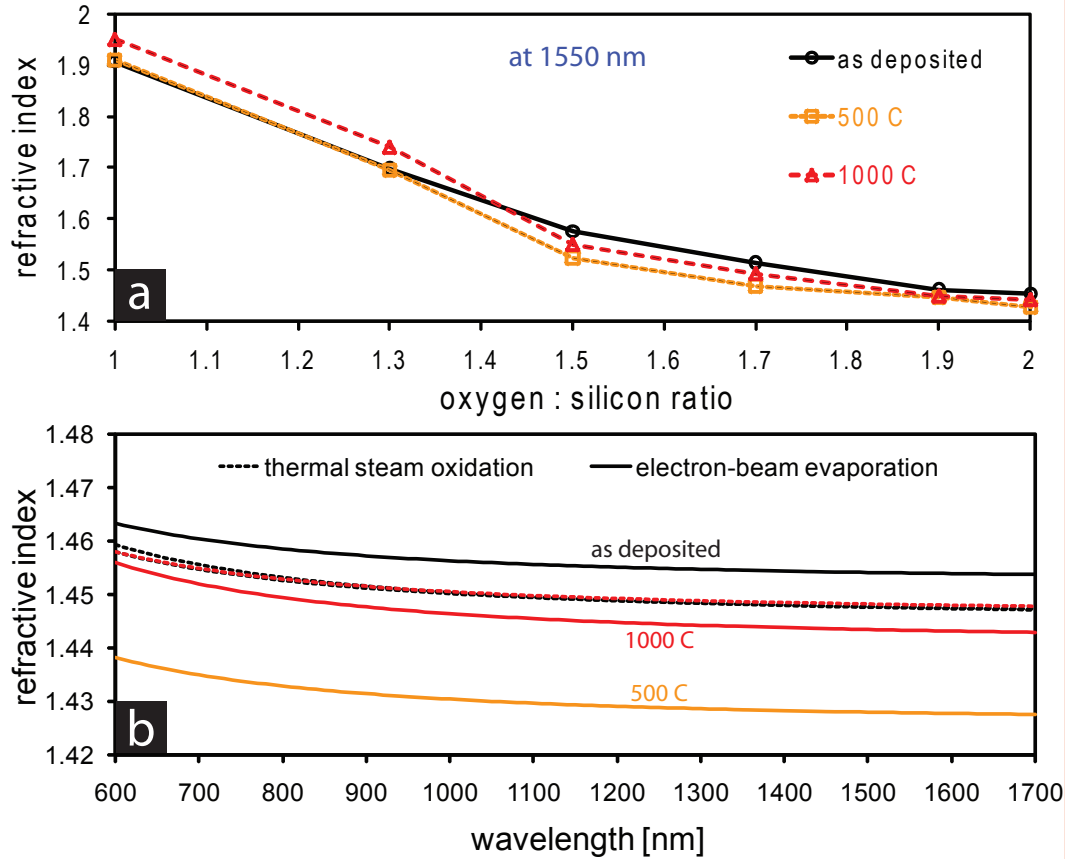
Fig. 2.6: Ellipsometry results for film thickness and refractive indices obtained for various SiO$_x$:Er compositions and annealing temperatures. (a) illustrates the measured refractive indices for various SiO$_x$:Er compositions before (○) and after annealing at 500°C (□) and 1000°C (△). (b) compares the refractive indices obtained for SiO$_2$ films formed by thermal oxidation and electron-beam deposition for the same annealing conditions.

As shown in Fig. 2.6 (a), the refractive index of SiO$_x$ and SiO$_x$:Er materials drops with increasing oxygen concentration and for $\lambda = 1.54$ µm approaches refractive index values around 1.45 (comparable to fused silica) as x (i.e. the oxygen-to-silicon ratio) goes towards 2. Upon annealing the investigated film specimens at 500°C and 1000°C , respectively, a slight change in refractive index can be observed compared to the 'as deposited' samples.

Figure 2.6 (b) compares the refractive indices obtained from a SiO_2 film sample deposited by e-beam evaporation - a potential material for the waveguide upper cladding - with values measured for a SiO_2 film formed via thermal steam oxidation - the undercladding material used in this work - before and after annealing at $500°C$ and $1000°C$. No change in the refractive index due to annealing is observed for the oxidation sample ($n = 1.448$ at 1550 nm). This might be expected since the film is already exposed to a temperature of $1000°C$ for 16 hours during oxidation.

In contrast, the refractive index of SiO_2 deposited by electron-beam is slightly decreased from $n = 1.454$ at $\lambda = 1550$ nm for the unannealed case to $n = 1.428$ after annealing at $500°C$. It then recovers to $n = 1.443$ for $T_{anneal} = 1000°C$, close to the value obtained for the oxidation specimens.

Further ellipsometry measurements were conducted on SiO_2 films deposited via plasma-enhanced chemical vapor deposition (PECVD), since these material can be readily etched into rib structures. In this case the obtained refractive index of $n = 1.465$ was relatively high compared to samples made by e-beam deposition and thermal oxidation.

2.4.3 Photoluminescence

All films deposited and tested in the frame of this work showed excellent long-term optical stability. Photoluminescence measurements were repeatable after extended periods of time (several days). Collection of emission from different spots of the same sample resulted in nearly identical results in the vast majority of cases. The results were also highly repeatable. Annealing films with equal compositions created overlapping photoluminescence spectra and intensities (e.g. from a SiO:Er sample annealed a total of eight times in steps of $100°C$ from $400°C$ to $1100°C$, and a second piece of the same sample only annealed once at $1100°C$). Therefore, repeated testing found that the samples were stable and reproducible.

2.4.3.1 Si-NC photoluminescence spectra, peak wavelength, and intensity

Silicon nanocluster (Si-NC) photoluminescence spectra were obtained for all samples from table 2.1 after each annealing step as described previously and displayed in Fig. 2.7 (for the series not including erbium) and in Fig. 2.8 (for the series deposited with erbium). Both amorphous and crystalline silicon nanocluster emission feature wide inhomogeneously broadened photoluminescence bands. With increasing oxygen-to-silicon ratio, the emission bands peak at shorter wavelengths although all samples were annealed at the same temperatures. This fact is readily understood considering the smaller number of silicon atoms available within a characteristic diffusion volume to form the Si-NCs, resulting in smaller cluster sizes for lower Si concentrations. The peak wavelengths of the nanocluster emission show good agreement with previous results.[32] The peak wavelengths are shown in Fig. 2.9 as a function of oxygen-to-silicon ratio (x) and annealing temperature
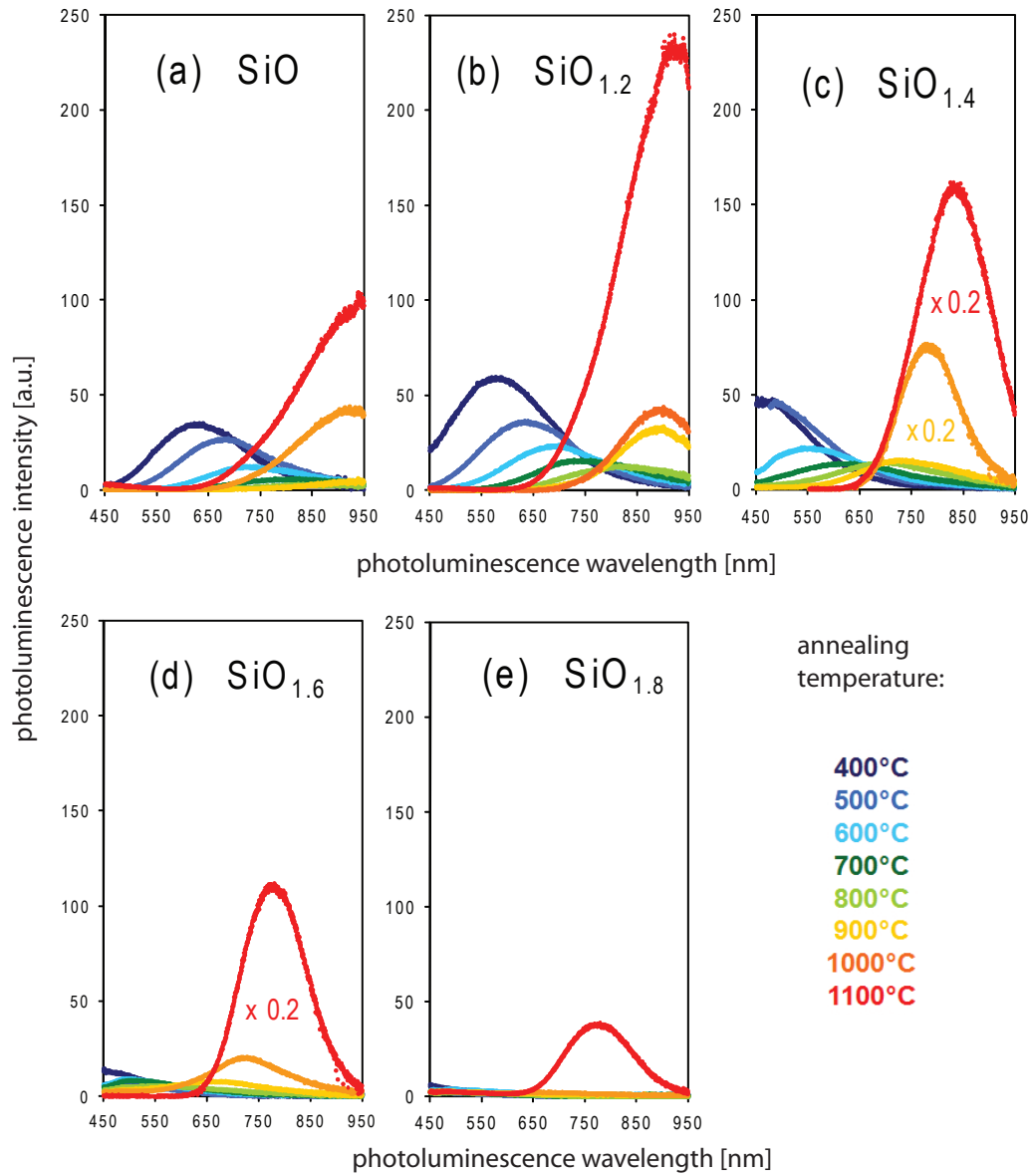
Fig. 2.7: Photoluminescence spectra for all investigated SiO_x materials (without Er) after annealing at temperatures from 400°C to 1100°C .
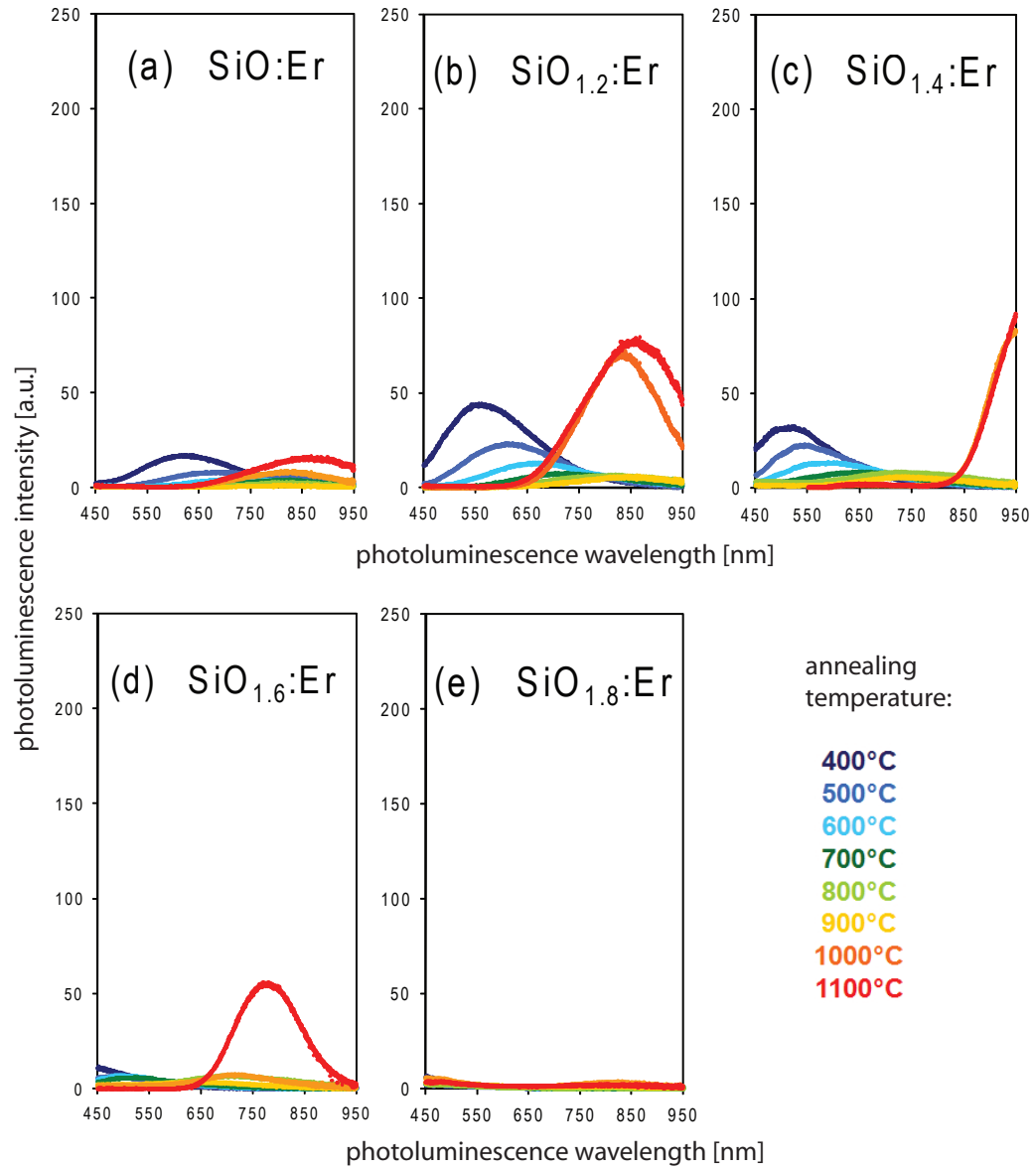
Fig. 2.8: Photoluminescence spectra for all investigated SiO_x:Er materials after annealing at temperatures from 400°C to 1100°C .
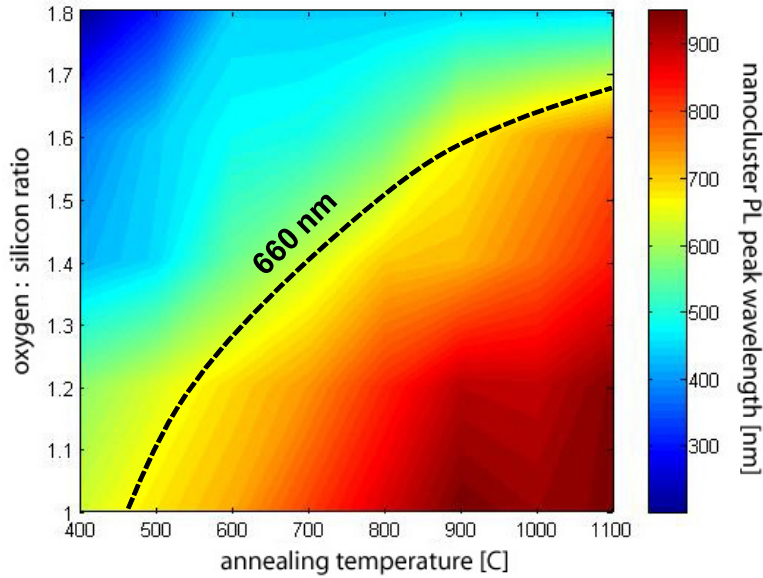
Fig. 2.9: PL peak wavelengths for all SiO_x compositions and annealing temperatures T_{anneal}. The dashed line serves as a guide to the eye approximating the conditions for a peak PL wavelength of 660 nm. The significance of this will be discussed later.

(T_{anneal}). It has been established previously that the PL from amorphous Si-NCs is characteristic of band-tail emission in amorphous Si.[32] Here, we see that the peak of the Si-NC emission is shifted to longer wavelength with increasing annealing temperatures. Since the Si-NCs grow larger with increasing temperature[103,104], the red-shifting of the peak wavelength can be attributed to emission from larger amorphous Si-NCs. This size-dependence of amorphous Si-NC photoluminescence is consistent with the spatial confinement model as introduced previously.[34,49]

At the same time, the integrated PL intensity decreases with increasing annealing temperatures up to the onset of crystallization. At temperatures above about $800-900°C$ the Si-NCs begin to crystallize[32]; PL in this stage is generally attributed to quantum confinement effects[34]. The photoluminescence band of crystalline Si-NCs peaks in the wavelength range 750 - 950 nm depending on nanocrystal size, while the intensity recovers due to the removal of non-radiative centers present in amorphous Si.[32] Strongest Si-NC emission is observed after annealing at $1100°C$ for all samples (see Fig. 2.7 and Fig. 2.8).

A summary of the observed peak wavelengths in the PL spectra is given in Fig. 2.9 as a function of annealing temperature and the oxygen-to-silicon ratio of each sample. The emission peak "red-shifts" to longer wavelength with increasing annealing temperature and with increasing concentration of excess Si (i.e. decreasing oxygen-to-silicon ratio), as the NCs grow larger under these conditions.

2.4.3.2 Si-NC photoluminescence dynamics

Figure 2.10 shows the photoluminescence decay (a) and rise (b) traces obtained via time-resolved measurements at room temperature for a $SiO_{1.5}$ film annealed at
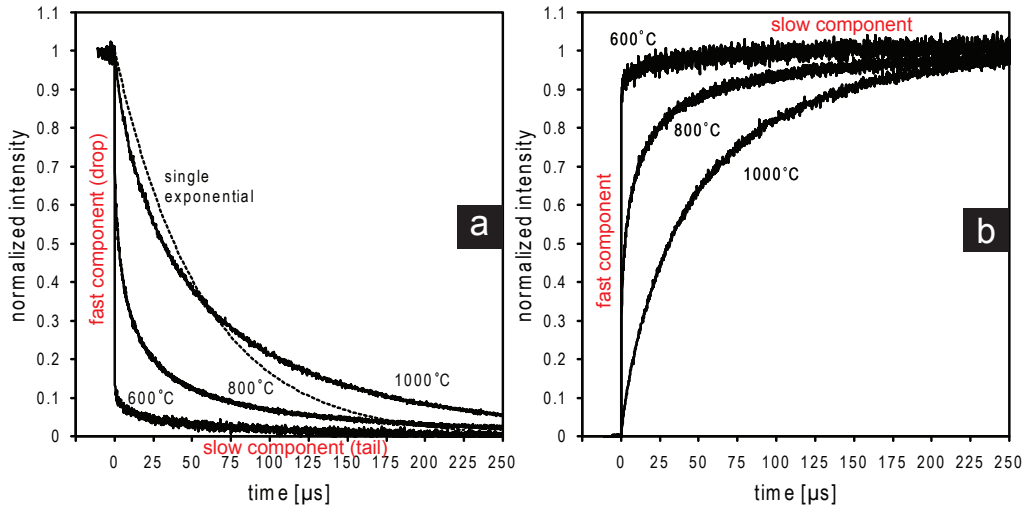
Fig. 2.10: Photoluminescence decay (a) and rise (b) curves for a $SiO_{1.5}$ film annealed at 600°C , 800°C , and 1000°C collected at room-temperature. A single-exponential with the same decay rate as the $c-$Si-NCs PL (1000°C) was added as a dashed line to illustrate the stretched character of the decay trace. Time zero corresponds to either the end (a) or the onset (b) of the pulsed excitation beam.

temperatures of $T_{anneal} = 600$°C , 800°C , and 1000°C in forming gas. For an annealing temperature of 600°C , the Si-NCs are amorphous (*a*-Si-NCs), whereas for $T_{anneal} = 1000$°C , the photoluminescence originates from crystalline nanoclusters (*c*-Si-NCs). Annealing at $T_{anneal} = 800$°C covered the intermediate region in an attempt to investigate the change in the PL dynamics close to the amorphous-to-crystalline transition.

The time-resolved data in Fig. 2.10 (a), collected upon termination of the pump light, shows that the photoluminescence dynamics of *a*-Si-NCs are strongly non-exponential. Although less obvious to the eye, decay curves of *c*-Si-NCs are also not well-described by a single exponential, which is illustrated by adding a single exponential with the same 1/e photoluminescence decay time to Fig. 2.10 (a). Decay traces from *a*-Si-NCs are generally characterized by a dominant fast component (< 0.1 μs) and a slow component or "tail" as shown in Fig. 2.10. These 'fast' and 'slow' components of the photoluminescence decay have been observed for porous silicon[105], crystalline Si-NCs[106,107], and amorphous silicon nanoparticles[108], indicating that multiple recombination mechanisms are possible in these materials. No fast-decay component (< 0.1 μs) was evidenced in the present work for annealing temperatures of 800°C and 1000°C .

The PL dynamics collected upon turning the pump light on – i.e. the PL intensity 'rise' – show the same characteristics (see Fig. 2.10 b) that where observed for the PL decay. At $T_{anneal} = 600$°C the rise trace clearly shows a fast and a slow component, whereas for annealing temperatures of 800°C and 1000°C the 1/e rise

time was longer and no clear distinction between a fast and a slow component is possible.

The slow decay and rise component in the micro-second time regime is described well by a stretched exponential function given by[105,108]

$$I_{\text{decay}}(t) = I_0 \times \exp^{-\left(t/\tau_{\text{decay}}\right)^\beta}, \text{ and} \qquad (2.4)$$

$$I_{\text{rise}}(t) = I_0 \times \left[1 - \exp^{-\left(t/\tau_{\text{rise}}\right)^\beta}\right], \qquad (2.5)$$

where $0 < \beta < 1$ is a parameter determining the "degree of stretching" and τ_{decay} and τ_{rise} are the characteristic "effective" lifetimes of the decay and rise processes. This 'stretching' of the PL decay and rise is caused by a wide distribution of excitation and recombination rates, which may originate from different forms of disorder[105], such as a wide distribution of Si-NC sizes, a random spatial arrangement of the Si-NCs, and localized states at the Si-NC surfaces.[106,107]

The curve fitting toolbox in MATLAB was used to fit the experimentally measured decay and rise data from Fig. 2.10 for a $SiO_{1.5}$ film annealed at 600°C , 800°C, and 1000°C to stretched exponential functions and thus to determine β and τ values. The resulting fitting parameters are presented in table 2.3. The lifetimes and

Annealing temperature T_{anneal} (°C)	Decay time τ_{decay} (µs)	Rise time τ_{rise} (µs)	Stretching factor β
600 (tail)	85.0	77.6	0.71
800	7.2	6.7	0.37
1000	51.2	49.7	0.70

Table 2.3: Room-temperature Si-NC PL decay and rise times for a $SiO_{1.5}$ film annealed at 600°C , 800°C , and 1000°C .

stretching factors obtained for annealing temperatures of 600°C and 1000°C are in good agreement with values reported elsewhere ($\beta \approx 0.76$[109] and $\tau \approx 50$ µs[106]). However, for $T_{\text{anneal}} = 800$°C the values of $\beta = 0.37$ and $\tau \approx 7$ µs resulting from a fit with one stretched-exponential function were quite different from the expected parameters, despite small residual values ($R^2 > 0.99$). Based on the observation of different recombination mechanisms and fast and slow decay components as mentioned previously, the decay at $T_{\text{anneal}} = 800$°C was also fit with two different decay components (i.e. stretched-exponential functions). To limit the range of free parameters, τ and β of one (slow) component were matched with the values obtained for the other annealing temperatures. Table 2.4 presents the results obtained from this 'alternative' fit including the determined ratio between the intensities (at time zero) of both components.

The decay lifetime determined for the second component in this fit was $\tau_{\text{decay}} = 4.1$ µs (see table 2.4). Interestingly, the steady-state intensity ratio ($t = 0$) between 'fast' and 'slow' component (9:1) was very similar to the ratio observed for T_{anneal}

Annealing temperature T_{anneal} (°C)	Component	Intensity (normalized)	Decay time τ_{decay} (µs)	Stretching factor β
800	slow	~0.1	50 (fixed)	0.71 (fixed)
	fast	~0.9	4.1	0.34

Table 2.4: τ and β values for fitting SiO$_{1.5}$ ($T_{\text{anneal}} = 800°$C) with two stretched-exponential functions.

= 600°C (see Fig. 2.10). Time-resolved spectroscopy might enable the identification of two or more distinct (in life time and energy/wavelength) decay processes and further explain the PL dynamics observed in this work.

From the photoluminescence analysis provided in this section one can conclude that different recombination and excitation mechanisms exist within the Si-NC material system. A fast and a slow component of the PL dynamics can be evidenced in a-Si-NCs, whereas a single (slow) process is dominant in the crystalline case.

2.4.3.3 Si-NC absorption cross section

By approximating silicon nanoclusters as two level systems (which is approximately true if Si-NCs excited to a higher level quickly decay non-radiatively to the lowest energy state in the 'band-tail' or sub-gap state of the conduction band)[22,35,59], it is possible to estimate an absorption cross-section for the Si-NCs via the relation[110] $1/\tau_{\text{rise}} = R_{\text{abs}} + 1/\tau_{\text{decay}}$. Here, R_{abs} represents the absorption rate given by $\sigma_{\text{abs}} \times \phi_{\text{pump}}$, where σ_{abs} is the absorption cross-section, and ϕ_{pump} is the incident photon flux. Therefore,

$$\sigma_{\text{abs}} = \left(\frac{1}{\tau_{\text{rise}}} - \frac{1}{\tau_{\text{decay}}} \right) / \phi_{\text{pump}} \qquad (2.6)$$

Table 2.5 shows the calculated absorption rates and cross-section for the SiO$_{1.5}$ films investigated above ($T_{\text{anneal}} = 600°$C , 800°C , and 1000°C) at a photon flux of 1.2×10^{17} cm^{-2}s^{-1}. The obtained values range from about 10^{-15} to about 10^{-14}.

Annealing temperature T_{anneal} (°C)	Decay time τ_{decay} (µs)	Rise time τ_{rise} (µs)	Absorption rate R_{abs} (1/s)	Absorption cross-section σ_{abs} ($\times 10^{-14}$ cm^2)
600 (tail)	85.0	77.6	1122	0.93
800	7.5	6.8	13725	11.44
1000	56.1	49.8	2255	1.88

Table 2.5: Si-NC absorption rate and cross sections calculated for a SiO$_{1.5}$ film annealed at 600°C , 800°C , and 1000°C .

2.4.3.4 Effect of Er-doping on Si-NC photoluminescence

Considering both Er-doped and undoped specimens were deposited in the same
evaporation process and annealed together at the same temperature, it should be
intuitive films of equal composition are essentially the same in terms of Si-NC size
distribution, density, and microstructure, the only difference being of course the
presence of Er dopants in one sample. In the Er-doped samples an alternative de-
excitation pathway besides radiative recombination is now available for excited
Si-NCs, the transfer of energy to Er^{3+} ions. This sensitization action is extremely
well known and has been widely investigated, although its exact nature is still
under debate. A comparison between photoluminescence spectra of both species
can therefore be an important tool to investigate the nature of the energy trans-
fer mechanism. Reduction of a Si-NC emission band, so-called "quenching", was
readily observed for all sample compositions and for all annealing temperatures.
Photoluminescence from crystalline Si-NC was strongly quenched (for example by
a factor of about 10 in $SiO_{1.6}$:Er annealed at 1100°C), whereas quenching in the
amorphous nanocluster case was relatively small (compare for example $SiO_{1.2}$:Er
was quenched by only a factor of about 2 after annealing at 400°C). In some cases
the peak emission wavelength of the SiO_x:Er spectra seemed to be shifted with
respect to the SiO_x spectra, which will be explained further below.
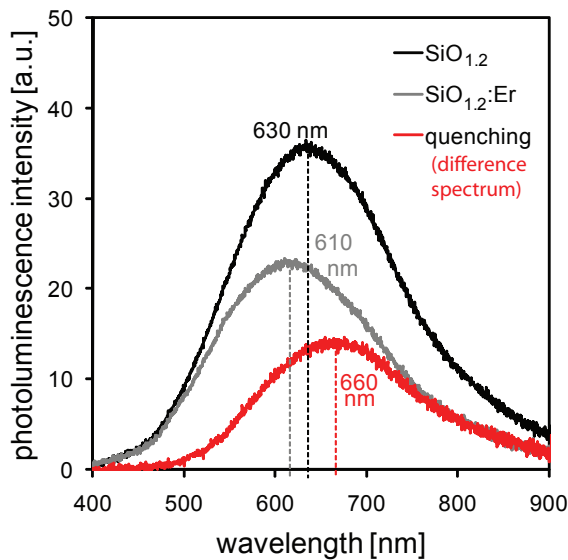
Fig. 2.11: Partially selective quenching of Si-NC photoluminescence upon introduction of erbium into SiO_x . Comparison between the PL spectra from $SiO_{1.2}$ and $SiO_{1.2}$:Er ($T_{anneal} = 500°C$) and the quenched photoluminescence difference spectrum, which is centered at a wavelength of 660 nm.

Here, the photoluminescence was not quenched equally over the entire width
of the PL band, but rather more selectively, favoring distinct wavelengths. One ex-
ample for such a inhomogeneous quenching effect is shown in Fig. 2.11, presenting
photoluminescence spectra of both Er-doped and undoped films with $x = 1.2$ af-
ter annealing at $T_{anneal} = 500°C$. The emission band of the $SiO_{1.2}$ film sample was
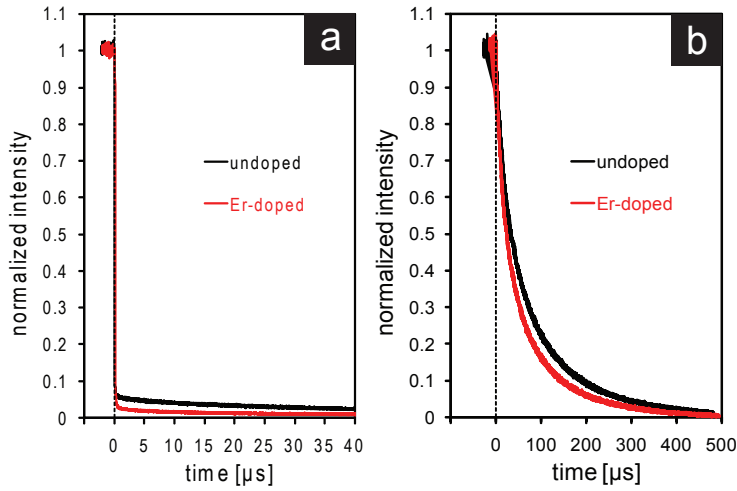
Fig. 2.12: Impact of Er-doping on the Si-NC PL intensity decay lifetime. Decay curves for Er-doped and undoped films containing amorphous (a) and crystalline (b) silicon nanoclusters are shown.

slightly more intense and peaked at a wavelength of 635 nm, whereas the photoluminescence of the $SiO_{1.2}$:Er film sample was weaker and centered at around 615 nm. Also depicted in Fig. 2.11 is the difference in intensity ($I_{undoped}$ minus $I_{Er-doped}$) between both spectra, showing selective quenching of the PL for a wavelength of about 660 nm. Comparison of the doped and undoped samples for all compositions and annealing temperatures yielded a trend towards a number of quenching "hotspots" for many specimens. These wavelengths for preferred intensity quenching were located near 540 nm, 660 nm, and 800 nm. These wavelengths are in close correspondence with the energies of the $^4S_{3/2}$, $^4F_{9/2}$, and $^4I_{9/2}$ excited states of Er^{3+} ions.

A comparison of the Si-NC decay times of both Er-doped (red) and undoped (black) SiO samples recorded at 77 K is shown in Fig. 2.12 (a) and (b) for amorphous ($T_{anneal} = 500°C$) and crystalline ($T_{anneal} = 1000°C$) nanoclusters, respectively. The Er-doped samples showed a faster decay for the Si-NC photoluminescence compared to the undoped specimens for both annealing temperatures. In case of the crystalline Si-NCs, the $1/e$ decay time of 52.3 μs shortened to 35.9 μs when Er^{3+} ions were present. Contrary to this finding, Kik *et al.*[59] have reported no change in the photoluminescence decay of *c*-Si-NC for increasing doping concentrations of erbium. The authors therefore proposed a "strong coupling model", where only the nanocrystals isolated from any Er^{3+} ion contribute to the photoluminescence at all. The shortening in Si-NC decay times with Er-doping observed in this work rather suggest a different model, where Si-NCs 'coupled' to Er^{3+} ions can either recombine by emitting a photon or by transferring energy to an Er^{3+} ion. In this case, the decay time of Si-NC photoluminescence depends on the Er^{3+} concentration.
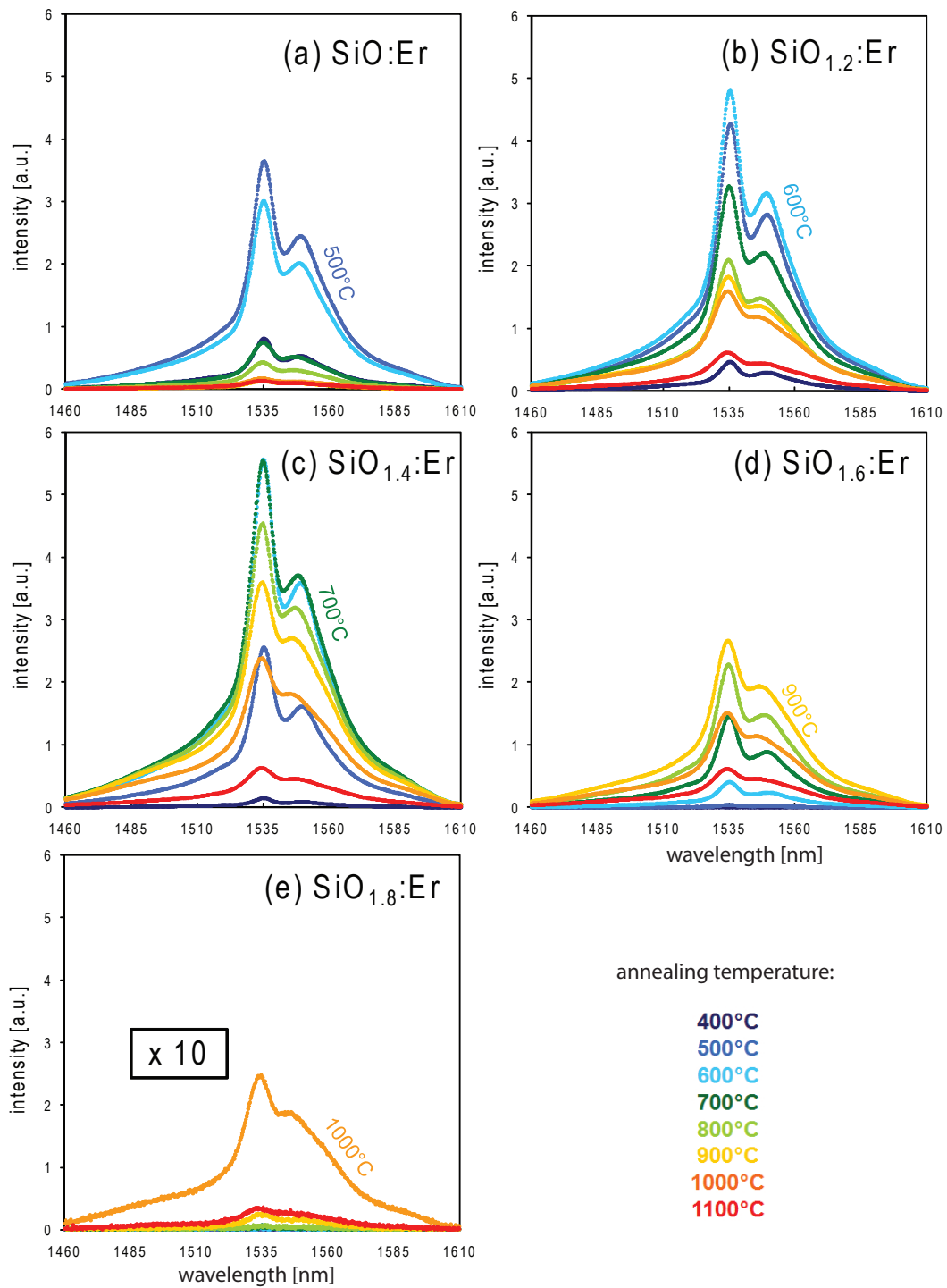
Fig. 2.13: Er^{3+} spectra for various compositions and annealing temperatures.

2.4.3.5 Er^{3+} photoluminescence spectra and intensity

The Er-doped films listed in table 2.1 exhibit two additional photoluminescence bands at wavelengths of 0.98 μm and 1.54 μm due to the Er^{3+} ions embedded in the material and the corresponding radiative transitions from the second excited state ^{4}I$_{11/2}$ and the first excited state ^{4}I$_{13/2}$ to the ground state ^{4}I$_{15/2}$. The ^{4}I$_{11/2}$ →^{4}I$_{15/2}$ transition is rather weak, indicating that non-radiative relaxation to the first excited level dominates over the radiative process to the ground state. Photoluminescence spectra of the ^{4}I$_{13/2}$ →^{4}I$_{15/2}$ transition (1.54 μm) obtained from the Er-doped samples for annealing temperatures of 400°C to 1100°C were recorded using a excitation wavelength of 325 nm (i.e. does not coincide with any of the optical absorption bands of Er^{3+}) and a pump photon flux of about $1 \times 10^{18}$ cm^{-2}s^{-1} and are shown in Fig. 2.13 (a)-(e). The spectra consist of two distinct peaks at around 1535 nm and around 1550 nm typical for Er^{3+} ions embedded in a silica fiber, suggesting that the optically active and emitting Er^{3+} ions are embedded in the SiO$_2$ host matrix surrounding the Si-NC and not within the clusters themselves.[68] This is in agreement with the STEM results presented earlier. The position of this emission peak does not change for different excess silicon concentrations or annealing temperatures. Erbium photoluminescence *intensities* on the other hand strongly depend on annealing temperature and oxygen-to-silicon ratio. The highest intensity was obtained for the SiO$_{1.4}$:Er film annealed at 700°C as shown in Fig. 2.13 (c). It is interesting to note that strongest emission intensities were obtained for different annealing temperatures depending on SiO$_x$ compositions. In particular, PL intensity at 1.54 μm peaked for SiO:Er at $T_{\mathrm{anneal}} = 500$°C , for SiO$_{1.2}$:Er at $T_{\mathrm{anneal}} = 600$°C, for SiO$_{1.4}$:Er at $T_{\mathrm{anneal}} = 700$°C , for SiO$_{1.6}$:Er at $T_{\mathrm{anneal}} = 900$°C , and for SiO$_{1.8}$:Er at $T_{\mathrm{anneal}} = 1000$°C . Figure 2.14 maps the integrated photoluminescence intensities of the measured spectra in terms of the investigated SiO$_x$:Er compositions ($x = 1$ to $x = 1.8$) and annealing temperatures ($T_{\mathrm{anneal}} = 400$°C to 1100°C). Five different zones or regimes may be distinguished in Fig. 2.14:

Zone ① indicates a regime of intense Er^{3+} photoluminescence. The integrated intensity at 1.54 μm peaks for annealing temperatures between about 450°C and 1000°C and stoichiometries in the range of SiO$_{1.2}$ to SiO$_{1.5}$, as indicated by the dashed lines enclosing this regime. Strongest emission is achieved for the SiO$_{1.4}$ film sample annealed between 600°C and 800°C , implying that these values provide optimum conditions for energy transfer from the Si-NCs to the Er^{3+} ions.

Zone ② shows only weak Er^{3+} photoluminescence. There are two possible factors contributing to low 1.54 μm emission at annealing temperatures below ~450°C . The annealing temperature was insufficient to (a) promote growth of sufficiently large Si-NCs, and (b), to encourage optical activation of the Er^{3+} ions, thereby suppressing an efficient sensitization process.
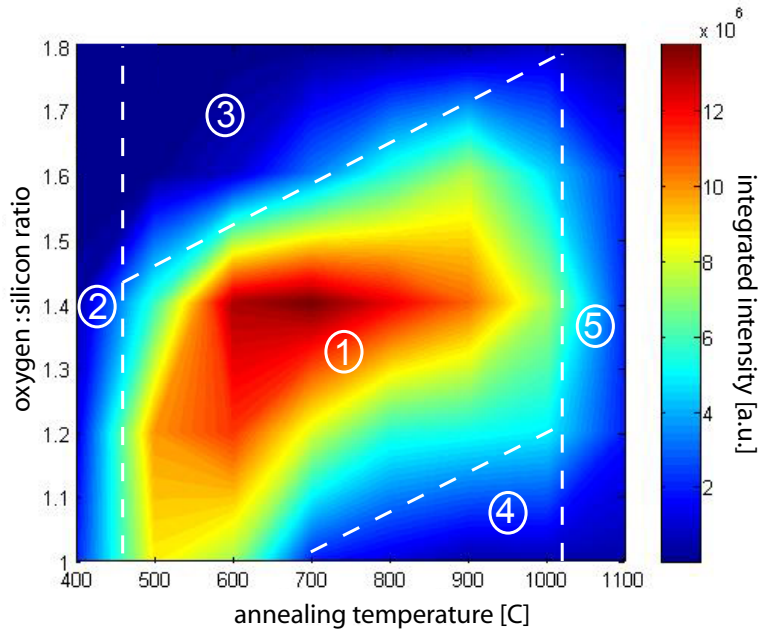
Fig. 2.14: 3D map of Er^{3+} photoluminescence intensity at 1.54 μm .

Zone ③ is also characterized by weak Er^{3+} photoluminescence. As indicated by the results from zone ① and reported in work by Bian *et al.* [90], Er^{3+} ions will be optically active and most efficient in this temperature range. One can therefore conclude that the weak Er^{3+} PL intensity is due to inefficient sensitization from the Si-NCs, resulting from the fact that the reduced amount of excess silicon in this region results in the creation of fewer and wider spread Si-NCs.

Zone ④ shows weak Er^{3+} photoluminescence as well. For high concentrations of excess Si the erbium PL intensity starts to drop rapidly for annealing temperatures above 650°C -700°C . As in zone ③ this seems to be caused by the increasing size of the Si-NCs, as they grow larger with increasing temperature.

Zone ⑤ **weak Er^{3+} photoluminescence:** T_{anneal} in excess of 1000°C on the other hand have been shown [96] to induce clustering of Er^{3+} , thereby reducing the number of optically active ions and quenching photoluminescence, even though energy transfer from the Si-NCs may still be effective.

Several different material characteristics (e.g. Si-NC size and concentration of optically active erbium ions) determine the efficiency of sensitization and 1.54 μm photoluminescence in the Si-NC-coupled Er^{3+} system. Controlling film composition and annealing temperature offers the possibility to influence a variety of material properties in order to optimize Er^{3+} photoluminescence.
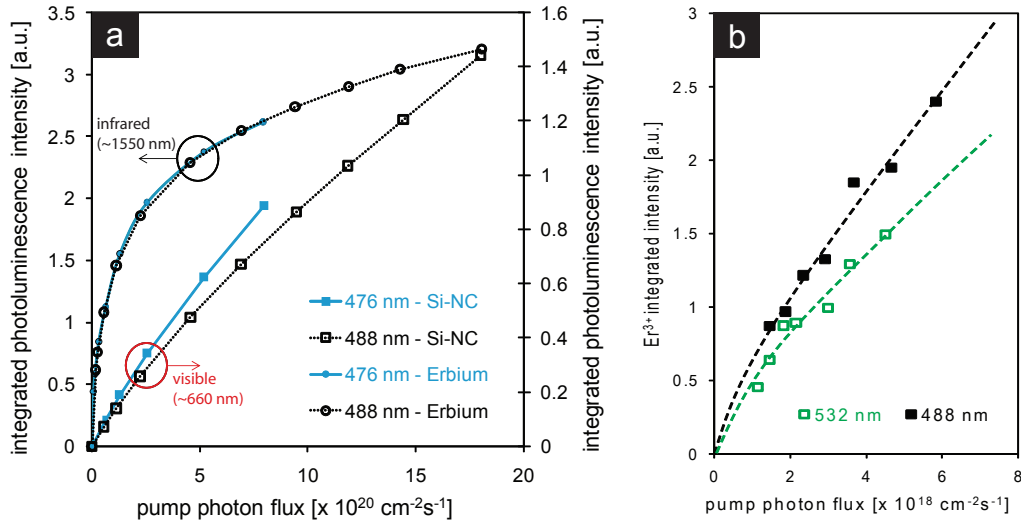
Fig. 2.15: Saturation behavior of Si-NC and Er^{3+} photoluminescence for a $SiO_{1.6}$:Er film excited at 476 nm, 488 nm, and 532 nm. (a) shows integrated intensities for Si-NCs and Er^{3+} ions for increasing pump flux. (b) illustrates integrated Er^{3+} PL intensities for resonant ($\lambda = 488$ nm) and non-resonant ($\lambda = 532$ nm) pumping for low photon flux. Dashed lines are a guide to the eye and present nearly linear behavior at these low pump powers.

The saturation behavior of the integrated photoluminescence intensity was investigated for the $SiO_{1.6}$:Er film sample annealed at $T_{anneal} = 900°C$ in order to determine whether all optically active Er^{3+} ions excitable by resonant pumping ($\lambda = 488$ nm can also be excited non-resonantly ($\lambda = 476$ or 532 nm) via energy transfer from the Si-NCs. The results may also indicate whether the energy transfer is limited by the number of excited Si-NCs or the amount of optically active Er^{3+} ions.

PL spectra were recorded and integrated over for both the Si-NC PL in the visible range (~650 nm) and Er^{3+} emission at 1.54 µm for increasing pump photon flux as shown in Figs. 2.15 (a) and (b). Excitation photon flux was calculated from pump power and laser beam spot area as described in detail in appendix B. The pump wavelength of 488 nm is resonant with the ${}^4F_{7/2}$ erbium level. Er^{3+} ions may therefore be excited by direct absorption of a photon in addition to excitation through energy transfer from Si-NCs. For pump wavelengths of 476 nm and 532 nm on the other hand (non-resonant with any Er^{3+} level), the Er^{3+} ions can be excited by sensitization from the Si-NCs alone.

It can be seen in Fig.2.15(a) that the integrated Er^{3+} PL intensity clearly flattened towards a saturation level at a pump photon flux of 2×10^{21} cm^{-2}s^{-1} (or ~ 800 Wcm^{-2}). Both, resonant and non-resonant pumping (476 nm and 488 nm) resulted in identical 1.54 µm PL intensities, suggesting that all optically active Er^{3+} ions in the excitation volume can be pumped by sensitization through silicon nanoclusters. These results are in good agreement with those reported by Kenyon *et al.*[29] for
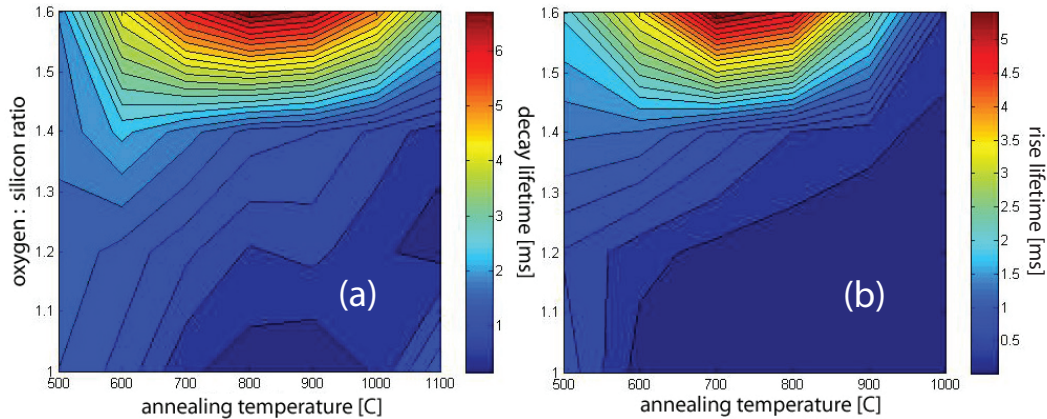
Fig. 2.16: Maps of the radiative decay (a) and rise (b) lifetimes for the $^4I_{13/2} \rightarrow ^4I_{15/2}$ transition of Er^{3+} ions in SiO_x:Er films ($x = 1 - 1.6$) annealed from $400 - 1100°C$.

similar SiO_x:Er samples.

Fig. 2.15(b) shows the integrated PL intensity at 1.54 µm for a non-resonant pump wavelength of 532 nm, in comparison to the partially direct excitation with 488 nm pump light. Here, the integrated Er^{3+} intensity decreased to about 80% of its value at low pump intensities, as compared to the resonant case. This might be due to the reduced number of excited Si-NC sensitizers at this wavelength. Saturation behavior could not be observed for pumping with 532 nm light due to the low pump photon flux available.

Contrary to the Er^{3+} PL intensity, the integrated Si-NC PL intensity increased nearly linearly up to the highest pump intensities investigated, the increase being slightly steeper for a pump wavelength of 476 nm than for 488 nm, possibly due to the higher photon energy. One can therefore conclude that the photoluminescence intensity is predominantly limited by the number of optically active Er^{3+} ions in the sample.

2.4.3.6 Er^{3+} photoluminescence dynamics

Er^{3+} photoluminescence decay and rise times of the optical transition from the $^4I_{13/2}$ level to the $^4I_{15/2}$ level under non-resonant excitation ($\lambda = 476$ nm) were determined for all Er-doped samples listed in table 2.1 after annealing at temperatures ranging from 400°C to 1100°C . The decay and rise traces of the Er^{3+} PL can be best fit (i.e. with minimum derivation – $R^2 \sim 1$)to stretched-exponential functions as shown in equations 3.2 and 3.3, as is the case for Si-NCs. The obtained PL decay times ranged from 0.5 to 6.6 ms as presented in Fig. 2.16(a), whereas PL rise times ranged from 0.1 to 5.4 ms as shown in Fig. 2.16(b).

The longest lifetimes were observed for samples rich in oxygen and annealed at temperatures between 700°C and 900°C . Under these conditions a larger number of oxygen atoms is available, enabling the rearrangement of the local environment

to form Er^{3+} sites in a sixfold O coordinated cage, providing a non-centrosymmetric environment that allows strong Er^{3+} photoluminescence.[90] A photoluminescence decay time of τ_{decay}=8.8 ms was determined for the $SiO_{1.7}$:Er film deposited in this work, approaching the lifetimes of 11 - 14 ms typically observed in Er-doped silica fibers.[96,111] Values for Si-NC sensitized Er^{3+} decay times reported previously in the literature range from 1 ms to about 8 ms[28,62,85], but contrary to this work, the Si-NCs were always crystalline ($T_{\text{anneal}} > 1000°C$). The corresponding stretching factor was $\beta = 0.92$, close to the "unstretched" single exponential case ($\beta = 1$), indicating a narrow distribution of lifetimes, corresponding to a similar local environment for all Er^{3+} ions. The rise time obtained for the same sample was τ_{rise}=5.9 ms ($\beta = 0.8$).

Values for an effective excitation cross-section for Er^{3+} ions may be obtained by considering the extracted photoluminescence decay and rise times at 1.54 µm. By assuming that an Er^{3+} ion excited to any of the higher energy levels will non-radiatively decay to the $^4I_{13/2}$ excited state much faster than recombining radiatively to the ground state, one can approximate the Er^{3+} as a simple two-level system. In this case, as for the Si-NC lifetimes, the $1/e$ decay time (τ_{decay}) and rise times (τ_{rise}) are related to the excitation rate by the expression[110]

$$R_{\text{exc}} = \frac{1}{\tau_{\text{rise}}} - \frac{1}{\tau_{\text{decay}}}. \tag{2.7}$$

From the obtained excitation rate, one can determine an effective Er^{3+} excitation cross-section (incorporating absorption of photons by the Si-NCs and energy transfer from the nanoclusters to the Er^{3+} ions) via $R = \sigma_{\text{eff}} \times \phi$. Excitation rates and effective excitation cross-sections were determined for a excitation photon flux of about 2×10^{18} cm^{-2}s^{-1} and listed in table 2.6 for various SiO_x:Er compositions after annealing at a temperature that results in the most intense emission at 1.54 µm for each stoichiometry.

Stoichiometry-T_{anneal}	Decay time τ_{decay} (ms)	Rise time τ_{rise} (ms)	Excitation rate R_{exc} (1/s)	Effective exc. cross-section σ_{eff} ($\times 10^{-16}$cm^2)
SiO-500°C	1.46	0.8	565	2.8
$SiO_{1.2} - 600°C$	1.36	0.3	2598	13.0
$SiO_{1.4} - 700°C$	1.85	0.8	709	3.5
$SiO_{1.6} - 900°C$	6.62	2.25	293	1.5
$SiO_{1.7} - 900°C$	8.8	5.9	56	0.3

Table 2.6: Er^{3+} photoluminescence decay and rise times, excitation rates, and excitation cross sections for various SiO_x:Er films.

Kenyon *et al.*[29] reported the cross sections for direct optical absorption by Er^{3+} ions in SiO_2 as 1×10^{-21} cm^2 and 8×10^{-21} cm^2 at 476 nm and 488 nm, respectively. The effective cross-sections obtained above therefore constitute an increase of 4-5
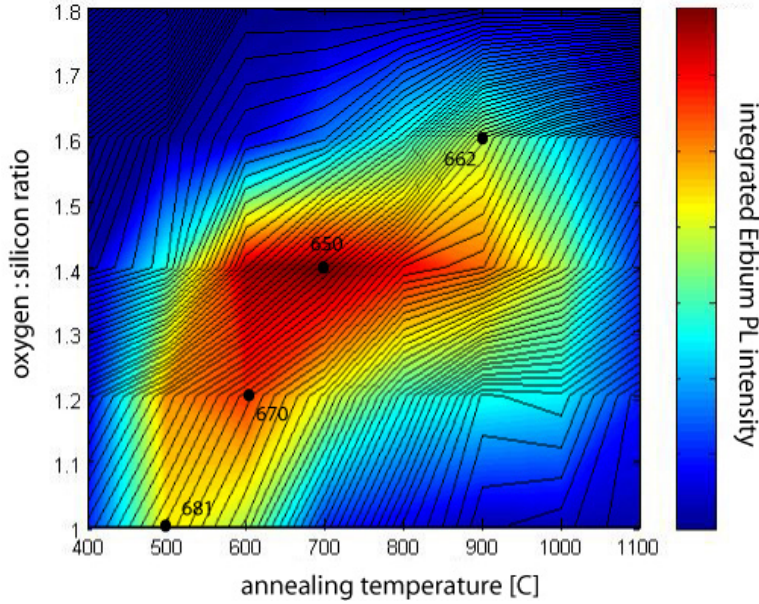
Fig. 2.17: Er^{3+} PL intensity map for all investigated SiO$_x$:Er compositions and T_{anneal} values (color contour). The superimposed black contour lines represent the Si-NC PL peak wavelengths for all specimens as a function of T_{anneal} and the O:Si ratio. The numbers beside the black dots represent the PL peak wavelength, in nm, for the corresponding contour line.

orders of magnitude compared to direct excitation of Er^{3+} ions, and are in good agreement with values reported for c-Si-NC sensitized Er^{3+} by Franzo *et al.*[55], Han *et al.*[85], and Kenyon *et al.*[29] ($2 - 7 \times 10^{-17}$ cm^2).

Faster decay and rise times (τ_{rise}) were obtained for films annealed above 1000°C (i.e. containing crystalline Si-NCs), in turn resulting in much higher estimated effective excitation cross sections. However, Er^{3+} photoluminescence intensities are much lower in this case than for film samples annealed at lower temperatures, likely due to erbium clustering and associated reduced number of optically active ions, as well as ion-ion interactions.

2.4.3.7 Si-NC to Er^{3+} sensitization efficiency

Er^{3+} photoluminescence spectra were recorded for all SiO$_x$:Er specimens after annealing at temperatures ranging from 400°C to 1100°C , and the integrated PL intensities were mapped as a function of x and T_{anneal} in Fig. 2.14. These results show, that the Er^{3+} emission intensity depends strongly on the composition (O:Si ratio) of the film and the annealing temperature.

As discussed in section 1.2, the bandgap energy and photoluminescence wavelength of silicon nanoclusters is - due to spatial confinement effects - size-dependent and therefore also depends on the stoichiometry of the film and the applied annealing temperature (see Fig. 2.9). A comparison of the Si-NC emission wavelength with the integrated Er^{3+} PL intensity obtained for the same film x and T_{anneal} can be used in order to identify conditions for efficient sensitization and serves as a qualitative indicator for the efficiency of the energy transfer from Si-NCs to Er^{3+}
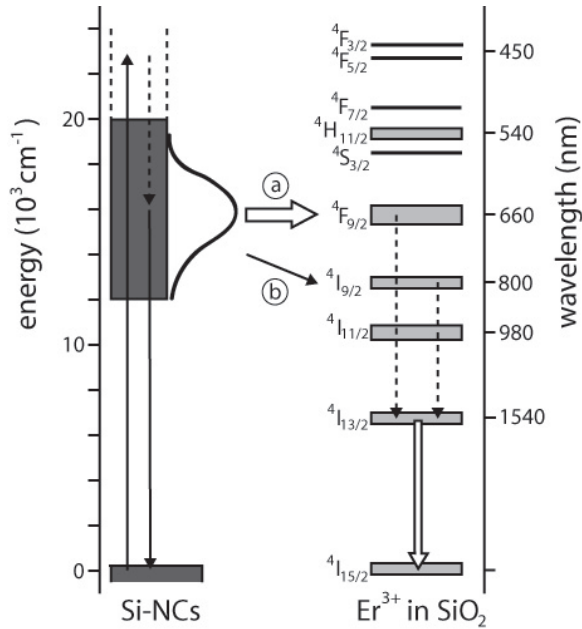
Fig. 2.18: Schematic representation of excitation, energy transfer, and recombination processes within the Si-NC and Er^{3+} system. Arrow (a) indicates a resonant energy transfer, whereas arrow (b) presents the possibility for a phonon-assisted process.

ions. This is because excitation of the luminescent Er^{3+} ions occurs indirect through the energy transfer from excited Si-NCs only. For this purpose, Fig. 2.14 was superimposed with Fig.2.9 (solid lines - points along any solid line correspond to equal photoluminescence wavelengths; adjacent lines differ in wavelength by about 7.5 nm) as presented in Fig. 2.17.

Note that Er^{3+} PL intensity and Si-NC PL wavelength follow the same general trend (bottom left to top right), emphasizing the importance of the Si-NC size towards the efficiency of the energy transfer. Numbered dots in Fig. 2.17 mark the conditions (x and T_{anneal}) for which maximum Er^{3+} emission was measured for each respective film (i.e. the maximum value on the color bar). The Si-NC emission wavelengths indicated are without exception close to $\lambda = 660$ nm, corresponding to a bandgap energy of E = 1.88 eV and a mean Si-NC diameter of about 2.8 nm, as determined by high-resolution electron microscopy (HREM) by Wang *et al.*[19]. This is the same wavelength for which selective quenching was observed, when comparing photoluminescence spectra of undoped and Er-doped SiO_x films as shown in Fig. 2.11. Other experiments[82,83] report on resonant energy transfer between Si-NCs and the $^4I_{11/2}$ state and the $^4I_{9/2}$ state of Er^{3+} ions in the SiO_x:Er material system. The observations made in this work indicate that the energy transfer between Si-NCs and Er^{3+} ions is most efficient when the excited states overlap with the $^4F_{9/2}$ energy level of Er^{3+} .

A simplified schematic of the excitation, energy transfer, and relaxation (neglecting back-transfer, upconversion, etc.) is shown in Fig. 2.18. The Si-NCs are represented by a three-level system, where a carrier is excited from the ground state

to an excited state by the pump light (upward arrow) and subsequently relaxes to a given sub-gap state (shaded region). If an optically active Er^{3+} ion is close enough to the nanocluster, energy can be transferred from the excited levels of the Si-NC to the erbium. The arrow labeled (a) represents a quasi-resonant transfer to one of the erbium levels; arrow (b) indicates possible phonon-assisted transfers to lower energy levels. The erbium levels populated by the energy transfer rapidly decay non-radiatively to the $^4I_{13/2}$ energy level. A photon with wavelength 1.54 μm can then be emitted upon recombination with the $^4I_{15/2}$ ground state.

Although the PL spectrum of the Si-NCs overlaps with other Er^{3+} levels for various compositions and annealing temperatures, the energy transfer seems most effective to the $^4F_{9/2}$ level. The weak 1.54 μm luminescence for the $SiO_{1.8}$:Er film could therefore be due to the fact that the amorphous clusters never reach the favorable size to support efficient energy transfer to this level.

It is noteworthy that the Er^{3+} photoluminescence intensity seems to depend predominantly on the Si-NCs size, rather than on the nanocluster PL intensity. For example, Si-NC PL intensity decreases for annealing temperatures between 700°C and 900°C , and is strongest for $T_{anneal} > 1000$°C . Er^{3+} emission at 1.54 μm on the other hand is more intense for annealing temperatures below 1000°C . In other words, it seems unnecessary for the Si-NCs to be good light emitters themselves in order to be good erbium sensitizers.

2.4.3.8 Temperature effects on SiO_x:Er photoluminescence

By placing SiO_x:Er samples in a liquid nitrogen cooled cryostat, the effect of temperature on Si-NC and Er^{3+} photoluminescence was investigated. Upon cooling to a minimum of $T = 77$ Kelvin and reheating to room-temperature (∼295 Kelvin), PL spectra and dynamics were recorded and analyzed as a function of temperature for both visible (550 - 750 nm) and near-infrared (around 1.54 μm) wavelengths.

2.4.3.8.1 Photoluminescence spectra as a function of PL temperature

Fig. 2.19(a) shows the change in the Si-NC photoluminescence peak wavelength as a function of temperature for a $SiO_{1.5}$:Er film annealed in forming gas at 800°C . A slight blueshift (∼10 nm) in the emission spectrum can be observed upon increasing the sample temperature from 77 K to 295 K.

The Er^{3+} emission lines around 1.54 μm on the other hand do not shift as a function of temperature, but a change in the overall shape of the spectra can be observed as shown in Fig. 2.19(b). Here, the recorded PL spectra for identical $SiO_{1.5}$:Er films are displayed for temperatures of 77 K and 295 K after normalization to the peak intensity at 1535 nm. Red curves indicate data recorded after annealing at T_{anneal} = 800°C (i.e. the Si-NCs in this specimen are amorphous), whereas black curves represent data collected after annealing the $SiO_{1.5}$:Er film at 1100°C , the embedded Si-NCs were crystalline in this case.
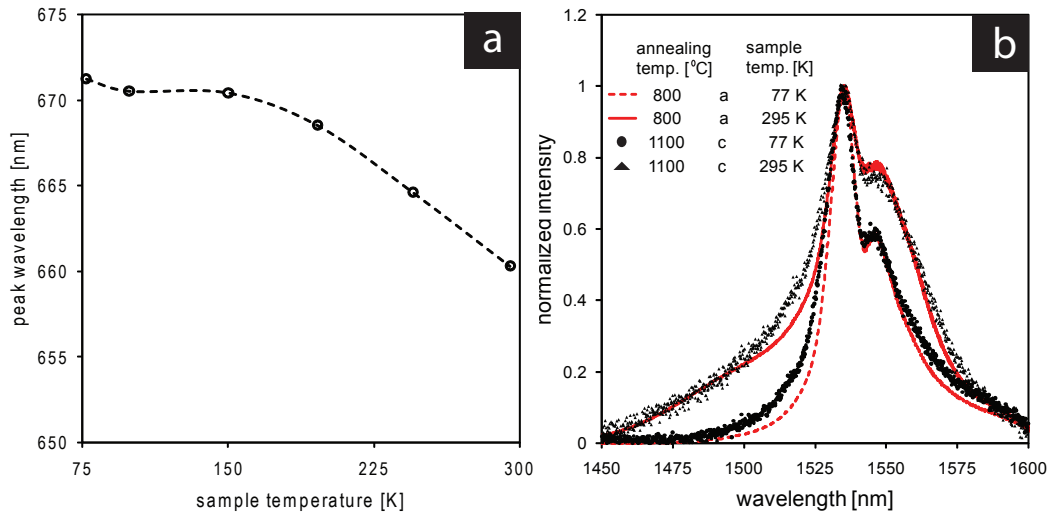
Fig. 2.19: Temperature effects on the photoluminescence spectra of Si-NCs and Er^{3+} ions in SiO_x:Er materials. (a) illustrates the shift in peak wavelength for the PL spectra of a $SiO_{1.5}$:Er film annealed at 800°C . (b) shows the normalized spectra at 1.54 μm for the same film annealed at 800°C and 1100°C and cooled to 77 Kelvin.

The overall spectral shape of the Er^{3+} photoluminescence did not depend on whether the sensitizing nanoclusters were amorphous or crystalline, as the red and black curves match each other well for both temperatures. Although the position of the primary (around 1535 nm) and secondary (around 1550 nm) peak did not change upon increasing the temperature of the sample from 77 Kelvin to 295 Kelvin (room-temperature), Fig. 2.19(b) shows, that the PL intensity of the secondary peak (or 'shoulder') was increased relative to the main peak. Also, higher PL intensities were observed for the shorter wavelength side of the peak, accompanied by an overall broadening of the spectra. These phenomena were consistent with the expected change in the temperature-dependant population distribution within the Er^{3+} level manifolds (see section 1.3) and the resulting transition probabilities. In appendix C, Er^{3+} emission spectra have been fitted with possible transition wavelengths and intensities - represented by gaussian curves - allowing the determination of sub-levels and corresponding energies within the $^4I_{13/2}$ and $^4I_{15/2}$ manifolds.

2.4.3.8.2 Photoluminescence intensity as a function of PL temperature

The integrated PL intensity for emission spectra of both a-Si-NC and c-Si-NC sensitized SiO_x:Er films was determined at various sample temperatures as shown in Figs. 2.20(a) and (b) for the photoluminescence at 1.54 μm from a SiO:Er sample annealed 500°C and 1000°C , respectively. Pump photon flux, PL collection time, and experimental setup remained unchanged for all measurements to enable
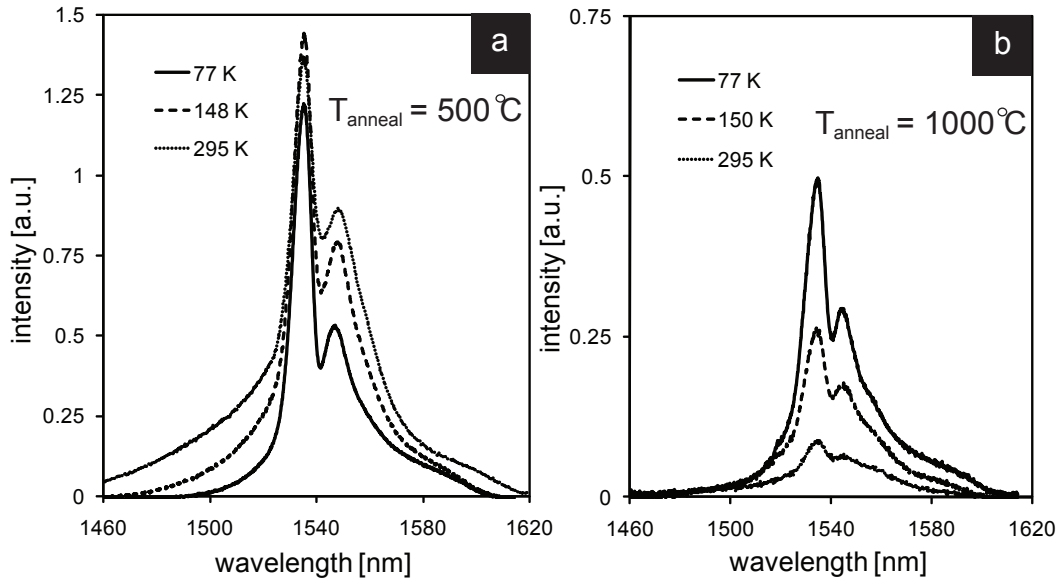
Fig. 2.20: Photoluminescence spectra of SiO:Er annealed at 500°C (a) and 1000°C (b) at temperatures of 77 K, 150 K, and 295 K.

quantitative comparison of the recorded spectra. Fig. 2.20(b) presents PL spectra collected at 77, 150, and 295 Kelvin from the sample containing crystalline nanoclusters. Clearly, the Er^{3+} emission is most intense for lower PL temperatures and decreases to about 20% of the peak value upon warming to room-temperature. This behavior is generally referred to as *thermal quenching*, where the intensity is decreased due to increasing probability for non-radiative decay with temperature, and corresponds well to thermal quenching reported elsewhere.[112,113] The Er^{3+} PL spectra obtained for $T_{anneal} = 500°C$ on the other hand exhibit a quite different effect. In this case an increase in photoluminescence intensity with increasing temperature was observed (Fig. 2.20 a). Although this phenomenon was observed for all films containing *a*-Si-NCs, it was most significant for the most silicon-rich SiO:Er film annealed at the lowest temperature (500°C). It is noteworthy that this increase in intensity does not occur homogeneously over the whole wavelength range, but rather in the form of the aforementioned change in emission spectra (i.e. increased intensity in the short and long wavelength regions). The peak intensity at 1535 nm remains relatively constant.

Fig. 2.21 presents plots of the integrated photoluminescence intensity with decreasing temperature on a logarithmic scale. In (a) the integrated Er^{3+} PL intensities for SiO_x:Er samples containing amorphous nanoclusters are shown in red for Er-doped films of compositions SiO, $SiO_{1.5}$, and $SiO_{1.7}$ annealed at temperatures of 500°C , 800°C , and 900°C , respectively, to optimize the sensitization process (i.e. $E_g = 1.88$ eV or $\lambda = 660$ nm). Shown in black are the integrated Er^{3+} PL intensities obtained from the same films after annealing at $T_{anneal} > 1000°C$; the Si-
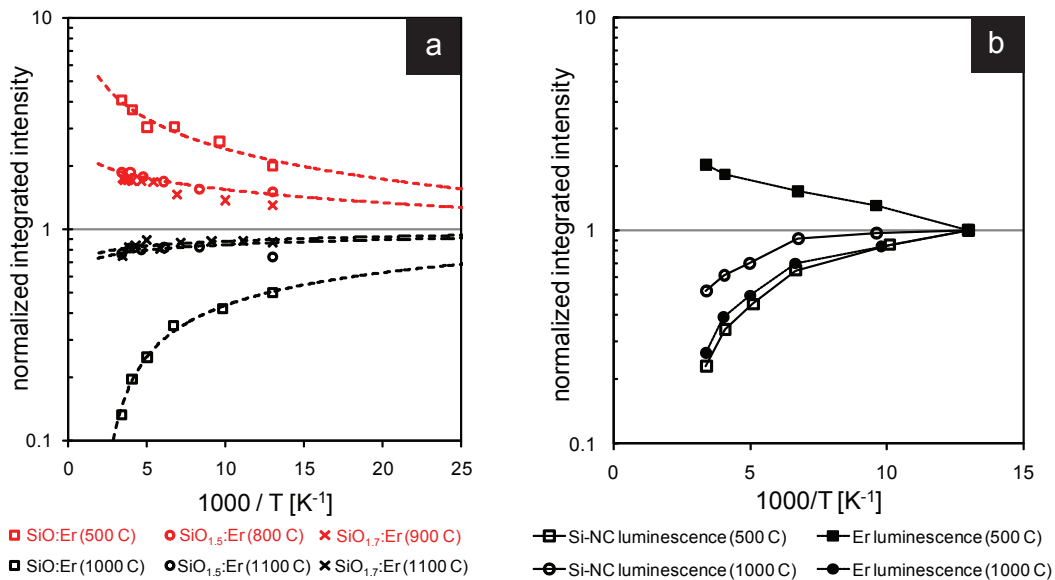
Fig. 2.21: Temperature-dependent integrated PL intensities for various SiO_x:Er compositions and annealing temperatures. (a) comparison of integrated Er^{3+} PL intensities for various SiO_x:Er films containing amorphous or crystalline Si-NCs, respectively. (b) comparison of integrated Si-NC and Er^{3+} PL intensities depending on temperature for SiO:Er ($500°C$ and $1000°C$).

NCs are now crystalline. Data points are fitted with logarithmic curves presenting a guide to the eye and normalized to low temperature values estimated from the same fits. The different (i.e. nearly opposite) effect of temperature on SiO_x:Er films containing crystalline and amorphous Si-NCs is clearly evident.

Fig. 2.21(b) compares the integrated PL intensities in the visible (Si-NC photoluminescence) and 1.54 µm (Er^{3+} photoluminescence) from the above SiO:Er film annealed at $500°C$ and $1000°C$. Curves are normalized to the value measured at a temperature of 77 Kelvin. The Si-NC PL intensity decreases with increasing temperature independent of wether the nanoclusters are amorphous or crystalline, thermal quenching is slightly reduced in the crystalline case. Er^{3+} PL intensity for $T_{anneal} = 1000°C$ is thermally quenched as well, in fact closely matching the decrease in the Si-NC PL intensity. The scaling of Er^{3+} intensity with Si-NC intensity suggests that energy transfer occurs predominantly from light emitting ('bright') silicon nanoclusters rather than 'dark' carriers. As the Si-NC PL becomes quenched, so is the transfer and therefore the Er^{3+} PL.

Once again, the Er^{3+} PL intensity for $T_{anneal} = 500°C$ showed opposite temperature dependent behavior and did not scale with Si-NC PL, suggesting that energy is not predominantly transferred to the Er^{3+} ions from the emitting Si-NC, but some other source, such as 'dark' nanoclusters or defect centers, which are not experiencing thermal quenching to the same degree. Reduced energy back-transfer from the ions to the nanoclusters might also contribute to the observed phenomenon.

2.4.3.8.3 Photoluminescence dynamics as a function of PL temperature

In addition to intensity measurements, photoluminescence dynamics investigations were conducted for both Si-NC and Er^{3+} emission. Recorded PL decay traces for a $SiO_{1.4}$ film annealed at $700°C$ containing amorphous silicon nanoclusters for various temperatures are shown in Fig. 2.22(a). The PL decay consists of a fast drop and a relative slow component as described previously. Upon cooling the sample
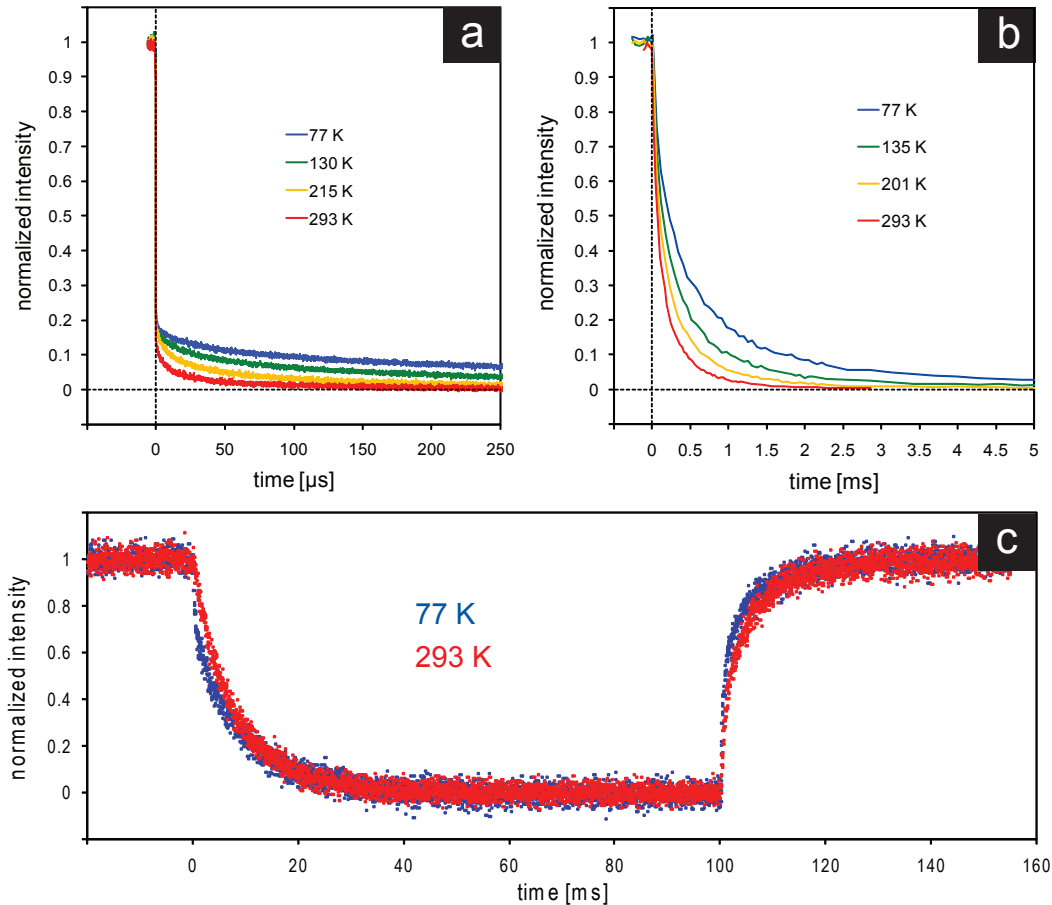
Fig. 2.22: Temperature-dependent PL intensity decay for Si-NC and Er^{3+} photoluminescence. (a) amorphous Si-NC photoluminescence from $SiO_{1.4}$ annealed at $700°C$, (b) crystalline Si-NC photoluminescence from $SiO_{1.5}$ annealed at $1100°C$, (c) Er^{3+} photoluminescence from $SiO_{1.7}$:Er annealed at $900°C$.

to temperatures of 215 K, 130 K, and 77 K no change in the initial intensity drop is observed (within the time resolution of our detection system). The decay lifetime of the "tail" (slow) component of the decay, however, increases significantly with decreasing temperature. Despite this, the ratio between the fast and slow components ($\sim 5 : 1$) is uneffected. Fig. 2.22(b) presents temperature-dependent PL intensity decay curves for a $SiO_{1.5}$ film annealed at $1100°C$, containing crystalline silicon

nanoclusters. As for the "tail" component in the amorphous case, an increase in decay lifetime with decreasing temperature is clearly evident. Decay times and stretching factors determined for both samples from a stretched exponential fit are presented in table 2.7.

Stoichiometry-T_{anneal}	77 K	135 K	201/215 K	293 K
SiO$_{1.4}$-700°C (tail)	$\tau_{decay} = 401.2\ \mu s$ $\beta = 0.49$	$\tau_{decay} = 124.0\ \mu s$ $\beta = 0.45$	$\tau_{decay} = 40.1\ \mu s$ $\beta = 0.43$	$\tau_{decay} = 14.5\ \mu s$ $\beta = 0.39$
SiO$_{1.5}$-1100°C	$\tau_{decay} = 398.2\ \mu s$ $\beta = 0.82$	$\tau_{decay} = 317.6\ \mu s$ $\beta = 0.80$	$\tau_{decay} = 265.0\ \mu s$ $\beta = 0.78$	$\tau_{decay} = 189.7\ \mu s$ $\beta = 0.76$

Table 2.7: Temperature dependent Si-NC decay lifetimes and stretching factors.

Contrary to the increase in decay lifetimes seen in Si-NC PL intensities at lower temperatures, the Er^{3+} decay lifetimes were relatively independent of temperature as shown in Fig. 2.22(c) for SiO$_{1.7}$:Er annealed at 900°C . Neither decay nor rise traces showed any noticeable effect upon cooling the film sample from room-temperature (293 K) to 77 K as illustrated by the close match between the two curves.

<div style="text-align: right">CHAPTER **3**</div>

SiO$_x$:Er optical waveguides

3.1 Introduction

The sensitizing effect of Si-NCs on Er^{3+} ions might enable integrated optical amplifiers with unique attributes. To this end, fabrication of light confining waveguide structures based on the SiO$_x$:Er films from chapter 2 was explored. In the following, the design, fabrication, and characterization of these waveguides is described.

3.2 Waveguide structures

Optical waveguides exist in a variety of different types, generally classified according to their structure or geometry. Optical fibers are a well known type of waveguide used in long-haul communication networks, whereas designs more suitable for integrated microphotonics include planar waveguides, channel waveguides, and rib or rib-loaded waveguides. The latter two types were realized in this work, as shown schematically in Fig. 3.1.

Choosing the appropriate layer dimensions – especially for the core layer – is essential when designing optical waveguides. In order to avoid interference between different guides modes (so-called "mode beating") it is beneficial to restrain the dimensions and only allow a single mode (i.e. usually the fundamental mode) to be confined and propagate within the waveguide. To achieve efficient coupling on the other hand, one would want to match as closely as possible the mode-field of the optical waveguide to that of the coupling fiber used. A large contrast between the refractive indices of the core material and the cladding material is preferential in order to achieve strong light confinement and maximize the overlap of the active core region with the waveguide mode-field.

A mode solving software (Mode Solutions 3.0 by Lumerical) was used to in-
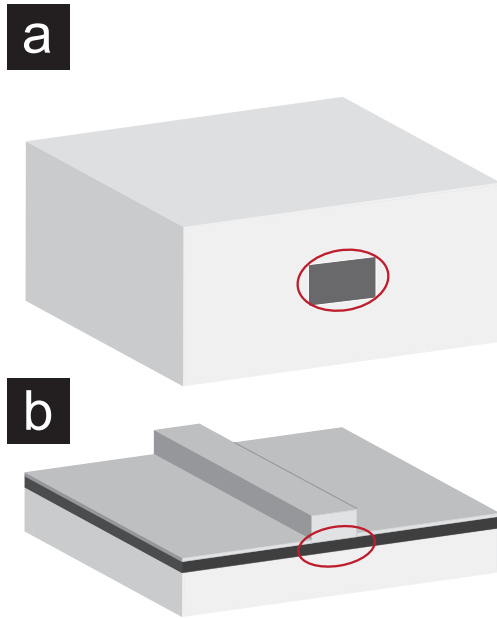
Fig. 3.1: Schematic of channel- and rib- type integrated waveguides fabricated from SiO$_x$:Er films in this work. The top image shows a channel waveguide; a strip of core material being completely surrounded by a cladding with lower refractive index. The bottom picture depicts a rib-loaded waveguide; light is confined in the core material layer through a cladding rib on top. Red circles in both images emphasize the region in which light confinement occurs.

vestigate and predict the modal characteristics and light confinement properties of the fabricated channel and rib-loaded waveguides. The waveguide design was generally guided by the aforementioned goals of efficient fiber coupling and minimization of the number of modes.

3.2.1 Channel waveguides

Channel waveguides consist of a core region embedded completely in a cladding material of lower refractive index. A special example of a channel waveguide is an optical fiber. In contrast to optical fibers, channel waveguides in integrated photonics do not typically have a round profile, due to the planar processing steps employed.

Figures 3.2(a) and (b) show the calculated transverse-electric (TE) modes for a channel waveguide with a SiO:Er core ($n \sim 1.9$) surrounded by a benzocyclobutene (BCB) polymer cladding obtained using the mode solving software. Only the fundamental TE mode (see Fig. 3.2 a) and first-order TE mode (see Fig. 3.2 b) are shown, but several transverse-magnetic (TM) modes were also predicted.

3.2.2 Rib-loaded waveguides

In contrast to channel waveguides, rib and rib-loaded waveguides do not comprise a fully embedded (i.e. within the cladding material) strip or cylinder of core ma-
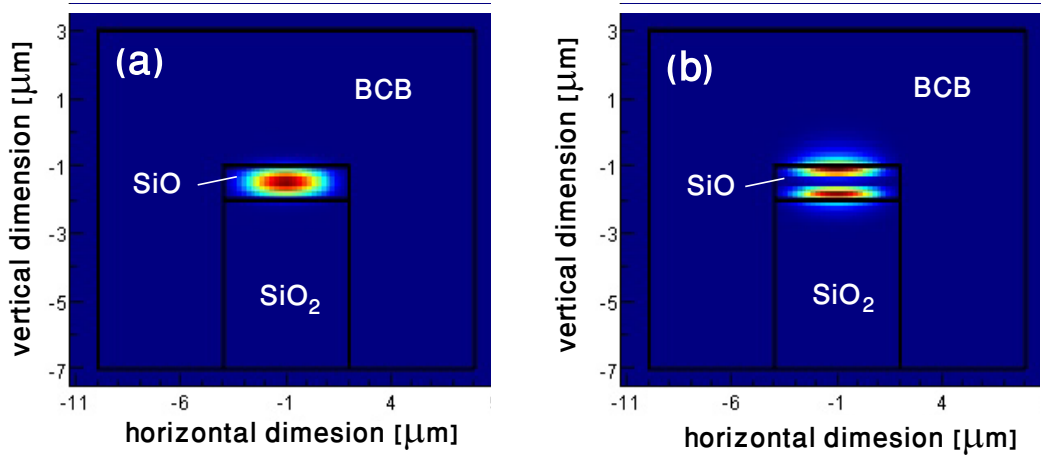
Fig. 3.2: Modesolver graphs showing possible modes in a channel waveguide of SiO (n=1.9) with the core dimensions 1x6 μm . (a) shows the fundamental TE mode with characteristic Gaussian electric field distribution, whereas (b) presents the first order TE mode. Higher order TE mode solutions were not found for this structure.

terial. Instead, light confinement is achieved within the continuous core layer by either shaping the core material into a rib itself or by forming a rib of cladding material on top as illustrated in Fig. 3.1(b). Since direct etching of the SiO_x:Er materials proved impractical and produced poor results (see section 3.3), the latter approach was chosen in this work.

One way to understand how the rib structure creates two-dimensional confinement of light (as shown for example in Fig. 3.3 a), is by applying the effective index method. In brief, the rib-loaded structure is divided into a region ① on the left and right of the rib, and a region ② including the rib, as illustrated in the bottom of Fig. 3.3 (b). By treating each region separately, and solving the according eigenvalue equation for the propagation of an electro-magnetic wave in each vertical multi-layer slab, one can determine an effective refractive index for each region. The effective index of region ② will be slightly higher than that obtained for region ①, due to the additional high index (compared to $n = 1$ for air) portion of the waveguide rib. Using these refractive index values, one may now solve the eigenvalue equation for the equivalent slab in the horizontal direction, as shown schematically in the top of Fig. 3.3 (b). The darker shaded region corresponds to the rib and underlying layers with slightly higher effective index.

Although the core layer is continuous, light can therefore be confined underneath and within the rib to form a two-dimensional optical waveguide. Figure 3.3(a) presents the calculated (via Mode Solutions 3.0 by Lumerical) result for the fundamental mode of a rib-loaded waveguide with a $SiO_{1.7}$:Er core and SiO_2 undercladding and rib. The inset of Fig. 3.3 shows the mode-field of the equivalent fabricated waveguide recorded with an infrared CCD-camera. The Mode Solutions
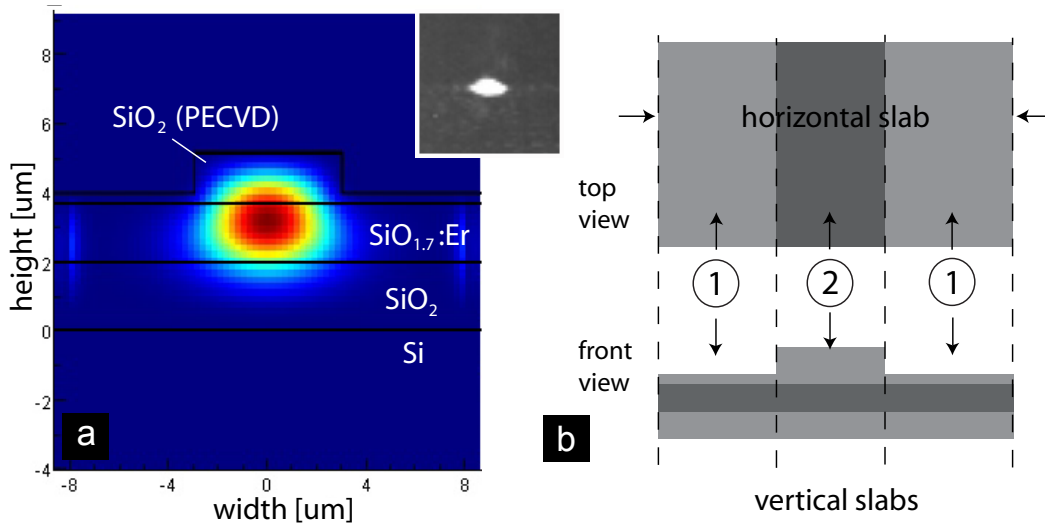
Fig. 3.3: Propagation mode simulation for a rib-loaded waveguide structure. (a) shows the calculated TE fundamental mode for a simulated waveguide structure with a core of $SiO_{1.7}$:Er. The TE fundamental mode is in fact the only supported guided mode in this case, the waveguide would therefore be single-moded. The inset features the mode-field of such a waveguide recorded with an infrared CCD-camera. (b) illustrates the effective index method.

3.0 software was used to investigate alternative SiO_x:Er core films and rib dimensions, mainly to determine single-mode conditions.

3.3 Fabrication of SiO_x:Er optical waveguides

3.3.1 Channel waveguides

The fabrication process used to realize channel waveguides was based on previous work in our group.[114] A step-by-step schematic of this technique and the involved processing steps is illustrated in Fig. 3.4.

Following cleaning of the silicon substrate in a mixture of hydrogen peroxide and sulfuric acid (a solution commonly known as piranha in reference to its ability to 'eat away' organic materials as does the famous little fish named *piranha*), a layer of SiO_2 (about 400 nm thick) was grown on the silicon surface by thermal steam oxidation. The desired waveguide structures were thereafter patterned into the SiO_2 layer via a standard lithography process. In this process, the samples were first treated with hexamethyldisilizane (HMDS), a photoresist adhesion promoter, followed by spin-coating of the sample surface with a positive-tone photoresist (HPR-504). The waveguide pattern (straight lines with varying lateral width ranging from 1 μm to 6 μm in steps of 0.5 μm) from an existing positive-image photomask[114] was thereafter transferred into the photoresist via exposure to ultraviolet (UV) light in a mask-aligner lithography unit. The patterned photoresist serves as
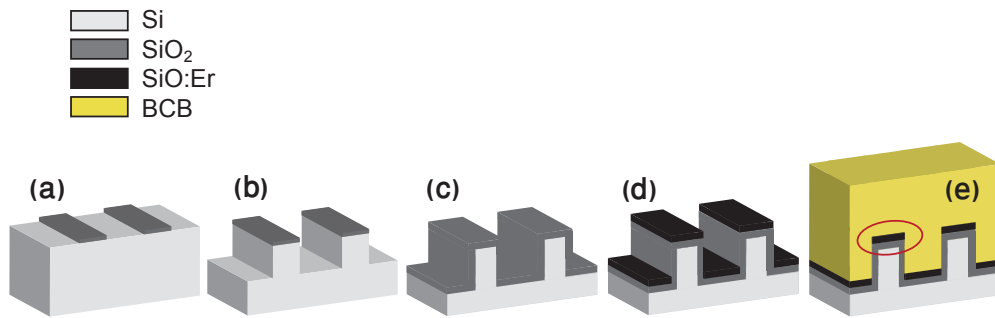
Fig. 3.4: Processing steps in channel waveguide fabrication: (a) an SiO_2 etch mask is deposited and patterned on top of a silicon substrate; (b) RIE of the silicon except where it is protected by the SiO_2 mask, thereby creating post structures; (c) thermal steam oxidation to build the waveguide undercladding; (d) deposition of the actual SiO_x:Er core material via PVD; (e) spin-on and curing of BCB as cladding material completes the channel waveguides.

etch-mask for the subsequent buffered-oxide-etch (BOE) of the underlying SiO_2 as illustrated in Fig. 3.4(a).

The resulting SiO_2 strips serve as the etch-mask for inductively-coupled plasma reactive-ion-etch (ICPRIE - process gas mixture of O_2 and SF_6) of the silicon, taking advantage of the much higher etch rate of silicon compared to SiO_2 ($\sim 500 : 1$). This Si-etch creates posts of silicon about 6 μm in height (see Fig. 3.4 b). As illustrated in Fig. 3.4(c), thermal steam oxidation for 16 hours at $1000°C$ was performed to transform the top 2 μm of the silicon (including the posts) into SiO_2 , which served as the low index undercladding in the waveguide structure. Subsequently, the core layer of SiO or SiO:Er was deposited, covering the SiO_2 undercladding but not the post sidewalls as illustrated in Fig. 3.4(d). After deposition, the post structures were annealed in order to promote Si-NC formation and growth in the core layer. Finally, the channel waveguides were spin-coated with a $\sim$10 μm layer of benzocyclobutene (BCB) polymer to completely cover the waveguide structures. The BCB layer reduces the waveguide propagation losses due to scattering and protects the waveguide structures from external damage. The final channel waveguide structure is shown schematically in Fig. 3.4(e).

Scanning-electron microscopy (SEM) images of the fabricated channel waveguides without top BCB layer are presented in Fig. 3.5. In (a), the sidewalls of the post were etched into an hourglass shape and shadowed during PVD by the SiO_2 mask on top of the post. The line-of-sight is interrupted and the sidewalls remain free of SiO_x:Er deposit. In (b), the highly directional deposition flux (normal to the substrate plane) results in formation of a highly porous layer consisting of angled columns or needles on the sidewalls; this effect is often referred to as *glancing angle deposition* (GLAD).[115] It is evident from these SEM images that uniform guiding layers with little sidewall roughness can be produced using these process steps.
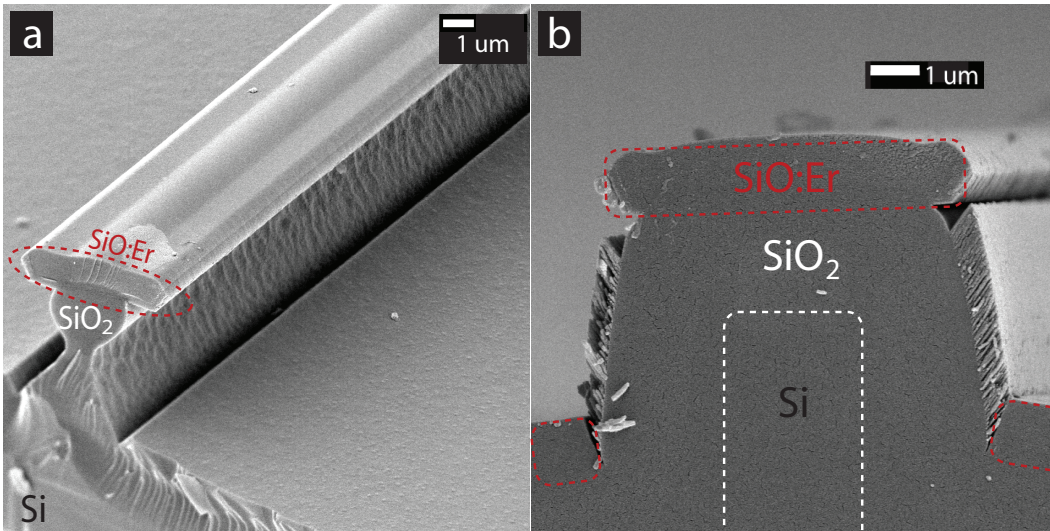
Fig. 3.5: SEM picture of fabricated channel waveguides excluding BCB layer. In (a) an hourglass shape is shown, created by 'over-etching' of the silicon post. No SiO_x:Er material is deposited on the sidewalls. (b) shows a channel waveguide with steep post sidewalls, resulting in SiO_x:Er deposit via glancing-angle deposition (GLAD). The dashed line indicates the position of the $SiO_x - SiO_2$ interface.

3.3.2 Rib-loaded waveguides

A rib-loaded waveguide is a relatively simple integrated structure, and can be fabricated with a minimum number of processing steps. A straightforward approach to create such waveguides would be to etch the rib directly into the guiding layer material, i.e. the deposited SiO_x:Er layer.

Attempts to etch ribs into SiO[114] and $SiO_{1.9}$ film deposited via PVD were undertaken by means of BOE and RIE, as both techniques are commonly used in direct patterning of SiO_2 . In the case of films deposited with the previously-described PVD technique, BOE etching results were rather poor. The BOE wet etch process showed inconsistent etch rates, and the occurrence of micrometer sized pinholes and large surface roughness was observed as shown in Fig. 3.6. On the other hand, RIE resulted in significant sidewall and surface roughness caused by high-power bombardment[114]. It is reasonable to associate these poor results with the deposition technique used, since the same etch processes produced much better results for SiO_2 films deposited by plasma-enhanced chemical vapor deposition (PECVD) of a mixture of tetrahylorthosilicate (TEOS) and oxygen gases.

As a result, SiO_2 rib-loaded waveguide structures (see Fig. 3.7) were realized using the following processing steps. First, a 2 µm thick SiO_2 layer was grown on a silicon-wafer substrate by thermal oxidation in a wet (steam) oxidation furnace ($T = 1000°C$). Subsequently, a SiO_x:Er waveguide guiding layer was deposited via PVD. This process was described in detail in section 2.2. Annealing of the samples in forming gas (H_2+N_2) results in the formation of Si-NCs. Thereafter, a layer of
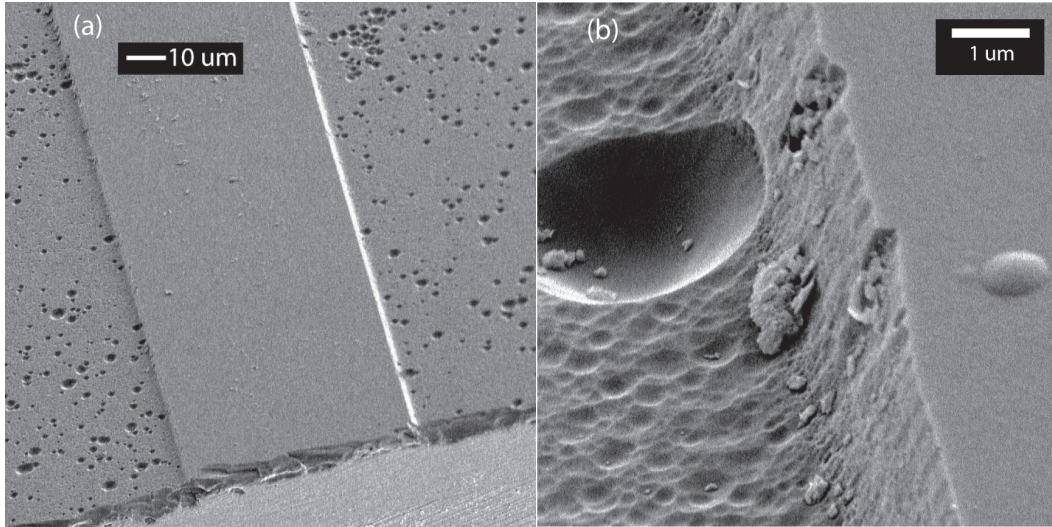
Fig. 3.6: SEM images of waveguide structures created by direct wet etching of $SiO_{1.9}$ in BOE; (a) shows big craters left behind by the etch, and the greater magnification in (b) reveals surface and sidewall roughness.

SiO_2 was deposited on top via PECVD and patterned using a standard lithography process, followed by "wet" or "dry" etching of the SiO_2 to create rib structures. Rib structures of heights between 0.4 to 1 µm were created via buffered-oxide etch (BOE) and possessed good edge definition and low sidewall roughness, as shown in Fig. 3.7 (b). The rounded and angled ($\sim 45°$) sidewalls are typical for an isotropic liquid-phase (wet) etchant.

Reactive-ion etching (RIE) was used to realize rib structures with heights in excess of 1 µm . RIE (process gas mixture: O_2 + CHF_3) is an anisotropic (i.e. unidirectional) plasma-phase (dry) etch, resulting in steep vertical sidewalls. Figure 3.8 shows a top view SEM image of a rib structure etched via RIE. The substantial sidewall roughness resulting from the reactive-ion etch process is evident.

3.4 Experimental: Waveguide analysis

In the present work, optical waveguides of different types, dimensions, and compositions were characterized in terms of optical losses and signal absorption and emission. A summary of the investigated waveguides showing key properties (including the core confinement factor Γ) is given in table 3.1.

3.4.1 Propagation loss measurements via the cutback technique

Waveguide losses can arise from intrinsic material properties, such as absorption and scattering, or extrinsic fabrication-related issues, such as interfacial scattering (e.g. at rough sidewalls). The term *propagation loss* is commonly used to refer to the
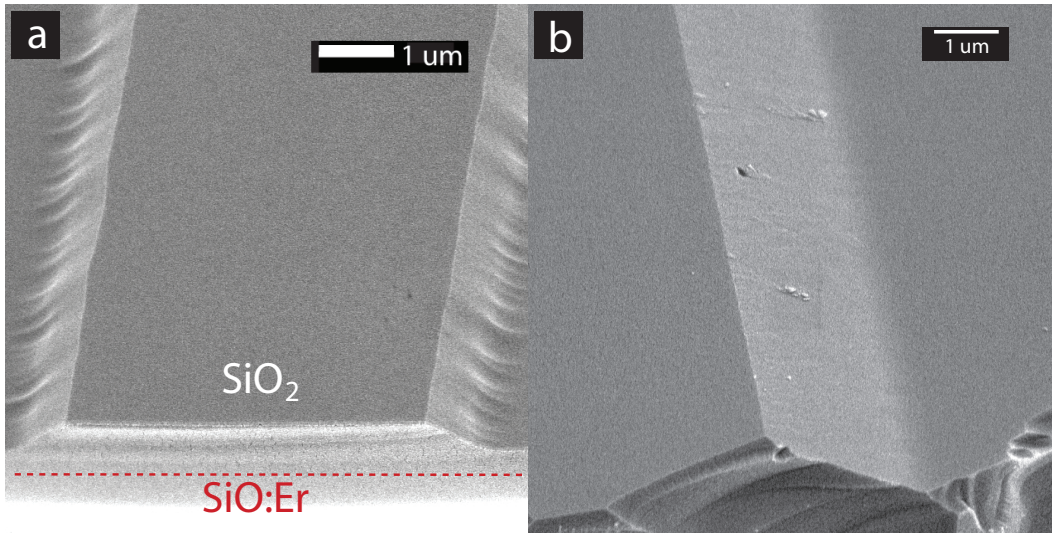
Fig. 3.7: SEM images of a rib-loaded waveguide fabricated by wet etching of PECVD-oxide. (a) is a profile view of a 5 µm wide rib structure, exhibiting some sidewall roughness in the form of ripples at the bottom of the rib, (b) is a close-up view of the sidewall of one of the larger rib structures, illustrating the low level of roughness achieved.

sum of all these losses.

The cutback technique is a relatively simple method to determine the propagation loss in optical waveguides (Fig. 3.9). In brief, light is coupled into a relatively long piece of a low-loss optical waveguide and the transmitted power (P_a) is measured. Subsequently, a small length of the waveguide is 'cut off', thereby shortening the propagation length that light travels within the guide. Shorter length results in less propagation loss and therefore increased transmitted power (P_b). Assuming equal coupling conditions and efficiency in both cases, the propagation loss of the waveguide can then be calculated as [116,117]

$$L_{wg}\,[\mathrm{dB/cm}] = -\frac{10}{l_{ab}}\log\left[\frac{P_a}{P_b}\right] \tag{3.1}$$

where $l_{ab} = a - b$ is the length of the waveguide section removed. The coupling losses can be estimated by using linear regression to calculate the power at the input facet and comparing the determined value to the measured output power of the coupling fiber.

In this work, channel and rib waveguides up to a length of about 2 cm were fabricated. Propagation losses were determined via the cutback technique, by cleaving off 2 or 3 pieces of length 3 - 12 mm each. All pieces were cleaved off the output facet of the wafer chip, maintaining the same conditions on the input coupling side to keep the coupling losses between the single-mode Nufern fiber and the waveguides as constant as possible. After optimizing the coupling for maximum trans-
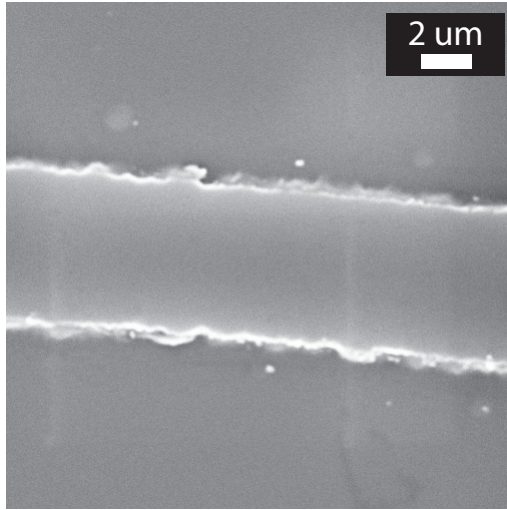
Fig. 3.8: SEM image (top view) of a rib-loaded waveguide fabricated via dry-etching (RIE) of PECVD-oxide. High sidewall roughness is evident, whereas the top surface seems smooth.

waveguide	C	R-1	R-2	U (undoped)
type	channel	rib-loaded	rib-loaded	channel & rib-loaded
active region				
height [μm]	1	1	1.7	1
width [μm]	1-6	1-6	1-6	1-6
stoichiometry	SiO:Er	SiO:Er	$SiO_{1.7}$:Er	SiO
core refractive index	1.9	1.9	1.46	1.9
Γ	0.92	0.93	0.64	0.93
Er in at.%	1	1	0.12	–
Er concentration [cm^{-3}]	6.0×10^{20}	6.0×10^{20}	0.72×10^{20}	–

Table 3.1: Summary of the investigated optical waveguides.

mission, the transmitted power ($\lambda = 1.3$ or 1.6 μm) was collected via a microscope objective (magnification $60\times$) and detected with a near-infrared photodiode (Newport 818-IR) connected to a calibrated optical power meter (Newport 1830C). As the photomask pattern provided a set of 9 parallel waveguides of equal width on each wafer chip, losses for all 9 waveguides were measured and averaged to eliminate effects occurring irregularly in one waveguide but not the other (e.g. scattering at an embedded particle).

3.4.2 Er^{3+} - and Si-NC- doped waveguide experiments

Absorption and emission experiments on optical waveguides (as opposed to thin films) can offer a new perspective on the investigation of optical properties in SiO_x:Er materials. Spontaneous and stimulated Er^{3+} emission is confined and guided within the waveguide, providing a directional and strong luminescence
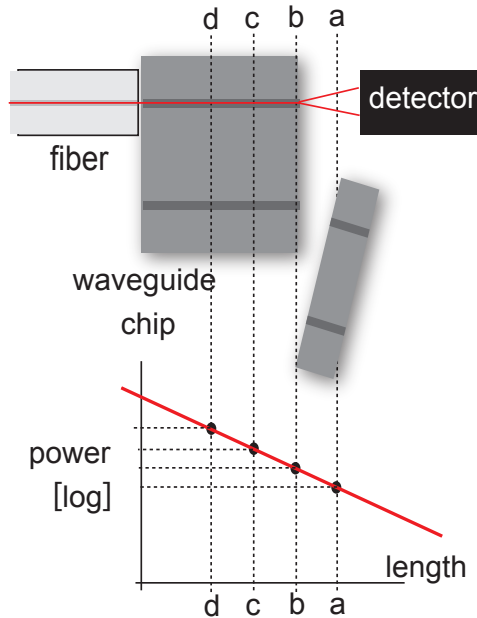
Fig. 3.9: Schematic illustration of the cutback technique. The top section of the image presents a simplified view of the measurement setup. Light (red) coming from a fiber is coupled into the optical waveguide, travels along the guide, and is detected after exiting the waveguide chip. Also indicated is the successive reduction in length from **a** to **b** to **c** to **d**. The bottom graph shows the measured values of transmitted power and the determination of the loss via linear regression (see results in section 3.5.1).

signal for analysis.

Figure 3.10 shows a schematic of the experimental setup used for photoluminescence measurements on the optical waveguides, analogous to the setup shown in Fig. 2.2 for the thin film case. Erbium ions within the waveguides can be excited directly (resonantly) or indirectly (non-resonantly) via sensitization from the embedded silicon nanoclusters. For resonant excitation of the Er^{3+} ions into their $^4I_{11/2}$ level, light with a wavelength of 0.98 μm from a fiber laser (TRLabs serial #:95485) was launched into the waveguide through the 0.98 μm port of a wavelength-division multiplexer (WDM). The light was coupled into the waveguide piece by aligning the end of the stripped Nufern single-mode fiber (core diameter 4 μm – mode-field diameter 4.8 μm) to the cleaved edge of the waveguide chip; a microscope objective and optical power meter (Newport 1830C) were used to optimize the positioning of the fiber for maximum coupling and transmission.

Non-resonant excitation of the Er^{3+} ions via Si-NCs can be achieved in two ways. Instead of the 0.98 μm pump laser, a different light source can be used to launch light into the end facet of the waveguide. Note that this approach of end-coupling of non-resonant pump light is not likely practical, due to the short absorption length of the pump light within the waveguide. Alternatively, the waveguides can be illuminated from above as illustrated in Figs. 3.10 and 3.11. Due to the broadband absorption of the silicon nanoclusters, the excitation wavelength need not be resonant with any erbium level and even broadband sources in the UV and visible wavelength range - such as light emitting diodes (LEDs) - might be usable, depending on the pump intensity required.

After excitation, the Er^{3+} ions emit light in the 1.54 μm wavelength regime,
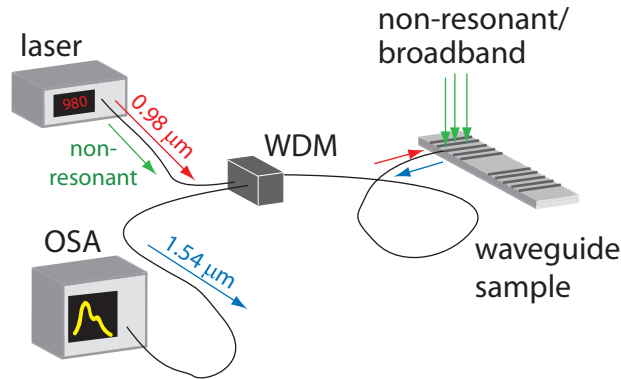
Fig. 3.10: Schematic of a waveguide photoluminescence experimental setup. Pump light exciting Er^{3+} ions directly or indirectly (via Si-ncs) is provided by a 980 nm pump laser or other sources launched into the waveguide through a coupling fiber or from above. Er^{3+} photoluminescence is collected with an OSA from the 1.54 µm port of the WDM.

some of which is confined to the waveguide core. The portion of light traveling in the backward direction can then be collected by the coupling fiber and exits the WDM through its 1.54 µm port, to be measured using an optical spectrum analyzer (OSA - Anritsu MS9710C).

In order to investigate the absorption and stimulated emission of a probe signal in the wavelength region of the $^4I_{15/2} \rightarrow {}^4I_{13/2}$ Er^{3+} transition at 1.54 µm , and to measure potential signal enhancement under different excitation schemes, an experimental arrangement as depicted in Fig. 3.11 was used. The probe signal (blue arrows) from a tunable fiber laser (Santec TSL-320) was scanned through the wavelengths from 1.52 µm to 1.62 µm and split into 2 parts by a 90/10 coupler. 10% of the total signal power was collected by a near-infrared photo detector (Newport 818-IS-1) and used to correct for variations in the wavelength dependent laser output power. The remaining 90% power was fed into a waveguide-division multiplexer (WDM) and coupled into the waveguide sample. Also, reference measurements were taken without the waveguides in place, and the data was used to account for the wavelength dependent response of the entire system.

As described previously, pump light can be either co-propagated with the probe light, or can be provided by directly illuminating the waveguide from above. Non-resonant pumping was attempted using a frequency-doubled Nd:YAG laser (CLM-50) with an output power of about 70 mW at a wavelength of 532 nm. The laser beam can be focused and shaped into a narrow line via a pair of lenses (at least one cylindrical lens), to better match the waveguide region and intensify the pump energy.

Transmitted light was collected at the opposite end of the waveguide via a microscope objective (60x) or a fiber with high numerical aperture. Residual pump light was eliminated by a long-pass filter, preventing light with a wavelength below ~1 µm to reach the detector, or by a band-pass filter (1.33 µm to 1.67 µm) only
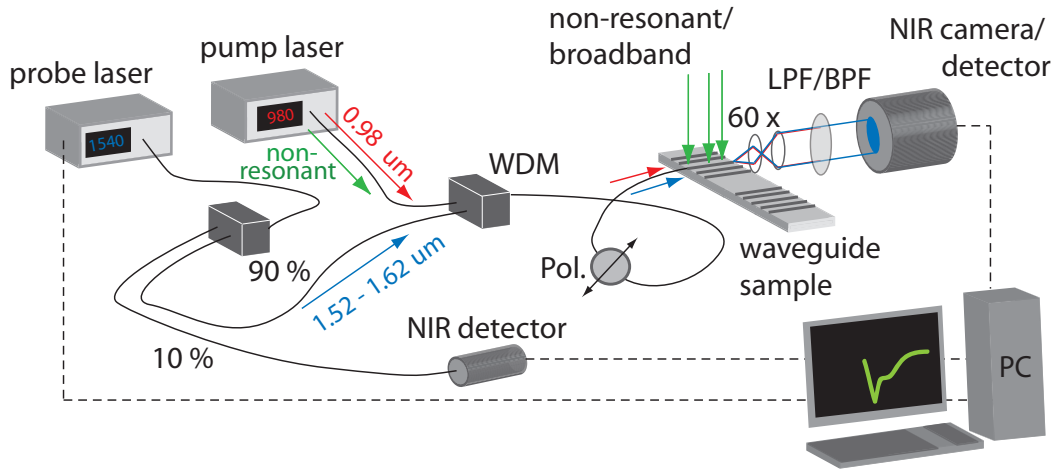
Fig. 3.11: Schematic of the experimental waveguide setup used to measure signal losses and gain under resonant and non-resonant pumping conditions. Pump (0.98 μm) and probe (1.52 - 1.62 μm) light were launched into the waveguide via a WDM and polarization controller (Pol). Also indicated (green arrows) is possible non-resonant pumping from above. Light exiting the opposite end of the waveguide sample was collected by a microscope objective (60x) and recorded via a near-infrared camera or germanium photodetector. A long-pass-filter (LPF) or band-pass-filter (BPF) eliminated residual pump light. Detector readouts were analyzed via PC.

allowing light from the Er^{3+} $^4I_{15/2} \rightarrow {^4I_{13/2}}$ transition to pass. The remaining signal was collected with a near-infrared photo detector (Newport 818-IR), recorded on a personal computer (PC), and corrected for the system response and variation in signal laser intensity. Prior to collecting the transmitted signal for the complete wavelength range, waveguide coupling was optimized, and polarization was tuned for maximum transmission. A polarization controller (Pol) enables the selection of a predominant polarization (TE or TM) to be coupled into the waveguide modes.

The photo detector can be replaced by an infrared CCD-camera (Sensors unlimited, Inc.) in order to image the output mode-field of the waveguides, as well as to ensure that pump and probe light are indeed coupled into the waveguide modes and not propagating beneath or above the actual core, or as a slab mode in the SiO_x:Er layer on either side of the waveguide.

3.5 Results & Discussion

3.5.1 Waveguide losses

The characterization of the waveguide propagation losses, i.e. the attenuation of signal power over a given length of waveguide, constitutes an important part of the waveguide design process. If the propagation losses in an optical waveguide are
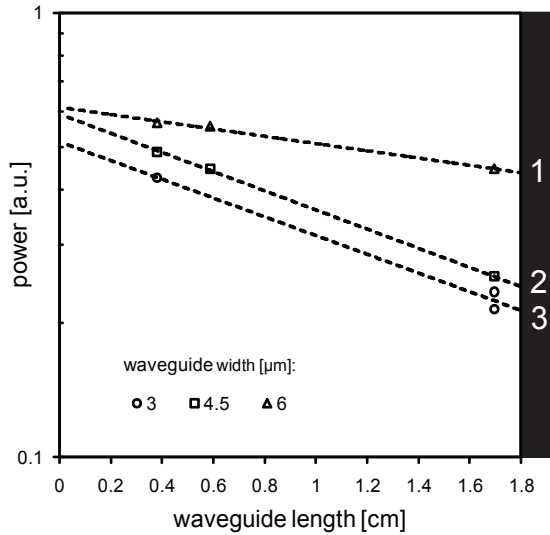
Fig. 3.12: Propagation losses of waveguide C with varying widths.

minimized, compensation of these losses via optical amplification can be achieved with even moderate gain coefficients.

To avoid absorption of the probe signal by Er^{3+} ions in the $^4I_{15/2}$ ground state, loss measurements in this work were conducted at wavelengths of 1.3 µm and 1.6 µm (rib-loaded waveguides only). At these wavelengths, the contribution of Er^{3+} absorption (centered around 1.54 µm) to the waveguide propagation losses is nearly zero (at 1.3 µm) or very small (at 1.6 µm), enabling an estimation of the 'pure' waveguide propagation and coupling losses. Propagation and coupling losses of fabricated channel- and rib-loaded waveguides (see table 3.1) were determined using the cutback technique described previously.

fit #	wavelength (nm)	width (µm)	propagation loss (dB/cm)	coupling loss (dB)
1	1300	6	0.8	6.0
2	1300	4.5	2.2	6.1
3	1300	3	2.1	6.8

Table 3.2: Propagation and coupling losses as shown in Fig. 3.12 for a waveguide C of widths 3, 4.5, and 6 µm at a signal wavelength of $\lambda = 1300$ nm.

Results for the measured transmitted powers ($\lambda = 1.3$ µm) for waveguides of type C are shown in Fig. 3.12 with the corresponding linear fit, the gradient of which is a measure for the waveguide propagation loss. The loss values determined from these data points via Eqn. 3.1 are presented in table 3.2. A propagation loss of 0.8 dB/cm was obtained for the 6 µm wide waveguide. Typical loss values for most of the narrower channel waveguides were approximately 2 dB/cm as shown for waveguide widths of 3 µm and 4.5 µm .
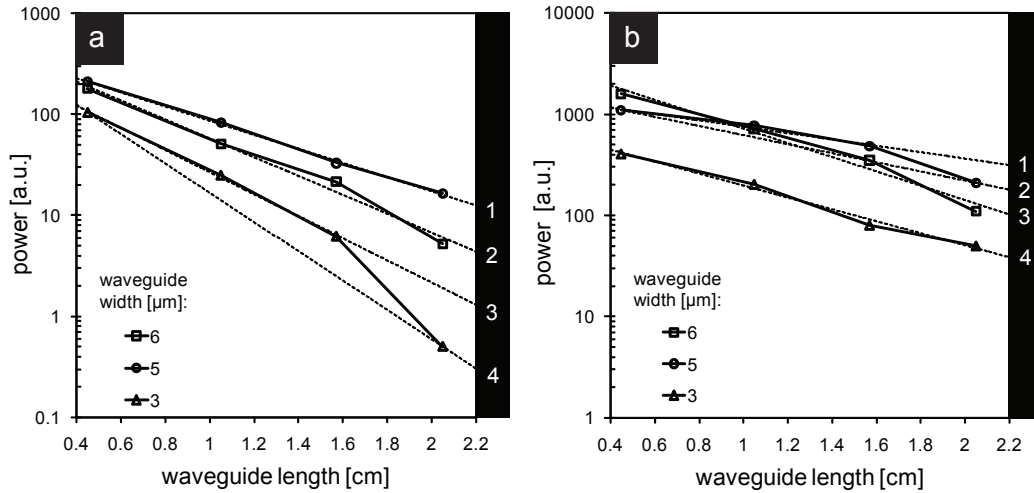
Fig. 3.13: Propagation losses of waveguide R-1 at $\lambda = 1300$ nm (a) and $\lambda = 1600$ nm (b) for different rib-widths of 3, 5, and 6 µm . Dashed lines are guides to the eye and possible data fitting curves represent different propagation loss values.

Measured transmitted powers for 3, 5, and 6 µm wide waveguides of type R-1 and the corresponding linear fits are shown in Figs. 3.13(a) and (b). Additional lines were added in some cases to illustrate how defects along one short section of waveguide can increase the overall propagation losses (e.g. fit 4 in Fig. 3.13 a) as compared to the waveguides without defect (e.g. fit 3 in Fig. 3.13 a). The determined propagation and coupling losses at wavelengths of 1.3 µm and 1.6 µm are presented in table 3.3. Typical propagation losses for waveguide R-1 are significantly higher than for waveguide C, ranging from 3.2 to 14.5 dB/cm. Also higher were the observed coupling losses, typically on the order of 8 to 10 dB.

fit #	wavelength (nm)	width (µm)	propagation loss (dB/cm)	coupling loss (dB)
a.1	1300	5	7.0	9.5
a.2	1300	6	9.3	9.0
a.3	1300	3	10.9	10.7
a.4	1300	3	14.5	9.2
b.1	1600	5	3.2	8.2
b.2	1600	5	4.5	7.7
b.3	1600	6	7.0	4.5
b.4	1600	3	5.9	11.3

Table 3.3: Propagation and coupling losses as shown in Fig. 3.13 determined for a waveguide R-1 of widths 3, 5, and 6 µm at signal wavelengths of 1.3 and 1.6 µm . Dashed lines are guides to the eye and possible data fitting curves represent different propagation loss values.

The substantial sidewall roughness (see Fig. 3.8) evident in waveguides of type R-2 causes high scattering losses and no transmission of light could be detected
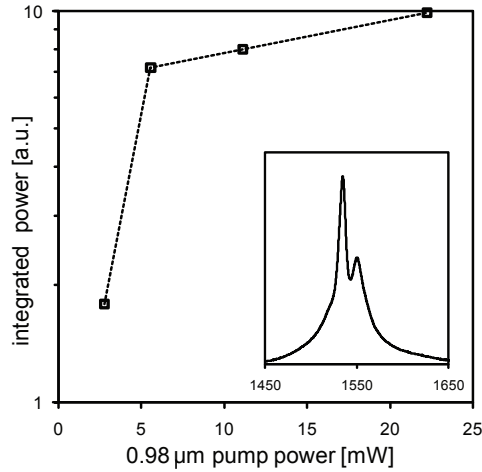
Fig. 3.14: Integrated PL intensities at 1.54 µm for resonant excitation ($\lambda = 0.98$ µm) with increasing pump powers. The inset shows the shape of the Er^{3+} emission spectra typically observed.

for waveguides longer than 5 mm. However, the insertion loss (i.e. the sum of coupling and propagation losses) was measured for this 5 mm waveguide to be around 38 dB. By estimating the coupling loss as 8 to 10 dB - as was determined for waveguide R-1 with similar dimensions - one can expect the propagation loss in this case to be approximately 60 dB/cm.

In summary, the collected data lends support to the conclusion that low loss waveguiding in SiO_x:Er based materials is possible, provided smooth sidewalls are created.

3.5.2 SiO_x:Er waveguide photoluminescence

A typical PL spectrum obtained from a SiO:Er channel waveguide using the setup in Fig. 3.10 is shown in the inset of Fig. 3.14, revealing the familiar Er^{3+} emission shape. Figure 3.14 illustrates the integrated photoluminescence power at 1.54 µm with increasing pump power for resonant pumping at 0.98 µm . As the pump power is increased by a factor of about 10, the integrated PL power only increases by a factor of approximately 5, indicating saturation behavior of the erbium inversion level at higher pump intensities (see section 2.4.3).

Attempts were made to observe 1.54 µm PL from the same waveguide under non-resonant pumping; i.e. via energy transfer from the Si-NCs to the Er^{3+} ions. To do so, pump light from a frequency-doubled Nd:YAG laser with wavelength 532 nm was either fed into the input fiber or delivered to the waveguide from the top. Both these strategies proved unsuccessful as no 1.54 µm emission could be detected by the OSA.

3.5.3   SiO$_x$:Er waveguide absorption

Wavelength resolved absorption spectra were recorded for a variety of fabricated waveguides using the setup described in section 3.4.2. The wavelength of the coupled and propagated light - hereafter referred to as "signal" - was scanned through the wavelengths from 1520 nm to 1620 nm and the transmitted power for each wavelength collected at the output of the waveguide. In order to eliminate signal power variations introduced by the fiber laser or other components of the system, each absorption spectrum was corrected using the corresponding spectrum recorded on the 10% port of the WDM as $P(\lambda) = P_{\text{trans}}(\lambda)/P_{10\%}(\lambda)$. Figures 3.15(a) and (b) show broadband scans recorded for waveguides of type R-1 and R-2, respectively.

A problem that was unfortunately encountered for almost all investigated waveguides is illustrated in Fig. 3.15(a). Although the typical Er^{3+} absorption peaks at 1534 nm and 1550 nm are clearly distinguishable in this case, periodic oscillations occurred, preventing useful analysis of the recorded data. The periodic character of these oscillations suggests some sort of interference effect. This was attributed to a combination of a "mode beating" effect and the fact that 0.1 nm or 1 nm wavelength steps were used in obtaining the data. Simply put, different modes traveling within a waveguide experience different effective refractive indices. Upon reaching the output facet of the waveguide, the electro-magnetic waves comprising these modes might be in phase or out of phase depending on signal wavelength and waveguide length, resulting in a fast oscillating amplitude of the output intensity with respect to scanning wavelength. In some cases the effect could be minimized (see Fig. 3.15 b), and in other cases it was not apparent at all (see Fig. 3.16 a), enabling the use of these waveguides for absorption and pumping experiments.

These spectra of transmitted power characterize the wavelength dependent signal loss in the waveguide, including waveguide coupling and propagation loss, absorption by Er^{3+} ion, and absorption by Si-NCs. To extract the absorption of signal power due to Er^{3+} ions from the overall transmitted spectrum, undoped waveguides of type U were used as reference. Since both Er-doped and undoped waveguides exhibit nearly the same losses due to coupling, scattering, and Si-NC absorption, these losses can be corrected for and the remaining Er absorption was determined via

$$\text{in } [\text{dB/cm}]: \quad \alpha\left(\lambda\right) = -\frac{10}{l_{\text{wg}}}\log_{10}\left(\frac{P_D\left(\lambda\right)}{P_U\left(\lambda\right)}\right), \tag{3.2}$$

$$\text{or in } \left[\text{cm}^{-1}\right]: \quad \alpha\left(\lambda\right) = -\frac{1}{l_{\text{wg}}}\ln\left(\frac{P_D\left(\lambda\right)}{P_U\left(\lambda\right)}\right), \tag{3.3}$$

where $P_D\left(\lambda\right)$ and $P_U\left(\lambda\right)$ are the transmitted powers of the Er-doped and undoped waveguides, respectively, at a given wavelength λ, and l_{wg} is the length of the waveguide in cm.
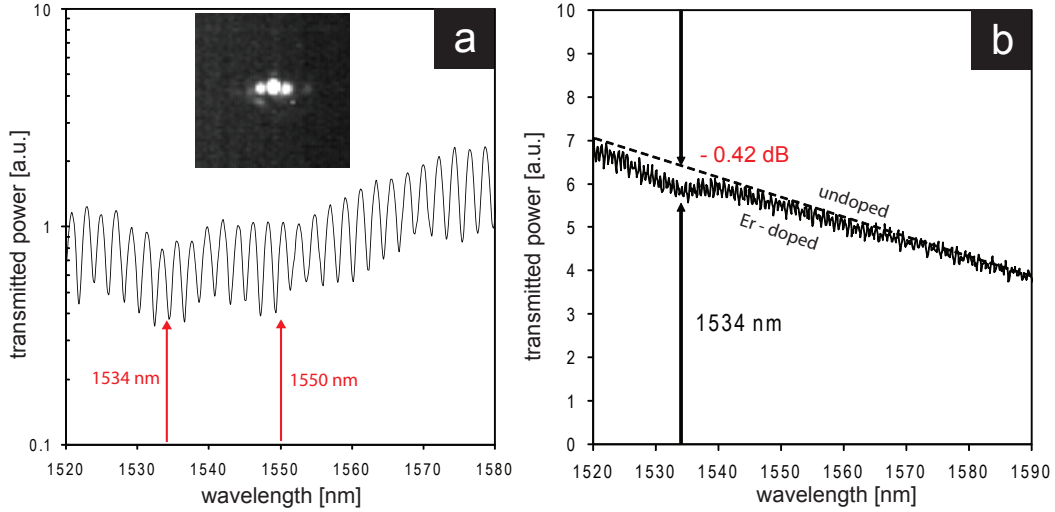
Fig. 3.15: Transmission spectra between $\lambda = 1520 - 1590$ nm of Er-doped optical waveguides. The scan in (a) shows a typical result from a SiO:Er rib-loaded waveguide (core layer height 1 µm) with erbium-related absorption at around 1534 nm and 1550 nm and the periodic oscillations frequently observed. The inset presents an image from the infrared CCD camera showing a higher order mode supported by the same waveguide. Graph (b) shows a scan from a $SiO_{1.7}$:Er waveguide with a shallow absorption peak at 1534 nm due to erbium doping of only 0.12 at.%.

Given the nature of the Er^{3+} energy band described in detail in appendix C, the most pronounced loss in transmitted light is expected for a wavelength of about 1534 nm due to absorption by erbium ions in the ground state. This ground state absorption becomes negligible at wavelengths above about 1580 nm.

An estimate of the peak $^4I_{15/2}$ to $^4I_{13/2}$ absorption cross section can made by using the relation[67,85,118]

$$\sigma_{\rm abs} = \frac{\alpha_{1534}}{\Gamma N_{\rm Er}}, \tag{3.4}$$

where α_{1534} is the Er^{3+} peak absorption at $\lambda = 1534$ nm as compared to an undoped sample, Γ is the core confinement factor (i.e. the overlap of the optical mode with the SiO_x:Er core), and $N_{\rm Er}$ is the erbium concentration in the core material. An estimate on the mode overlap can be made by assessing the mode structures calculated using the mode solving software. The fundamental mode of both channel and rib-loaded waveguides of types C and R-1 was nearly completely ($\Gamma \approx 0.93$) confined to the core layer (see Fig. 3.2 a), due to the core materials refractive index of $n \approx 1.9$. When the refractive index contrast between core and cladding materials is small, a considerable portion of the fundamental mode does not overlap with the core layer. For waveguide R-2, Γ was determined to be 0.64 (see Fig. 3.3 a). The peak absorption of waveguide R-2 with $N_{\rm Er} = 0.72 \times 10^{20}$ cm^{-3} is approximately 0.42 dB on a waveguide length of 0.5 cm (see Fig. 3.15 b), which corresponds to about 0.2 cm^{-1}. Using these values the absorption cross section is estimated to be
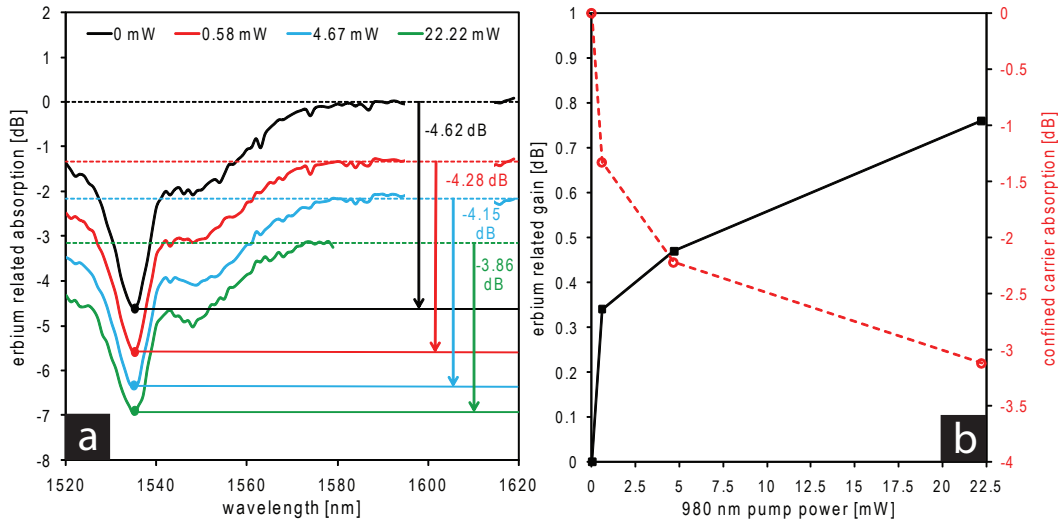
Fig. 3.16: Absorption and emission behavior of a SiO:Er rib-loaded waveguide (rib width: 5 μm, rib height: 0.6 μm) between $\lambda = 1520 - 1620$ nm for increasing pump powers at 0.98 μm . (a) shows transmission spectra (corrected for the system response) for various pump intensities and peak absorption values. (b) illustrates erbium-related gain and confined carrier absorption as a function of pump power.

4.3×10^{-21} cm^2. In case of the heavier doped R-1 waveguide with $N_{Er} = 6 \times 10^{20}$ cm^{-3} the peak absorption is 9.24 dB/cm or 2.13 cm^{-1} (see Fig. 3.16 a), resulting in an estimated absorption cross section of about 3.8×10^{-21} cm^2. These numbers are in good agreement with values for Si-NC and Er-doped glasses reported elsewhere[67,87], and about 1 order of magnitude lower than the cross section reported by Han *et al.*[5]

3.5.4 Pump - probe experiment

In order to raise Er^{3+} ions from the $^4I_{15/2}$ ground state into their excited $^4I_{13/2}$ level, and thereby create the potential for population inversion and stimulated emission, the Er-doped waveguides have to be pumped optically. Population inversion is achieved if at least 50 % of the Er^{3+} ions can be excited. A typical pumping wavelength is 0.98 μm , as photons at this wavelength can excite Er^{3+} ions into their $^4I_{11/2}$ level, from where they quickly relax to the $^4I_{13/2}$ level through phonon-mediated energy exchange.

To estimate the amount of excitable Er^{3+} ions (in relation to all absorbing Er^{3+} ions) and investigate if population inversion can be achieved in SiO$_x$:Er waveguides, optical pumping at 0.98 μm was conducted for increasing pump powers with the setup shown in Fig. 3.11. For each pump intensity, the signal wavelength was scanned through the 1520 nm - 1620 nm band and the transmitted powers were recorded as a function of wavelength. Typical results – corrected for system response and showing the erbium-related changes only – are shown in Fig. 3.16(a).

As pump power was increased, two mechanisms acting simultaneously on the spectral response of the waveguide were observed.

First, the dashed lines in Fig 3.16 (a) correspond to the transmitted power recorded at 1620 nm where the erbium-related absorption is negligibly small. These indicate a broad and featureless loss mechanism. This effect is commonly ascribed to *carrier-induced absorption* – free carrier absorption (FCA) or confined carrier absorption (CCA) – and is well known to be a dominant pump-induced mechanism in Si-NC materials.[25,67,84,119] Light in the signal band near 1534 nm can be absorbed by free carriers, which undergo intraband transitions in the process. Carrier-induced absorption therefore depends on the density of excited carriers, which in turn depends on the pump power as illustrated in Fig. 3.16(b) for a SiO:Er waveguide.

The second observed effect is a reduction in the erbium-related absorption with increasing pump power due to stimulated emission, which is most apparent at 1534 nm. In Fig. 3.16(a), the absorption for each pump power was determined as the intensity ratio between 1534 nm and 1580 nm, as erbium-related absorption at 1580 nm was considered negligible. The change in intensity due to Er^{3+} emission – hereafter referred to as "gain" g_{Er} – may then be determined via

$$g_{Er}\,[dB] = \alpha_{pump}\,[dB] - \alpha_o\,[dB]\,, \qquad (3.5)$$

where α_o is the peak absorption at 1534 nm with zero pump power, and α_{pump} is the peak absorption at the same wavelength under optical pumping. Note that despite using the term 'gain', no net gain (i.e. signal amplification) was actually observed. Rather, the increase in carrier-induced absorption with pump power is the dominant effect. Figure 3.16(b) shows the change in transmitted intensity (i.e. erbium-related gain) with increasing pump power for a SiO:Er waveguide of length $\sim$ 0.5 cm. At maximum pump intensity of 22.2 mW, the erbium-related gain reaches 0.76 dB or 1.52 dB/cm. The percentage of inverted Er^{3+} ions may be estimated by comparing this gain to the peak absorption via[118]

$$\frac{N_{exc}}{N_{Er}} = \frac{g_{Er}}{2 \cdot \alpha_o}. \qquad (3.6)$$

Given the values above, only about 8.2 % of the absorbing Er^{3+} ions were optically active and contributed to signal gain at a pump power of 22.2 mW, most likely due to clustering of the Er^{3+} ions at high doping concentrations.[96,120] The determined value is in good agreement with values reported by Daldosso *et al.*[67]

Attempts were made to non-resonantly excite the erbium ions via sensitization by the Si-NCs as described in section 3.4.2. Neither co-propagating the 532 nm pump light in the waveguide nor pumping from above was successful.

CHAPTER 4

Conclusion

4.1 Summary of Results

Er-doped glasses containing amorphous and crystalline silicon nanoclusters were investigated as a potential medium for integrated optical waveguide amplifiers. Both photoluminescence properties and microfabrication approaches were studied.

4.1.1 Si-NC photoluminescence

Photoluminescence spectra were recorded for various SiO_x compositions ($x = 1 - 1.8$) and annealing temperatures ($T_{anneal} = 400°C - 1100°C$). Due to the NC size distribution, these spectra were typically about 200 nm wide and the peak emission wavelengths ranged from 450 nm to 950 nm depending on the mean nanocluster size. Rise and decay traces obtained from crystalline Si-NCs were well described by a stretched exponential function with $1/e$ lifetimes of $\tau \approx 50$ μs and $\beta \approx 0.7$, whereas the traces obtained from amorphous Si-NCs were characterized by two components. (A fast component and a slow component). Again, the slow component was well described by a stretched exponential with $\beta \approx 0.7$ and a $1/e$ value of $\tau \approx 80$ μs. Using these lifetimes and approximating the silicon nanoclusters as a two level system, the absorption cross section of Si-NCs was estimated to be approximately 10^{-15} cm^2 to 10^{-14} cm^2.

Introduction of Er^{3+} ions into the SiO_x films was found to quench Si-NC photoluminescence and cause a shortening of the Si-NC photoluminescence rise and decay times, both indicative of a fast and efficient transfer of energy from the silicon nanoclusters to the erbium. Quenching was most pronounced at wavelengths corresponding to Er^{3+} excited levels (e.g. $\lambda \approx 660$ nm).

4.1.2   Er^{3+} photoluminescence and effective energy transfer

Amorphous and crystalline silicon nanoclusters have been shown to efficiently sensitize the luminescent transitions in Er^{3+} -doped silicon-rich oxide (SRO). The Er^{3+} ions embedded in the SiO$_x$ matrix were excited via energy transfer from the Si-NCs with wavelengths not resonant to any excited erbium level. The characteristic Er^{3+} emission band around $\lambda = 1.54$ µm - corresponding to the transition between the ^{4}I$_{13/2}$ and ^{4}I$_{15/2}$ erbium levels - was observed for annealing temperatures ranging from 400°C to 1100°C and oxygen-to-silicon ratios between 1 and 1.8 (SiO $\rightarrow$ SiO$_{1.8}$).

Intense Er^{3+} photoluminescence was observed for samples which also exhibited Si-NC photoluminescence at a peak wavelength of $\lambda \approx 660$ nm. This suggests that the energy transfer mechanism is most efficient when the band levels of the Si-NCs overlap with the ^{4}F$_{9/2}$ excited state of the Er^{3+} ions. It is noteworthy that in all these cases the Si-NCs were in an amorphous state, confirming an earlier report[69] stating amorphous Si-NCs as more effective sensitizers than their crystalline counterparts.

Photoluminescence rise and decay traces were recorded for the 1.54 µm emission band and were described by a stretched exponential function with $1/e$ lifetimes in the range of 0.1 ms to 8.8 ms, the latter being close to the lifetimes found in Er-doped silica fibers. The longest lifetimes were observed for films rich in oxygen and annealed at temperatures between 700°C and 900°C . The Er^{3+} excitation cross section was estimated (using the obtained rise and decay times) to be $\sim 10^{-16} - 10^{-15}$ cm^2 by assuming a two-level system at low pump flux. This cross section estimate is $4-5$ orders of magnitude larger than for Er^{3+} ions in silica.[29]

In contrast to Er-doped films containing crystalline Si-NCs, no temperature quenching was observed for films containing amorphous silicon nanoclusters, indicating that back transfer from the Er^{3+} ions to the Si-NCs is minimal in this case. In fact, the PL intensity at 1.54 µm increases with temperature when the nanocluster sensitizers are amorphous.

In conclusion, the obtained results suggest means by which the properties of Si-NC sensitized Er^{3+} ions can be optimized by choosing the appropriate T_{anneal} and oxygen-to-silicon ratio.

4.1.3   SiO$_x$:Er waveguides

Channel- and rib-loaded integrated waveguides have been designed and fabricated using the investigated SiO$_x$:Er films as active core materials. Insertion losses for each waveguide type were determined for a variety of waveguide widths. In the case of the investigated channel waveguides, propagation losses on the order of ~ 2 dB/cm and coupling losses of about 6 dB at a wavelength of $\lambda = 1300$ nm were obtained. For rib-loaded waveguides, propagation losses between 3.2 dB/cm ($\lambda = 1600$ nm) and 14.5 dB/cm ($\lambda = 1300$ nm) were measured. The coupling losses

for this type of waveguide were measured to be ~ 10 dB.

The ${}^4I_{13/2}$ to ${}^4I_{15/2}$ erbium absorption cross section under direct excitation ($\lambda = 0.98$ µm) was estimated to be 4×10^{-21} cm^2, slightly higher than the value reported in SiO$_2$, but much lower than the values determined for Si-NC sensitized excitation in this work ($\sim 10^{-16} - 10^{-15}$ cm^2).

Erbium related signal enhancement in the 1.54 µm emission band was investigated by co-propagating signal and pump light in rib-loaded waveguide with a SiO:Er core layer. Under resonant pumping ($\lambda = 0.98$ µm) it was possible to invert $\sim 8\%$ of the active Er^{3+} ion population and an erbium related signal enhancement of ~ 1.5 dB/cm was observed. However, carrier-induced absorption constitutes a dominant loss mechanism (~ 3 dB/cm) exceeding the signal enhancement.

4.2 Suggested future work

To exploit the potential of Si-NC sensitized Er-doped glasses for optical waveguide amplifiers, several issues (e.g. the invertible fraction of active Er^{3+} ions or the reduction of carrier-induced absorption loss) must be addressed and resolved. In this work, an Er^{3+} doping concentration of ~ 0.2 at.% was used in most SiO$_x$ host compositions. Photoluminescence in the SiO$_x$:Er material system may be further optimized by investigating the effects of different doping levels. SiO$_{1.5}$ is suggested as the host material, since annealing this composition at 700°C created the best conditions for effective energy transfer in this work, paired with long lifetimes of the excited level. This work aims to maximize the fraction of active and invertible Er^{3+} ions. The increased oxygen-to-silicon ratio will result in a smaller number of Si-NC, thereby reducing the losses due to carrier-induced absorption.

Bibliography

[1] G. E. Moore, "Cramming more components onto integrated circuits," *Electronics*, vol. 38, no. 8, pp. 114–117, 1965.

[2] http://www.itrs.net.

[3] E. Suhir, "Microelectronics and photonics - the future," *Microelectronics Journal*, vol. 31, pp. 839–851, 2000.

[4] L. Pavesi and G. Guillot, *Optical Interconnects: the silicon approach*.   Berlin: Springer-Verlag, 2006, ISBN: 3-540-28910-0.

[5] H.-S. Han, S.-Y. Seo, and J. H. Shin, "Optical gain at 1.54 μm in erbium-doped silicon nanocluster sensitized waveguide," *Applied Physics Letters*, vol. 79, no. 27, pp. 4568–4570, 2001.

[6] D. Pacifici, "Erbium doped silicon nanoclusters for Microphotonics," Ph.D. dissertation, University of Catania, Italy, 2003.

[7] L. Pavesi, "Silicon-Based Light Sources for Silicon Iintegrated Circuits," *Advances in Optical Technologies*, vol. 2008, no. 416926, pp. 1–12, 2008.

[8] S. S. Iyer and Y. H. Xie, "Light Emission from Silicon," *Science*, vol. 260, no. 5104, pp. 40–46, 1993.

[9] A. C. Hryciw, "Optical properties of rare-earth doped silicon nanocomposites," Ph.D. dissertation, University of Alberta, Edmonton, Alberta, Canada, 2007.

[10] N. W. Ashcroft and N. D. Mermin, *Solid state physics*.   New York: Holt Rhinehart, 1976, ISBN: 0-03-083993-9.

[11] D. J. Lockwood and L. Pavesi, "Silicon Fundamentals for Photonics Applications," *Topics in Applied Physics*, vol. 94, pp. 1–52, 2004.

[12] U. Gnutzman and K. Clausecker, "Theory of Direct Optical Transitions in an Optical Indirect Semiconductor with a Superlattice Structure," *Applied Physics*, vol. 3, pp. 9–14, 1974.

[13] E. Kasper and F. S. in: R. K. Willardson, A. C. Beer, T. P. Pearsall (Eds.), *Semiconductors and Semimetals, vol.33: Strained-Layer Super-Lattices*.   Boston: Academic Press, 1991, pp. 223, ISBN: 0-12-752133-X.

[14] H. Ennen, G. Pomrenke, A. Axmann, K. Eisele, W. Haydl, and J. Schneider, "1.54-μm electroluminescence of erbium-doped silicon grown by molecular beam epitaxy," *Applied Physics Letters*, vol. 46, no. 4, p. 381, 1985.

[15] L. Canham, K. G. Barraclough, and D. J. Robbins, "1.3-m light-emitting diode from silicon electron irradiated at its damage threshold," *Applied Physics Letters*, vol. 51, no. 19, p. 1509, 1987.

[16] P. L. Bradfield, T. G. Brown, and D. G. Hall, "Electroluminescence from sulfur impurities in a p-n junction formed in epitaxial silicon," *Applied Physics Letters*, vol. 55, no. 2, p. 100, 1989.

[17] D. Weaire, "Existence of a gap in the electronic density of states of a tetrahedrally solid of arbitrary structure," *Phys. Rev. Lett.*, vol. 26, no. 25, pp. 1541–1543, 1971.

[18] M. F. Thorpe and D. Weaire, "Electronic density of states of amorphous Si and Ge," *Phys. Rev. Lett.*, vol. 27, no. 23, pp. 1581–1584, 1971.

[19] J. Wang, X. F. Wang, Q. Li, A. Hryciw, and A. Meldrum, "The microstructure of SiO thin films: from nanoclusters to nanocrystals," *Philosophical Magazine*, vol. 87, no. 1, pp. 11–27, 2007.

[20] G. A. Kachurin, M. O. Ruault, A. K. Gutakovsky, O. Kaitasov, S. G. Yanovskaya, K. S. Zhuravlev, and H. Bernas, "Ligth particle irradiation effects in Si nanocrystals," *Nucl. Instr. Meth. B*, vol. 147, no. 1-4, pp. 356–360, 1999.

[21] L. Canham, "Gaining light from silicon," *Nature*, vol. 408, pp. 411–412, 2000.

[22] L. Pavesi, L. Dal Negro, C. Mazzoleni, G. Franzò, and F. Priolo, "Optical gain in silicon nanocrystals," *Nature*, vol. 408, pp. 440–444, 2000.

[23] A. G. Cullis, L. T. Canham, and P. D. J. Calcott, "The structural and luminescence properties of porous silicon," *Journal of Applied Physics*, vol. 82, no. 3, pp. 909–965, 1997.

[24] A. Hryciw, A. Meldrum, K. S. Buchanan, and C. W. White, "Effects of particle size and excitation spectrum on the photoluminescence of silicon nanocrystals formed by ion implantation," *Nucl. Instr. Meth. B*, vol. 222, no. 3-4, pp. 469–476, 2004.

[25] P. G. Kik and A. Polman, "Gain limiting processes in Er-doped Si nanocrystal waveguides in SiO_2 ," *Journal of Applied Physics*, vol. 91, no. 1, pp. 534–536, 2002.

[26] O. Savchyn, F. R. Ruhge, P. G. Kik, R. M. Todi, K. R. Coffey, H. Nukala, and H. Heinrich, "Luminescence-center-mediated excitation as the dominant Er sensitization mechanism in Er-doped silicon-rich SiO_2 films," *Physical Review B*, vol. 76, no. 195419, pp. 1–10, 2007.

[27] M. Fujii, M. Yoshida, Y. Kanzawa, S. Hayashi, and K. Yamamoto, "1.54 µm photoluminescence of Er^{3+} doped into SiO_2 films containing Si nanocrystals: Evidence for energy transfer from Si nanocrystals to Er^{3+} ," *Applied Physics Letters*, vol. 71, no. 9, pp. 1198–1200, 1997.

[28] F. Gourbilleau, M. Levalois, C. Dufour, J. Vicens, and R. Rizk, "Optimized conditions for an enhanced coupling rate between Er ions and Si nanoclusters for an improved 1.54-µm emission," *Journal of Applied Physics*, vol. 95, no. 7, pp. 3717–3722, 2004.

[29] A. J. Kenyon, C. E. Chryssou, C. W. Pitt, T. Shimizu-Iwayama, D. E. Hole, N. Sharma, and C. J. Humphreys, "Luminescence from erbium-doped silicon nanocrystals in silica: Excitation mechanisms," *Journal of Applied Physics*, vol. 91, no. 1, pp. 367–374, 2002.

[30] G. Franzò, E. Pecora, F. Priolo, and F. Iacona, "Role of the Si excess on the excitation of Er doped SiO_x," *Applied Physics Letters*, vol. 90, no. 183102, pp. 1–3, 2007.

[31] S. W. Roberts, G. J. Parker, and M. Hempstead, "The Photoluminescence of Erbium-doped Silicon Monoxide," *Optical Materials*, vol. 6, pp. 99–102, 1996.

[32] A. Meldrum, A. Hryciw, A. N. MacDonald, C. Blois, K. Marsh, J. Wang, and Q. Li, "Photoluminescence in the silicon-oxygen system," *Journal of Vacuum Science and Technology A*, vol. 24, no. 3, pp. 713–717, 2006.

[33] L. T. Canham, "Silicon quantum wire array fabrication by electrochemical and chemical dissolution of wafers," *Applied Physics Letters*, vol. 57, no. 10, pp. 1046–1048, 1990.

[34] Y. Kanemitsu, "Efficient light emission from crystalline and amorphous silicon nanostructures," *Journal of Luminescence*, vol. 100, pp. 209–217, 2002.

[35] D. Kovalev, H. Heckler, G. Polisski, and F. Koch, "Optical properties of Si nanocrystals," *Physica Status Solidi B*, vol. 215, no. 2, pp. 871–932, 1999.

[36] S. V. Gaponenko, Ed., *Optical Properties of Semiconductor Nanocrystals*. Cambridge, UK: Cambridge University Press, 1998, ISBN: 0-521-58241-5.

[37] V. A. Belyakov, V. A. Burdov, R. Lockwood, and A. Meldrum, "Silicon Nanocrystals: Fundamental Theory and Implications for Stimulated Emission," *Advances in Optical Technologies*, vol. 2008, no. 279502, pp. 1–32, 2008.

[38] A. Meldrum, R. Lockwood, V. A. Belyakov, and V. A. Burdov, "Computational simulations for ensembles of luminescent silicon nanocrystals: Implications for optical gain and stimulated emission," *Physica E*, vol. 41, pp. 955–958, 2009.

[39] M. V. Wolkin, J. Jorne, P. M. Fauchet, G. Allan, and C. Delerue, "Electronic States and Luminescence in Porous Quantum Dots: The Role of Oxygen," *Physical Review Letters*, vol. 82, no. 1, pp. 197–200, 1999.

[40] E. Luppi, F. Iori, R. Magri, O. Pulci, S. Ossicini, E. Degoli, and V. Olevano, "Excitons in silicon nanocrystallites: The nature of luminescence," *Physical Review B*, vol. 75, no. 3, p. 033303, 2007.

[41] N. Daldosso, M. Luppi, S. Ossicini, E. Degoli, R. Magri, G. Dalba, P. Fornasini, R. G. F. Rocca, L. Pavesi, S. Boninelli, F. Priolo, C. Spinella, and F. Iacona, "Role of the interface region on the optoelectronic properties of silicon nanocrystals embedded in SiO_2 ," *Physical Review B*, vol. 68, no. 8, p. 085327, 2003.

[42] G. Hadjisavvas and P. Kelires, "Theory of interface structure, energetics, and electronic properties of embedded Si/a-SiO_2 nanocrystals," *Physica E*, vol. 38, no. 1-2, pp. 99–105, 2007.

[43] A. Saar, Y. Reichman, M. Dovrat, D. Krapf, J. Jedrzejewski, and I. Balberg, "Resonant Coupling between Surface Vibrations and Electronic States in Silicon Nanocrystals at the Strong Confinement Regime," *Nanoletters*, vol. 5, no. 12, pp. 2443–2447, 2005.

[44] T. Shimizu-Iwayama, D. E. Hole, and P. D. Townsend, "Excess Si concentration dependence of the photoluminescence of Si nanoclusters in SiO_2 fabricated by ion implantation," *Journal of Luminescence*, vol. 80, no. 1-4, pp. 235–239, 1998.

[45] S. Ossicini, C. M. Bertoni, M. Biagini, A. Lugli, G. Roma, and O. Bisi, "Optical properties of isolated and interacting silicon quantum wires," *Thin Solid Films*, vol. 297, no. 1-2, pp. 154–162, 1997.

[46] J. Heitmann, F. Müller, M. Zacharias, and U. Gösele, "Silicon Nanocrystals: Size Matters," *Advanced Materials*, vol. 17, no. 7, pp. 795–803, 2005.

[47] H. Rinnert, M. Vergnat, and A. Burneau, "Evidence of light-emitting amorphous silicon clusters confined in a silicon oxide matrix," *Journal of Applied Physics*, vol. 89, no. 1, pp. 237–243, 2001.

[48] X. D. Pi, O. H. Y. Zalloum, T. Roschuk, J. Wojcik, A. P. Knights, P. Mascher, and P. J. Simpson, "Light emission from Si nanoclusters formed at low temperatures," *Applied Physics Letters*, vol. 88, no. 103111, pp. 1–3, 2006.

[49] R. B. Wehrspohn, J. N. Chazalviel, F. Ozanam, and I. Solomon, "Spatial versus quantum confinement in porous amorphous silicon nanostructures," *Eur. Phys. J. B*, vol. 8, no. 2, pp. 179–193, 1999.

[50] M. J. Estes and G. Moddel, "Luminescence from amorphous silicon nanostructures," *Physical Review B*, vol. 54, no. 20, pp. 14 633–14 642, 1996.

[51] G. H. Dieke, *Spectra and energy levels of rare earth ions in crystals*. California: Interscience Publisher, 1968, ISBN: 0-470-21390-6.

[52] A. J. Kenyon, "Recent developments in rare-earth doped materials for optoelectronics," *Progress in Quantum Electronics*, vol. 26, pp. 225–284, 2002.

[53] A. Kenyon, "Erbium in silicon," *Semicond. Sci. Technol.*, vol. 20, pp. R65–R84, 2005.

[54] S. Sudo, Ed., *Optical Fiber Amplifiers: Materials, Devices, and Applications*. Norwood, MA: Artech House, Inc., 1997, ISBN: 0-89006-809-7.

[55] G. Franzò, V. Vinciguerra, and F. Priolo, "The excitation mechanism of rare-earth ions in silicon nanocrystals," *Applied Physics A*, vol. 69, pp. 3–12, 1999.

[56] J. S. Chang, J.-H. Jhe, M.-S. Yang, K. J. Kim, D. W. Moon, and J. H. Shin, "Effects of silicon nanostructure evolution on Er^{3+} luminescence in silicon-rich silicon oxide/Er-doped silica multilayers," *Applied Physics Letters*, vol. 89, no. 181909, pp. 1–3, 2006.

[57] K. Imakita, M. Fujii, Y. Yamaguchi, and S. Hayashi, "Interaction between Er ions and shallow impurities in Si nanocrystals within SiO_2," *Physical Review B*, vol. 71, p. 115440, 2005.

[58] J. S. Ha, C. H. Bae, S. H. Nam, S. M. Park, Y. R. Jang, K. H. Yoo, and K. Park, "Er^{3+} photoluminescence from Er-doped amorphous SiO_x films prepared by pulsed laser deposition at room temperature: The effects of oxygen concentration," *Applied Physics Letters*, vol. 82, no. 20, pp. 3436–3438, 2003.

[59] P. G. Kik, M. L. Brongersma, and A. Polman, "Strong exciton-erbium coupling in Si nanocrystal-doped SiO_2 ," *Applied Physics Letters*, vol. 76, no. 17, pp. 2325–2327, 2000.

[60] P. G. Kik and A. Polman, "Exciton-erbium interaction in Si nanocrystal-doped SiO_2 ," *Journal of Applied Physics*, vol. 88, no. 4, pp. 1992–1998, 2000.

[61] M. Falconieri, E. Borsella, L. De Dominicis, F. Enrichi, G. Franzò, F. Priolo, F. Iacona, F. Gourbilleau, and R. Rizk, "Probe of the Si nanoclusters to Er^{3+} energy transfer dynamics by double-pulse excitation," *Applied Physics Letters*, vol. 87, no. 061109, pp. 1–3, 2005.

[62] M. Fujii, K. Imakita, K. Watanabe, and S. Hayashi, "Coexistence of two different energy transfer processes in SiO_2 films containing Si nanocrystals and Er," *Journal of Applied Physics*, vol. 95, no. 1, pp. 272–280, 2004.

[63] J.-H. Jhe, J. H. Shin, K. J. Kim, and D. W. Moon, "The characteristic carrier-Er interaction distance in Er-doped a-Si/SiO_2 superlattices formed by ion sputtering," *Applied Physics Letters*, vol. 82, no. 25, pp. 4489–4491, 2003.

[64] T. Kimura, H. Isshiki, S. Ide, T. Shimizu, T. Ishida, and R. Saito, "Suppression of Auger deexcitation and temperature quenching of the Er-related 1.54 µm emission with an ultrathin oxide interlayer in an Er/SiO_2 /Si structure," *Journal of Applied Physics*, vol. 93, no. 5, pp. 2595–2601, 2003.

[65] F. Gourbilleau, C. Dufour, R. Madelon, and R. Rizk, "Effects of Si nanocluster size and carrier-Er interaction distance on the efficiency of energy transfer," *Journal of Luminescence*, vol. 126, pp. 581–589, 2007.

[66] H. Lee, J. H. Shin, and N. Park, "Performance analysis of nanocluster-Si sensitized Er-doped waveguide amplifier using top-pumped 470nm LED," *Optics Express*, vol. 13, no. 24, pp. 9881–9889, 2005.

[67] N. Daldosso, D. Navarro-Urrios, M. Melchiorri, L. Pavesi, F. Gourbilleau, M. Carrada, R. Rizk, C. Garcia, P. Pellegrino, B. Garrido, and L. Cognolato, "Absorption cross section and signal enhancement in Er-doped Si nanocluster rib-loaded waveguides," *Applied Physics Letters*, vol. 86, no. 261103, pp. 1–3, 2005.

[68] P. Pellegrino, B. Garrido, J. Arbiol, C. Garcia, Y. Lebour, and J. R. Morante, "Site of Er ions in silica layers codoped with Si nanoclusters and Er," *Applied Physics Letters*, vol. 88, no. 121915, pp. 1–3, 2006.

[69] G. Franzò, S. Boninelli, D. Pacifici, F. Priolo, F. Iacona, and C. Bongiorno, "Sensitizing properties of amorphous Si clusters on the 1.54-μm luminescence of Er in Si-rich SiO$_2$," *Applied Physics Letters*, vol. 82, no. 22, pp. 3871–3873, 2003.

[70] F. Auzel, "Up-conversion in RE-doped solids," in *Spectroscopic properties of rare earths in optical materials*, G. Liu and B. Jacquier (Eds.). Berlin: Springer-Verlag, 2005, pp. 265-319, ISBN: 3-540-23886-7.

[71] T. Förster, "Zwischenmolekulare Energiewanderung und Fluoreszenz," *Annalen der Physik*, vol. 2, no. 1-2, pp. 55–75, 1948.

[72] D. L. Dexter, "A theory of sensitized luminescence in solids," *J. Chem. Phys.*, vol. 21, no. 5, pp. 836–850, 1953.

[73] T. Miyakawa and D. L. Dexter, "Phonon sidebands, multiphonon relaxation of excited states, and phonon-assisted energy transfer between ions in solids," *Physical Review B*, vol. 1, no. 7, pp. 2961–2969, 1970.

[74] N. L. Vekshin, Ed., *Energy transfer in macromolecules*. Bellingham, WA: SPIE Optical Engineering Press, 1997, ISBN: 0-8194-2081-6.

[75] R. Lockwood, A. Hryciw, and A. Meldrum, "Nonresonant carrier tunneling in arrays of silicon nanocrystals," *Applied Physics Letters*, vol. 89, no. 263112, pp. 1–3, 2006.

[76] P. G. Kik and A. Polman, "Erbium doped optical waveguide amplfiers on silicon," *MRS Bulletin*, vol. 23, no. 4, 1998.

[77] W. H. Loh and A. J. Kenyon, "Excited State absorption in the Si Nanocluster-Er Material System," *IEEE Photonics Technology Letters*, vol. 18, no. 1, pp. 289–291, 2006.

[78] C. J. Oton, W. H. Loh, and A. J. Kenyon, "Er^{3+} excited state absorption and the low fraction of nanocluster-excitable Er^{3+} in SiO$_x$," *Applied Physics Letters*, vol. 89, no. 031116, pp. 1–3, 2006.

[79] C. E. Chryssou, A. J. Kenyon, and C. W. Pitt, "Investigation of energy exchange between silicon nanocrystals and Er^{3+} in silica," *Materials Science & Engineering B*, vol. 81, pp. 16–18, 2001.

[80] K. Choy, F. Lenz, X. X. Liang, F. Marsiglio, and A. Meldrum, "Geometrical effects in the energy transfer mechanism for silicon nanocrystals and Er^{3+} ," *Appl. Phys. Lett.*, vol. 93, no. 261109, pp. 1–3, 2008.

[81] B. Garrido, C. Garcia, P. Pellegrino, D. Navarro-Urrios, N. Daldosso, L. Pavesi, F. Gourbilleau, and R. Rizk, "Distance dependent interaction as the limiting factor for Si nanocluster to Er energy transfer in silica," *Applied Physics Letters*, vol. 89, no. 163103, pp. 1–3, 2006.

[82] K. Imakita, M. Fujii, and S. Hayashi, "Spectrally resolved energy transfer from excitons in Si nanocrystals to Er ions," *Physical Review B*, vol. 71, no. 193301, pp. 1–4, 2005.

[83] K. Watanabe, M. Fujii, and S. Hayashi, "Resonant excitation of Er^{3+} by the energy transfer from Si nanocrystals," *Journal of Applied Physics*, vol. 90, no. 9, pp. 4761–4767, 2001.

[84] D. Pacifici, G. Franzò, F. Priolo, F. Iacona, and L. Dal Negro, "Modeling and perspectives of the Si nanocrystals-Er interaction for optical amplification," *Physical Review B*, vol. 67, no. 245301, pp. 1–13, 2003.

[85] H.-S. Han, S.-Y. Seo, J. H. Shin, and N. Park, "Coefficient determination related to optical gain in erbium-doped silicon-rich silicon oxide waveguide amplifier," *Applied Physics Letters*, vol. 81, no. 20, pp. 3720–3722, 2002.

[86] P. Pellegrino, B. Garrido, C. Garcia, J. Arbiol, J. R. Morante, M. Melchiorri, N. Daldosso, L. Pavesi, E. Scheid, and G. Sarrabayrouse, "Low-loss rib waveguides containing Si nanocrystals embedded in SiO_2 ," *Journal of Applied Physics*, vol. 97, no. 074312, pp. 1–8, 2005.

[87] H. Mertens, A. Polman, I. M. P. Aarts, W. M. M. Kessels, and M. C. M. van de Sanden, "Absence of the enhanced intra-4f transition cross section at 1.5 μm of Er^{3+} in Si-rich SiO_2," *Applied Physics Letters*, vol. 86, no. 241109, pp. 1–3, 2005.

[88] F. Iacona, C. Bongiorno, C. Spinella, S. Boninelli, and F. Priolo, "Formation and evolution of luminescent Si nanoclusters produced by thermal annealing of SiO_x films," *Journal of Applied Physics*, vol. 95, no. 7, pp. 3723–3732, 2004.

[89] C.-C. Kao, C. Barthou, B. Gallas, S. Fisson, G. Vuye, J. Rivory, A. Al Choueiry, A.-M. Jurdyc, B. Jacquier, and L. Bigot, "Correlation between Si-related and erbium photoluminescence bands and determination of erbium effective excitation cross section in SiO_2 films," *Journal of Applied Physics*, vol. 98, no. 013544, pp. 1–5, 2005.

[90] L.-F. Bian, C. G. Zhang, W. D. Chen, C. C. Hsu, and T. Shi, "Local environment of Er^{3+} in Er-doped Si nanoclusters embedded in SiO_2 films," *Applied Physics Letters*, vol. 89, no. 231927, pp. 1–3, 2006.

[91] Y. C. Fang, W. Q. Li, L. J. Qi, L. Y. Li, Y. Y. Zhao, Z. J. Zhang, and M. Lu, "Photoluminescence from SiO_x thin films: effects of film thickness and annealing temperature," *Nanotechnology*, vol. 15, pp. 494–500, 2004.

[92] D. Nesheva, C. Raptis, A. Perakis, I. Bineva, Z. Aneva, Z. Levi, S. Alexandrova, and H. Hofmeister, "Raman scattering and photoluminescence from Si nanoparticles in annealed SiO_x thin films," *Journal of Applied Physics*, vol. 92, no. 8, pp. 4678–4683, 2002.

[93] J. F. O'Hanlon, *A user's guide to vacuum technology*. Hoboken, New Jersey: John Wiley and Sons, Inc., 2003, ISBN: 0-471-27052-0.

[94] J. A. Moreno, B. Garrido, P. Pellegrino, C. Garcia, J. Arbiol, J. R. Morante, P. Marie, F. Gourbilleau, and R. Rizk, "Size dependence of refractive index of Si nanoclusters embedded in SiO_2," *Journal of Applied Physics*, vol. 98, no. 013523, pp. 1–4, 2005.

[95] A. Hryciw, C. Blois, A. Meldrum, T. Clement, R. DeCorby, and Q. Li, "Photoluminescence from Er-doped silicon oxide microcavities," *Optical Materials*, vol. 28, pp. 873–878, 2006.

[96] A. Polman, "Erbium implanted thin film photonic materials," *Journal of Applied Physics*, vol. 82, no. 1, pp. 1–39, 1997.

[97] E. Neufeld, S. Wang, R. Apetz, C. Buchal, R. Carius, C. W. White, and D. K. Thomas, "Effect of annealing and H_2 passivation on the photoluminescence of Si nanocrystals in SiO_2 ," *Thin Solid Films*, no. 294, pp. 238–241, 1997.

[98] S. P. Withrow, C. W. White, A. Meldrum, J. D. Budai, D. M. Hembree, and J. C. Barbour, "Effects of hydrogen in the annealing environment on photoluminescence from Si nanoparticles in SiO_2," *Journal of Applied Physics*, vol. 86, no. 1, pp. 396–401, 1999.

[99] L. Pavesi, "Routes toward silicon-based lasers," *Materials Today*, pp. 18–25, 2005.

[100] H. Yorikawa and S. Muramatsu, "Logarithmic normal distribution of particle size from luminescence line-shape analysis in porous silicon," *Appl. Phys. Lett.*, vol. 71, no. 5, pp. 644–646, 1997.

[101] J. Söderlund, L. B. Kiss, G. A. Niklasson, and C. G. Granqvist, "Lognormal size distributions in particle growth processes without coagulation," *Phys. Rev. Lett.*, vol. 80, no. 11, pp. 2386–2388, 1998.

[102] P. Li, X. Wang, M. Malac, R. Egerton, A. Meldrum, X. Liang, F. Lenz, and J. Wang, "3D Imaging of Si and Er Nanoclusters in Er Doped $SiO_{1.5}$ Films by STEM Tomography," *submitted*, 2009.

[103] Z. Ma, X. Liao, J. He, W. Cheng, G. Yue, Y. Wang, and G. Kong, "Annealing behaviors of photoluminescence from SiO_x:H," *Journal of Applied Physics*, vol. 83, no. 12, pp. 7934–7939, 1998.

[104] F. Iacona, G. Franzo, and C. Spinella, "Correlation between luminescence and structural properties of Si nanocrystals," *Journal of Applied Physics*, vol. 87, no. 3, pp. 1295–1303, 2000.

[105] L. Pavesi and M. Ceschini, "Stretched-exponential decay of the luminescence in porous silicon," *Phys. Rev. B*, vol. 48, no. 23, pp. 17 625–17 628, 1993.

[106] L. Dal Negro, M. Cazzanelli, L. Pavesi, S. Ossicini, D. Pacifici, G. Franzo, F. Priolo, and F. Iacona, "Dynamics of stimulated emission in silicon nanocrystals," *Applied Physics Letters*, vol. 82, no. 26, pp. 4636–4638, 2003.

[107] O. Guillois, N. Herlin-Boime, C. Reynaud, G. Ledoux, and F. Huisken, "Photoluminescence decay dynamics of noninteracting silicon nanocrystals," *Journal of Applied Physics*, vol. 95, no. 7, pp. 3677–3682, 2004.

[108] Y. Kanemitsu, Y. Fukunishi, and T. Kushida, "Decay dynamics of visible luminescence in amorphous silicon nanoparticles," *Applied Physics Letters*, vol. 77, no. 2, pp. 211–213, 2000.

[109] C. Garcia, B. Garrido, P. Pellegrino, R. Ferre, J. A. Moreno, J. R. Morante, L. Pavesi, and M. Cazzanelli, "Size dependence of lifetime and absorption cross section of Si nanocrystals embedded in SiO_2," *Applied Physics Letters*, vol. 82, no. 10, pp. 1595–1597, 2003.

[110] P. G. Kik and A. Polman, "Towards an Er-doped Si nanocrystal sensitized waveguide laser - the thin line between gain and loss," in *Towards the first silicon laser*, L. Pavesi, S. Gaponenko, and L. Dal Negro (Eds.), vol. 93 of *NATO Science Series II*. Norwell, MA: Kluwer Academic Publishers, 2003, pp. 383-400, ISBN: 1-402-01193-8.

[111] W. J. Miniscalco, "Erbium-Doped Glasses for Fiber Amplifiers at 1500 nm," *Journal of Lightwave Technology*, vol. 9, no. 2, pp. 234–250, 1991.

[112] M. Fujii, M. Yoshida, S. Hayashi, and K. Yamamoto, "Photoluminescence from SiO_2 films containing si nanocrystals and Er: Effects of nanocrystalline size on the photoluminescence efficiency of Er^{3+}," *Journal of Applied Physics*, vol. 84, no. 8, pp. 4525–4531, 1998.

[113] S. Lüttjohann, C. Meier, M. Offer, A. Lorke, and H. Wiggers, "Temperature-induced crossover between bright and dark exciton emission in silicon nanoparticles," *EPL*, vol. 79, no. 37002, pp. 1–5, 2007.

[114] T. J. Clement, "Studies on the Potential for Optical Amplification in Erbium-doped Silicon Monoxide," MSc thesis, University of Alberta, Edmonton, Alberta, Canada, 2006.

[115] K. Robbie and M. J. Brett, "Sculptured thin films and glancing angle deposition: Growth mechanics and applications," *J. Vac. Sci. Technol. A*, vol. 15, no. 3, pp. 1460–1465, 1997.

[116] H. Nishihara, M. Haruna, and T. Suhara, *Optical Integrated Circuits*. New York: McGraw-Hill Professional, 1989, pp. 240, ISBN: 0-07-046092-2.

[117] R. Hui and M. O'Sullivan, *Fiber Optic Measurement Techniques*. San Diego: Elsevier Academic Press, 2008, pp. 382, ISBN: 0-12-373865-2.

[118] T. J. Clement, R. G. DeCorby, N. Ponnampalam, T. W. Allen, A. Hryciw, and A. Meldrum, "Nanocluster sensitized erbium-doped silicon monoxide waveguides," *Optics Express*, vol. 14, no. 25, pp. 12 151–12 162, 2006.

[119] M. Forcales, N. J. Smith, and R. G. Elliman, "Pump-probe experiments at 1.54 µm on silicon-rich silicon oxide waveguides," *Journal of Applied Physics*, vol. 100, no. 014902, pp. 1–3, 2006.

[120] M. J. F. Digonnet (Editor), *Rare-earth-doped Fiber Lasers and Amplifiers*. New York: CRC Press, 2001, ISBN: 0-8247-0458-4.

[121] J. A. Woollam, B. D. Johs, C. M. Herzinger, J. N. Hilfiker, R. A. Synowicki, and C. L. Bungay, "Overview of variable-angle spectroscopic ellipsometry (VASE), part i: Basic theory and typical applications," *Optical Metrology*, vol. CR72, pp. 3–28, 1999.

APPENDIX **A**

Ellipsometry

Ellipsometry is a valuable tool primarily in determining film thickness and optical constants non-destructively; its sensitivity allows it to obtain optical properties of nanometer-scale material film layers. This measurement technique utilizes a change in polarization as light reflects or transmits from a material structure; the measured response depends on optical properties and thickness of the individual film. Besides its most common use to determine film thickness and refractive index, it is also applied to characterize composition, crystallinity, roughness, doping concentration, and other material properties associated with a change in optical response.

A.1   Principle of operation

As ellipsometry is based on a change in the polarization of reflected light it may be useful to give a short overview on light polarization at this point. Light can be described as an electromagnetic wave traveling through space; polarization represents the behavior of the electric field in space and time. Since the electric field of a wave is always perpendicular to the direction in which the wave travels (commonly labeled z), its polarization can be described by its x- and y- components. In cases where the x- and y- wave components are in-phase, the resulting light will be polarized *linearly* as shown in Fig. A.1 (a), whereby the relative amplitudes determine the orientation of the polarization. If the y- component is exactly 90 ° phase-shifted to the x- component, but both wave components have equal amplitudes, resulting light will be *circular* polarized as illustrated in Fig. A.1 (b). Linear and circular polarization represent special cases; most commonly the x- and y- components of a light wave will have arbitrary amplitudes and phase relative to each other, the resulting polarization is *elliptical* as shown in Fig. A.1 (c).
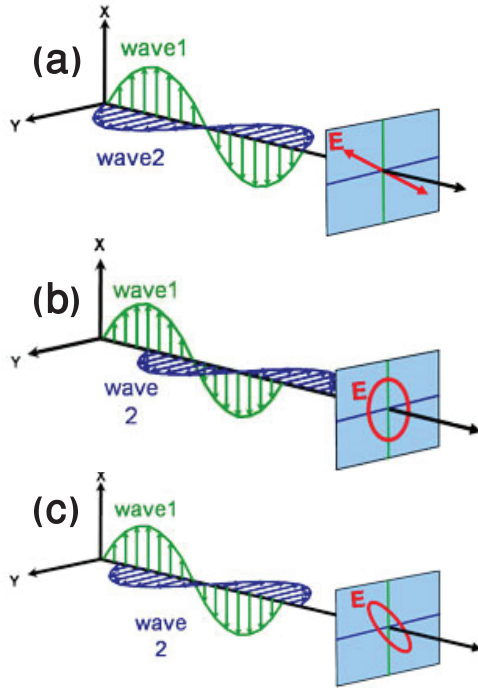
Fig. A.1: Combination of orthogonal waves to demonstrate different polarization: (a) linear polarization; (b) circular polarization; and (c) elliptical polarization.

When light is incident on a material or propagates inside a material, interaction occur between the light and the material. These optical interaction properties can be described in part by the complex refractive index $\hat{n} = n + ik$, consisting of the index n and the extinction coefficient k. The index n describes the phase velocity of light traveling inside a material compared to the speed of light in vacuum, whereas the extinction coefficient k describes the loss of the light waves energy to the material due to absorption. Maxwell's equations must remain satisfied when light interacts with a material, which leads to boundary conditions at the interface; i.e. incident light is reflected and/or refracted at a material interface, depending on the materials optical constants. But, these boundary conditions provide different solutions for electric field polarizations parallel (p) and perpendicular (s) to the plane of incidence, respectively. The amount of light reflected and transmitted at any given interface between two materials in term of the $p-$ and $s-$components are given by Fresnel's equations:

$$r_s = \frac{n_i\cos(\theta_i) - n_t\cos(\theta_t)}{n_i\cos(\theta_i) + n_t\cos(\theta_t)}; \quad t_s = \frac{2n_i\cos(\theta_i)}{n_i\cos(\theta_i) + n_t\cos(\theta_t)} \tag{A.1}$$

$$r_p = \frac{n_t\cos(\theta_i) - n_i\cos(\theta_t)}{n_i\cos(\theta_t) + n_t\cos(\theta_i)}; \quad t_p = \frac{2n_i\cos(\theta_i)}{n_i\cos(\theta_t) + n_t\cos(\theta_i)} \tag{A.2}$$
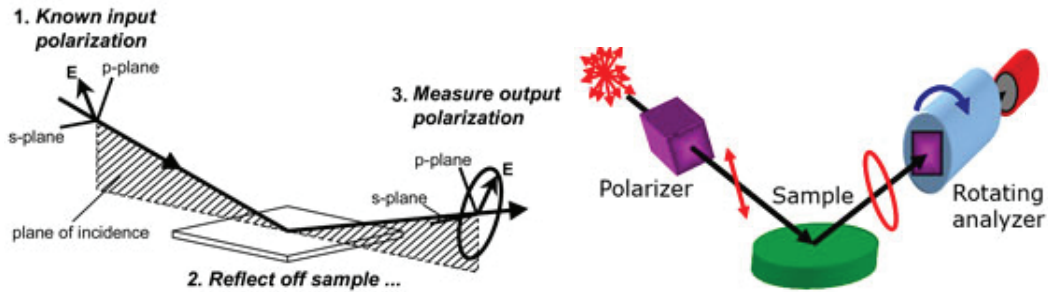
Fig. A.2: Typical ellipsometry configuration: By a polarizer linearly polarized light is reflected from a sample surface and the change in polarization is measured by a rotating analyzer to determine the sample response. After [121].

where i and t represent incident and transmitted light, respectively, and θ denotes the angle relative to the surface normal.

In ellipsometry, measuring the change of $p-$ and $s-$components upon reflection or transmission is of primary interest. To do so, a reference beam with known polarization is reflected of the sample and the resulting output polarization is measured; the change in polarization is represented as an amplitude ratio ψ, and the phase difference Δ, and commonly written as

$$\rho = \tan(\psi)e^{i\Delta}. \tag{A.3}$$

Incident light is linear with both, $p-$ and $s-$components; reflected light has undergone changes of amplitude and phase for both polarizations. A common ellipsometry setup is shown in Fig. A.2 and consists of five basic parts: a light source, a polarization generator, the sample itself, a polarization analyzer, and the detector. For this work a so-called *rotating analyzer ellipsometer* (RAE) was used as also shown in Fig. A.2.

A.2 Measurements

The polarizer axis is oriented between the $p-$ and $s-$ planes to ensure both polarizations are incident on the sample. Upon reflection from the sample the light is elliptical polarized and detected after traveling through a continuously rotating polarizer. ψ and Δ are then determined by comparison with the known input polarization. Typically, regression analysis is used to derive the desired material properties, such as layer thickness and refractive index, from the polarization data measured. After the sample (ψ and Δ) is measured, a model is constructed to describe the sample in terms of the predicted response from Fresnel's equations.

Software compares the calculated values of ψ and Δ for estimated starting values of thickness and/or refractive index and improves the match between experiment and calculation typically via a regression technique.

Film thickness is determined through interference between light reflected at the top surface and light reflected at the bottom surface, the latter traveling through the film twice (i.e. four times, six times, and so on for multiple reflections between bottom and top surface), resulting in constructive or destructive interference depending on the relative phase. Ellipsometry is suitable to measure the thickness of material layers ranging from nanometers to a few micrometers, but with films thicker than several tens of microns, resolution of interference oscillations becomes a limiting factor [121]. Ellipsometry cannot measure the thickness of a material layer independent of its optical constants, since the material index affects light velocity and refracted angle, thereby changing the path length of reflected light traveling through the film. Both n and κ need to be determined along with the layer thickness to ensure correct results. Optical constants are wavelength dependent, but a dispersion relationship can be used to describe the wavelength dependance. The adjustable parameters of this dispersion relationship ease matching of the measured results at various wavelength to an overall optical constant shape. The Cauchy dispersion relationship for the index n is often used in case of transparent materials; it is typically given as

$$n\left(\lambda\right) = A + \frac{B}{\lambda^2} + \frac{C}{\lambda^4} \tag{A.4}$$

where the three terms are adjusted to match the refractive index of the material.

In this work, the deposited sample dummies (film on silicon substrate) where measured in a VASE ellipsometer at two different incident angles, 50° and 60° towards the surface normal. Typically, the wavelength range from 500 nm to 1700 nm was scanned and measured, excluding the region of OH^- absorption between 1350 and 1450 nm. The model used for regression consisted of a Cauchy layer on top of a thick silicon substrate, starting values for thickness and refractive index were estimated from deposition data; i.e. from deposition rates and composition. The obtained refractive index results are very consistent for various samples and are presented in chapter 3 of this thesis. Measured film thicknesses corresponded well to those obtained by a physical measurement via a stylus instrument (profilometer).

APPENDIX **B**

Determination of laser beam profile and area

In general, even two lasers of the same model and type will not have the same beam characteristics, such as beam area or threshold current. Insertion of various optical components (e.g. lenses and mirrors) into our setup will furthermore change and possibly distort the beam profile and spot. To be able to compare the effects of laser irradiation on a sample photon flux values are commonly used. The photon flux, ϕ, irradiant on a surface is defined as

$$\phi = \frac{P}{A} \times \frac{\lambda}{hc},$$ (B.1)

where P is the laser power at the sample, A is the area irradiated, λ is the laser wavelength, h is Planck's constant, and c is the speed of light.

The laser power hitting the sample was readily measured with a silicon photodiode detector, but no instrument was available to determine the area of the laser beam at the location of the sample. Measurement of the beam profile and subsequent derivation of the beam area was implemented as illustrated in Fig. B.1. A detector with silicon photodiode was covered by a horizontal slit and placed at the exact position of the samples, aligned to the center of the beam. The slit width was 5 µm and therefore much smaller than the beam diameter of approximately 0.5 mm, whereas the length of the slit was long enough to allow the hole beam through the slit in that dimension. By moving the slit as shown in the inset of Fig. B.1 from point 0 (whole slit outside the beam area) horizontally towards the beam, an intensity curve can be recorded. Circles and dashed curve in Fig. B.1 show the behavior of the integrated intensity while moving the slit from point 0 to point x (full beam diameter within the slit). The beam intensity profile can then be derived by differentiation of the integrated intensity and results in a gaussian intensity profile also shown in Fig. B.1 as squares and solid curve after normalization to the maximum value. By definition, the diameter of a laser beam is measured at
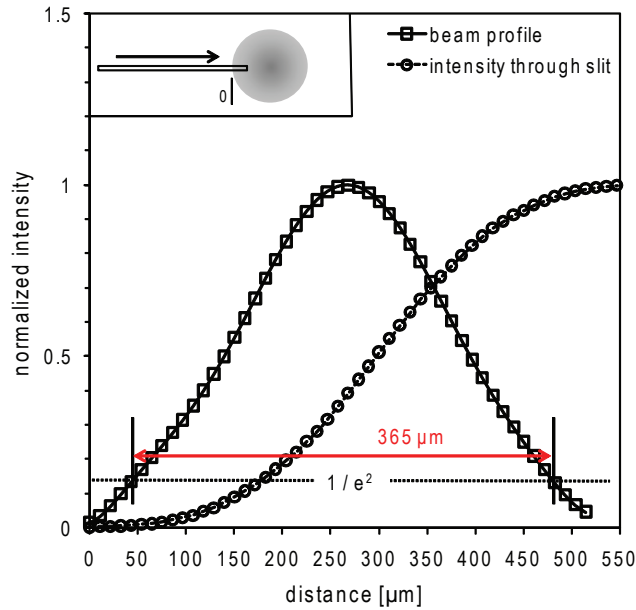
Fig. B.1: Derivation of laser beam profile and spot size.

the points at which the electric field has decreased to the $1/e$ value of the peak amplitude, or analogous where the intensity has decreased to the $1/e^2 = 0.1353$ of the peak value. Using this definition the beam radius was determined to be r = 182.5 µm . In order to avoid collection of laser pump light during photoluminescence measurements, the samples where turned by 45 ° away from the incident beam, distorting the circular beam profile into an ellipse. The minor axis of this ellipse is still r = 182.5 µm , whereas the major axis is now s = $\sqrt{2}$· 182.5 µm = 258.2 µm . Finally, the area enclosed by this ellipse is calculated as A = πrs = 0.00148 cm^2; the latter beam area was used to determine all pump power density in the saturation measurements of chapter 2.

APPENDIX C

Erbium transition band fitting

In the course of investigating the effect of sample temperature on the Er^{3+} emission spectrum, energy levels within the $^4I_{13/2}$ and $^4I_{15/2}$ level manifolds were determined via fitting the the overall spectrum with gaussian curves of the form

$$I(\lambda) = I_0 \cdot \exp^{-\frac{(\lambda - \lambda_0)^2}{2c^2}},$$

where I_0 is the peak intensity at the peak wavelength λ_0, and c is a measure of the broadening (i.e. the peak width).

Each Gaussian curve represents a radiative transition between a level of the upper manifold and a level of the ground state manifold. Since all in all 56 transitions are theoretically possible (i.e. 8×7, from each of the 7 upper split levels to each of the 8 lower split levels), a high number of fitting parameters is given. Therefore, manual fitting (using Fityk 0.8.6) was required to obtain meaningful results. A spectra obtained for a sample cooled to 77 K (see Fig. 1.8) was used for the fit, taking advantage of the more distinct features of the primary and secondary peaks as well as the 'tail' features in this case.

First, a gaussian curve was fit to the primary peak at around 1534 nm, which represents the transition from the lowest level in the $^4I_{13/2}$ manifold to the lowest level (E=0) in the $^4I_{15/2}$ manifold. The secondary peak at around 1550 nm corresponds to the transition from the lowest $^4I_{13/2}$ to the next higher (E>0) level in the ground state manifold.

By adding another gaussian peak centered left of the primary peak (i.e. contributing to the 'shorter wavelength tail' of the spectrum) at around 1525 nm, the next higher split level in the $^4I_{13/2}$ manifold was estimated. Now, the transition energy (i.e. wavelength) between the this second lowest $^4I_{13/2}$ and the second lowest $^4I_{15/2}$ level can be determined and added to the fit as another gaussian curve. Keeping in mind the exponential character of the split level populations in each
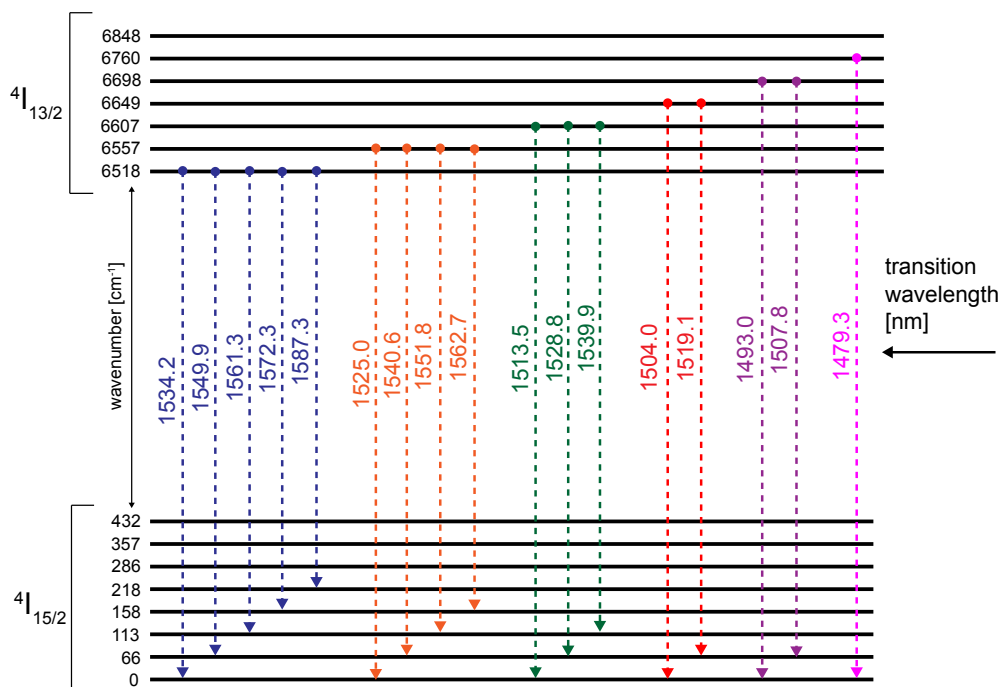
Fig. C.1: Radiative transitions between the $^4I_{13/2}$ and $^4I_{15/2}$ level manifolds of Er^{3+} ions at 77 K. The energy of each level is given in form of the wavenumber on the left hand side. The wavelength of each transition are indicated as downward arrows. Only the transitions shown are observable at T = 77 K; the color-coding corresponds to the the fitted curves in Fig. 1.8, where blue represents transitions from the lowest split level in the $^4I_{13/2}$ manifold, whereas transitions from the second lowest $^4I_{13/2}$ level are shown in orange, continuing with green, red, purple, and finally pink.

manifold given by the Boltzman distribution as stated in Eqn. 1.5, one can continue to add gaussian curves in the same way until the complete spectrum is satisfactorily matched by the sum of all transitions or gaussian peaks, respectively. Although this process is tedious and requires constant adjustment of height and width of already placed curves, a very good fit of the overall Er^{3+} emission spectrum was achieved as shown in Fig. 1.8.

Not all 56 possible transitions are contributing to the overall spectrum, due to the small populations in the higher-energy split levels at a temperature of 77 Kelvin. Only those transitions which can be resolved in the fit are illustrated as colored arrows in Fig. C.1.

The wavenumbers of the involved split levels in the $^4I_{13/2}$ and $^4I_{15/2}$ manifolds were determined from the observed transition energies (or wavelengths). At higher temperatures populations in the higher energy split levels of each manifold grow due to thermal excitation, increasing the probability of transitions from and to these levels. Therefore, a Er^{3+} emission spectrum recorded at room-temperature was fit
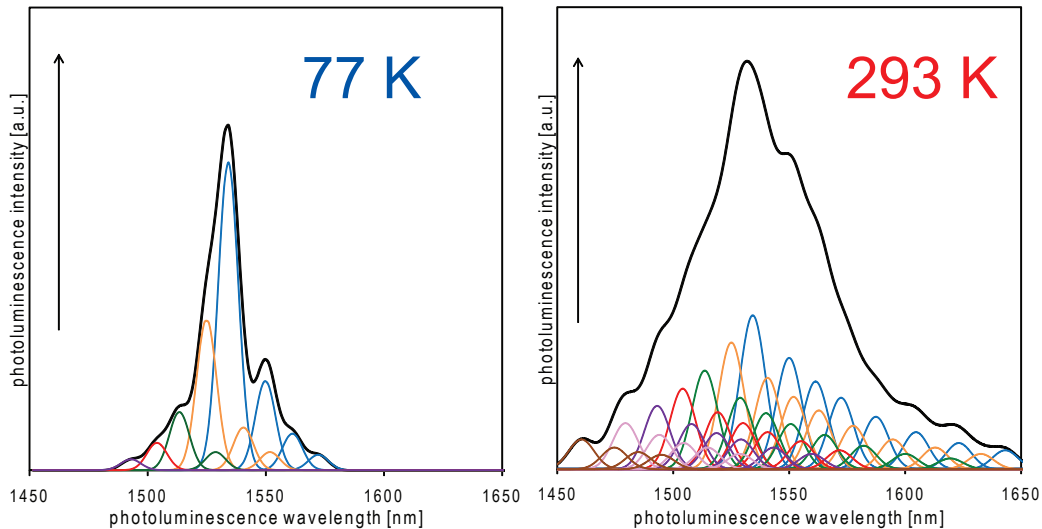
Fig. C.2: Emission spectra of Er^{3+} ions approximated using transitions between split levels found via fitting of experimental spectra and a Boltzman distribution in level populations. Contributing transitions (gaussian curves) and overall spectra (sum) are shown at 77 and 293 Kelvin.

to find these higher energy levels. The obtained energy values for all split levels are shown in Fig. C.1.

Figure C.2 illustrates the change in the overall emission spectrum with sample temperature as observed in experiment (see section 2.4.3). Here, spectra for temperatures of 77 Kelvin and 293 Kelvin are displayed. Transition wavelengths were calculated from the previously determined energies of the split levels and are represented by gaussian peaks. Also, the peak intensity of each transition was estimated using the population distributions given by Eqn. 1.5 for the respective temperature.

For example, the population in the lowest levels of the $^4I_{13/2}$ and $^4I_{15/2}$ manifolds were set to be 1, the transition between these levels ($\sim$1534 nm) was therefore weighted with a factor of $1 \times 1 = 1$. At 77 K, one then obtains (using Eqn. 1.5) populations of 0.29 and 0.485 for the second lowest levels of each manifold, the transition between these two levels ($\sim$1541 nm) was accordingly weighted with a factor of $0.29 \times 0.485 = 0.14$. The same transition is much stronger at 293 K ($0.72 \times 0.82 = 0.59$), due to increased thermal excitation. Both spectra in Fig. C.2 were obtained by summing all weighted transitions.

Not taken into account was the non-uniform broadening of the transitions (i.e. the width of the gaussian curves), resulting in the rather 'bumpy' character of the overall spectrum. It is evident, that the increased luminescence intensities on the left and right of the primary peak as well as the overall broadening, which were observed in experiment for increased temperatures, are caused by thermal excitation into higher energy split levels of the $^4I_{13/2}$ and $^4I_{15/2}$ manifolds.